AN ABSTRACT OF THE DISSERTATION OF

Daniel P. Mosher for the degree of Doctor of Philosophy in Mechanical Engineering presented on May 25, 2018.

Title: In-Situ Stereo Vision Metrology
for Metal Powder Bed Fusion Additive Manufacturing.

Abstract approved:

_____

Brian K. Bay

Powder Bed Fusion (PBF) techniques are additive manufacturing (AM) technologies with paradigm-shifting potential for the production industry. However, before they can become viable production solutions for quality critical industries, issues with process consistency and repeatability need to be addressed. There is a need for in-situ sensing systems that characterize process variation and analytical methods that relate sensor data back to input parameters and final part quality. This dissertation describes an in-situ stereovision-based metrology technique for characterizing 3D build surface variation in metal PBF AM. The natural optical characteristics of metal powders and fused metal regions are leveraged to extract high-precision 3D surface measurements from stereoscopic images of the powder bed. Measurement results are shown to detect spreader blade wear, broad powder surface height variations, powder spread interactions with part geometry, and powder bed surface irregularities linked to a focal part defect. Build surface measurements are also used to calculate layer-wise measures of powder layer thickness, material densification, and incremental build height which provide the information necessary to perform localized in-process parameter optimization with

closed-loop control. Finally, layer-wise stereoscopic surface measurement data are rendered volumetrically to produce quasi-tomographic representations of build process variation that may assist with final part qualification. This dissertation provides a foundation of knowledge for applying in-situ stereo vision metrology to metal PBF, but work remains to fully realize its potential.

In-Situ Stereo Vision Metrology for Metal Powder Bed Fusion Additive Manufacturing

by
Daniel P. Mosher

A DISSERTATION

submitted to

Oregon State University

in partial fulfillment of
the requirements for the
degree of

Doctor of Philosophy

Presented May 25, 2018
Commencement June 2018

Doctor of Philosophy dissertation of Daniel P. Mosher presented on May 25, 2018.

APPROVED:

Major Professor, representing Mechanical Engineering

Head of the School of Mechanical, Industrial, and Manufacturing Engineering

Dean of the Graduate School

I understand that my dissertation will become part of the permanent collection of Oregon State University libraries. My signature below authorizes release of my dissertation to any reader upon request.

Daniel P. Mosher, Author

ACKNOWLEDGEMENTS

I want to start by expressing sincere appreciation to my doctoral advisor, Brian Bay. The support and guidance you provided during the course of my graduate studies helped me grow as both a scholar and a person. You are a fantastic advisor, mentor, and friend. I look forward to working with you well into the future.

This work would not have been possible without the support of David Champion – thank you for all of your professional and personal mentorship throughout the years. I would also like to acknowledge and thank Andrew Queisser for his technical insights and perspective. It is my privilege to work with both of you.

Thank you to my family and friends – many of whom I consider one and the same – for providing unwavering encouragement throughout this process. Writing a dissertation is difficult, but I have an amazing support system to lean on and it made all the difference.

Last but not least, I want to acknowledge my wonderful wife, Kelsey Burkum. I am simply incapable of articulating how grateful I am for everything you do and how much it means to me. You are one of the strongest, most compassionate, and thoughtful people I know. You motivate me to want to improve myself every day, and that motivation has driven me to this accomplishment. I love you.

TABLE OF CONTENTS

TABLE OF CONTENTS (Continued)

LIST OF FIGURES

LIST OF FIGURES (Continued)

LIST OF FIGURES (Continued)

LIST OF FIGURES (Continued)

LIST OF TABLES

Chapter 1

General Introduction:
Motivation for Stereo Vision Metrology in Metal Additive Manufacturing

Daniel P. Mosher[1,2]

[1]Oregon State University, Corvallis, Oregon

[2]Department of Mechanical, Industrial, and Manufacturing Engineering

mosherd@oregonstate.edu

Introduction

Additive Manufacturing (AM) technologies construct 3D objects through the incremental addition of material. Early adopters utilized polymer-based systems as convenient rapid prototyping solutions because their layer-by-layer build process enabled streamlined fabrication of geometrically complex structures without the need for custom tooling. Advancements in technology have since delivered systems capable of producing functional metal components with shorter lead times and lower direct costs than traditional manufacturing methods [1]. Nevertheless, modern metal AM is not yet viable as an industry production solution. Although high quality potential has been demonstrated, improvements to the consistency and repeatability of additive systems are required before they can be reliably applied to manufacture parts for quality critical industries [2-4].

For all of the potential advantages of speed and flexibility offered by AM, there is one profound difficulty: a single large step in traditional manufacturing (e.g. casting or injection molding) effectively becomes thousands of small steps (each individual layer of a build). Since validation throughout production is a basic premise of quality assured manufacturing, this dramatic increase in the number of steps presents a significant challenge to quality assurance. Each step introduces additional unknowns that must be understood and accounted for to ensure part quality and reproducibility. Compounding the difficulty of layer-wise inspection is the variation and obscurity in how process inconsistencies manifest themselves within 3D printed components [1-3]. To address the quality assurance problem, and learn more about these relatively new technologies, industry researchers have turned to developing in-situ sensing systems that monitor the metal AM process [5].

Real-time monitoring and process control for reducing variability in metal AM has undergone initial investigation, but there is still much to be learned [1,3]. Most contemporary literature focuses on understanding a subset of AM technologies called Powder Bed Fusion (PBF) techniques, such as Selective Laser Melting (SLM), because they produce high-strength parts with higher feature resolution and tighter dimensional accuracy than wire or powder feed systems [4]. These techniques achieve their high performance by implementing a layer-by-layer process of sequentially spreading then fusing thin layers of metal powder. In metal powder bed methods there are three distinct opportunities being leveraged to gather information regarding the state of each manufacturing step: (1) after the recoat process but before laser scanning, (2) during laser scanning, and (3) after laser scanning but before the next recoat process.

Sensing and controlling powder bed uniformity in PBF is critical to process performance and overall part quality. The time after the recoat process but before laser scanning occurs has offered an excellent opportunity to either validate the recoat process or identify issues with the powder bed that require attention; monitoring the temperature of the fresh powder bed has also been performed. Craeghs et al. coupled a single camera with additional lighting sources to identify regions of sunken or elevated powder created by a damaged coater blade [6]. With this technique, changes in powder elevation are discernable because elevated powder will cast shadows on sunken powder. Concept Laser, a leading additive manufacturing systems vendor, uses a similar single-camera approach to monitor powder bed uniformity in their QMcoating Module [7]. Wegner et al. successfully integrated a single IR camera to measure temperature distributions on the post-spread powder surface [8]. While single camera techniques can be used to monitor

temperature field or identify streaking in the powder bed, they are unable to provide actual measurements of build surface variation in the out-of-plane direction [9]. Additionally, due to the nature of detecting anomalies using shadows, single camera methods have limited effectiveness for capturing subtle variations in surface height that can potentially impact final build quality. Implementation of a 3D surface profiling technique would enable direct measurement of these subtle variations in layer height, while providing additional understanding of significant anomalies and how to correct them.

Many researchers believe that temperature field is an excellent proxy for part quality because it has direct impact on the resulting microstructure, density, and mechanical properties of the part [1]. The best opportunity to understand the temperature field is during the process of laser scanning. A large portion of literature to date focuses on monitoring during laser scanning with a motivation to understand the characteristics of the melt pool and surrounding heat affected zone. Bi et al. initially showed that integration of a suitable photodiode into a processing head can provide a coaxial measurement of average melt pool temperature [10-11]. Later, Lott et al. [12] designed a single-camera imaging system to monitor the size and shape of the melt pool, and prove its capabilities at high scanning velocities. Craeghs et al. [13-14] then used a similar single-optical-camera system in combination with a photodiode to demonstrate that melt pool size is roughly proportional to photodiode signal. Concept Laser's patented QMmeltpool Module also uses a CMOS camera in combination with a photodiode to control the temperature and size of the melt pool by adjusting laser power [7-8]. Doubenskaia et al. utilized a pyrometer to monitor the heat affected zone during SLM as a function of hatch spacing [15]. They showed that for thin powder layers (50 μm), pyrometer signal generally

increases with increasing hatch spacing since the thermal conductivity of the powder bed is approximately 20-times lower than bulk material. For thick powder layers (1 mm), when there is no metallurgical contact with the substrate, the opposite trend was observed [15]. Krauss et al. took a slightly different approach by mounting an IR camera to the outside of an SLM system to monitor the heat affected zone from a fixed reference frame [16]. This method enabled them to monitor a 50 mm objective at 50 Hz with a spatial resolution of 250 µm/pixel. However, the downside of in-situ sensing and control systems that leverage this opportunity is they require significant data acquisition and processing rates due to the dynamic nature of the laser scanning process. These requirements contribute to the overwhelming data volumes that monitoring the AM process is notorious for producing, thus providing another barrier to adoption [17]. If an alternative method for intelligently controlling laser power can be established, such as creating a laser power map based on a predictive model of how the melt pool behaves as a function of cross-sectional geometry and local layer thickness, then it may be possible to avoid data-intensive melt pool monitoring and control altogether.

In addition to thermal signatures, geometric fidelity is a key component of final part quality. By monitoring each section after scanning, its fidelity can be validated, or unacceptable geometric variation can be identified to provide tremendous benefit. Abandoning a faulty build early in the process can save a significant amount of time and money. Additionally, understanding how the build is progressing enables the potential for part-saving corrective action. The time after laser scanning but before the next recoat process has provided an opportunity to evaluate the fidelity of each scanned section and reassess the state of the powder bed before recoating occurs. Cooke et al. mounted a

single-camera vision system to the outside of the build chamber to monitor the planar geometry of scanned sections [18]. They used edge detection algorithms to identify the profile of each scanned section after the images were corrected for perspective distortions. Kleszczynski et al. integrated a 29 MP CCD camera into a Laser Beam Melting system and attempted to identify errors by imaging printed sections after scanning and again after recoating [19]. Their results showed that high resolution images (~24 µm/pixel) are attainable for reasonable sized working areas (100 mm x 100 mm). However, the information gathered from their setup is essentially the same as what Craeghs et al. accomplished earlier [6]: relative identification of variations in layer height, but no way to measure these variations quantitatively. As previously established, single camera techniques are unable to measure out-of-plane variation. Although evaluating planar geometric fidelity is useful, it does not provide complete understanding of the situation. Fidelity in the out-of-plane direction (adherence to layer height) is a parameter that must be evaluated to fully validate scanned sections. Additionally, it is necessary to measure surface height after scanning to calculate a “true” powder layer thickness after recoating occurs. Measurement of surface height before and after laser scanning can be achieved by implementing a 3D surface profiling technique.

Based on the gaps in state of the art sensing and control systems described above, a technique that monitors and characterizes out-of-plane (z-height) variation would greatly benefit metal PBF technologies. Many researchers are fixated on monitoring the melt pool as the primary means for controlling build quality. However, this method produces unwieldy data volumes and requires high data processing rates to be effective. It is possible that the need for data-intensive monitoring of the melt pool during laser scanning

can be mitigated by gaining more information from the quasi-static monitoring opportunities before and after laser scanning occurs [17].

Dissertation Content

The manuscripts in this dissertation relate to the development of a stereovision-based metrology technique for monitoring, characterizing, and presenting 3D build surface variation in metal PBF. Chapter 2 details the implementation of an in-situ stereoscopic measurement system to monitor 3D build surface variation in a production SLM machine. Chapter 3 extends in-situ build surface measurements to calculate layer-wise measures of powder layer thickness, material densification, and incremental build height which provide the information necessary to perform localized in-process parameter optimization with closed-loop control. Chapter 4 casts layer-wise stereoscopic surface measurement data into a rich volumetric form to produce a quasi-tomographic representation of build process variation in the context of as-built part geometry. Chapter 5 identifies potential directions for future work based on the individual manuscript findings.

References

1. Tapia G, Elwany A (2014) A Review on Process Monitoring and Control in Metal-Based Additive Manufacturing. J. Manuf. Sci. Eng 136(6), 060801

2. King WE, Anderson AT, Ferencz RM, Hodge NE, Kamath C, Rubenchik AM (2015) Laser Power Bed Fusion Additive Manufacturing of Metals; Physics, Computational, and Materials Challenges. Applied Physics Review 2(4)

3. Spears TG and Gold SA (2016) In-process sensing in selective laser melting (SLM) additive manufacturing. Integrating Materials and Manufacturing Innovation (2016) 5(2)

4. Fraizer WE (2014) Metal Additive Manufacturing: A Review. Journal of Materials Engineering and Performance 23(6):1917-28

5. Everton SK, Hirsch M, Stravroulakis P, Leach RK, Clare AT (2016) Review of in-situ process monitoring and in-situ metrology for metal additive manufacturing. J. Materials & Design 95(2016)

6. Craeghs T, Clijsters S, Yasa E, Kruth JP (2011) Online Quality Control of Selective Laser melting. Proceedings of the 22nd Annual International Solid Freeform Fabrication Symposium

7. Dunsky C (2014) Process Monitoring in Laser Additive Manufacturing. Industrial Laser Solutions

8. Wegner A, Witt G (2011) Process Monitoring in Laser Sintering using Thermal Imaging. Solid Freeform Fabrication: Proceedings, August 2011: University of Texas at Austin 2011

9. Townsend A, Senin N, Blunt L, Leach RK, Taylor JS (2016) Surface Texture Metrology for Additive Manufacturing: A Review. Prec. Eng. 46(2016):34-47

10. Bi G, Gasser A, Wissenbach K, Drenker A, Poprawe R (2006) Characterization of the Process Control for the Direct Laser Metallic Powder Deposition. Surface and Coatings Technology 201(6):2676-2683

11. Bi G, Shürmann B, Gasser A, Wissenbach K, Poprawe R (2007) Development and Qualification of a Novel Laser-Cladding Head with Integrated Sensors. International Journal of machine Tools and manufacturing 47(3):555-561

12. Lott P, Schleifenbaum H, Meiners W, Wissenbach K, Hinke C, Bultmann J (2011) Design of an Optical system for the In Situ Process Monitoring of Selective Laser Melting (SLM). Physics Procedia 12(2011):683-690

13. Craeghs T, Bechmann F, Berumen S, Kruth JP (2010) Feedback control of Layerwise Laser Melting using Optical Sensors. Physics Procedia 5(2010):505-514

14. Craeghs T, Clijsters S, Yasa E, Bechmann F, Berumen S, Kruth JP (2011) Determination of geometrical factors in Layerwise Laser Melting using optical process monitoring. Optics and Lasers in Engineering 49(2011):1440-1446

15. Doubenskaia M, Pavlov M, Grigoriev S, Tikhonova E, Smurov I (2012) Comprehensive Optical Monitoring of Selective Laser Melting. Journal of Laser Micro/Nanoengineering 7(3):236-243

16. Krauss H, Eschey C, Zaeh MF (2012) Thermography for Monitoring the Selective Laser Melting Process. Proceedings of the Solid Freeform Fabrication Symposium

17. Seifi M, Salem A, Beuth J, Harrysson O, Lewandowski JJ (2016) Overview of Materials Qualification Needs for Metal Additive Manufacturing. JOM 68(3):747:764

18. Cooke AL, Moylan SP (2011) Process Intermittent Measurement for Powder-Based Additive Manufacturing. Proceedings of the 22nd International SFF Symposium – An Additive Manufacturing Conference

19. Kleszczynski S, Jacobsmühlen J zur, Sehrt JT, Witt G (2012) Error Detection in Laser Beam Melting Systems by High Resolution Imaging. Proceedings of the 23rd Annual International Solid Freeform Fabrication Symposium

Chapter 2

In-Situ Stereoscopic 3D Surface Measurement System for Metal Powder Bed Fusion Additive Manufacturing

Daniel P. Mosher[1,2], Brian K. Bay[1,2]

[1]Oregon State University, Corvallis, Oregon

[2]Department of Mechanical, Industrial, and Manufacturing Engineering

mosherd@oregonstate.edu

Abstract

Metal Powder Bed Fusion (PBF) techniques are Additive Manufacturing (AM) technologies with paradigm-shifting potential for the production industry. However, production PBF systems continue to treat each build layer as though it is flat and consistent, which perpetuates the gap in understanding between process inputs and outputs while contributing to repeatability issues. This work details the development and application of an in-situ stereoscopic 3D surface measurement system for metal PBF AM. We first describe the optical characteristics of metal powders and lighting conditions used to extract 3D surface measurements from stereoscopic images of the powder bed. We then propose and experimentally verify a closed-form approximation for stereoscopic depth measurement error as a function of vision system geometry and calibration reprojection error. Finally, the monitoring system is installed on a commercial SLM system and used to monitor 3D surface variation during the fabrication of a metal turbine. Measurement results show numerous effects during the build: spreader bar wiper blade wear, broad powder surface height variations, interaction of powder surface spread with part geometry, and powder irregularities linked to a focal build defect.

Introduction

Metal Powder Bed Fusion (PBF) techniques, such as Selective Laser Melting (SLM), are Additive Manufacturing (AM) technologies with paradigm-shifting potential for the production industry. By coupling a layer-by-layer build process with the ability to read profile information directly from a 3D CAD file, these methods are capable of fabricating geometrically complex, functional metal components without the need for custom tooling.

The approach offers an unprecedented freedom of design with shorter lead times and lower direct costs than traditional manufacturing methods [1]. Yet these technologies are struggling to gain traction as viable production solutions for quality-critical industries, such as the medical and aerospace sectors, because significant uncertainty remains regarding process repeatability and quality of the final product [1-3].

For all of the advantages offered by layer-wise manufacturing, there is one profound difficulty: a single large step in traditional manufacturing (e.g. casting or injection molding) effectively becomes thousands of small steps (each individual layer). This dramatic increase in the number of steps creates significant challenges with regard to quality assurance because each new step provides an opportunity for the build process to go awry. Since validation throughout production is a basic premise of quality assured manufacturing, complete validation of 3D printed parts will ultimately require thousands of individual inspections. Compounding the difficulty of layer-wise inspection is the variation and obscurity in how process inconsistencies manifest themselves within 3D printed components [1-3].

To address the quality assurance problem and learn more about these relatively new technologies, industry researchers have turned to developing in-situ sensing systems that monitor the build process. Countless systems have been implemented with objectives ranging from monitoring characteristics of the melt pool with various sensors [4-11] to assessing the uniformity [12] and temperature [13] of the powder bed with a single camera setup. The planar fidelity of scanned sections has also been evaluated using a single optical camera with additional lighting sources [14-17]. The limitation of single-camera 2D imaging techniques is that they are incapable of providing quantitative out-of-plane (z-

height) information, rendering them inadequate for characterizing build surface variation [16,18]. A recent publication described the application of 3D Digital Image Correlation (3D-DIC) to perform in-situ defect detection in a part printed via Fused Deposition Modeling (FDM) [19]. Although similar in principal to our method, the FDM study required introduction of a contrast agent (visible particles added to the base polymer material) in order to support the stereovision process.

We sought to achieve a monitoring system suitable for powder systems that did not interfere in any way with the basic process, required no modification of the material system, and generated quantitative information of high precision relative to desired levels of process control. We also sought information for the entire build region, covering both unfused powder and fused material, in a form relevant to powder spreading and fusion operations. This was motivated by an interest in treating the process zone in a more realistic and detailed manner. Production powder systems continue to treat the thickness of the process zone (i.e. powder layer thickness and fused layer thickness) as a nominal parameter, despite the known impact of variations in these parameters on final part quality [3]. The assumption that each build layer is flat and consistent perpetuates the gap in understanding between process inputs and outputs while contributing to poor repeatability being associated with powder fusion technologies [3]. Our process satisfies these requirements by leveraging the natural optical characteristics of metal powders and fused metal regions within a stereovision-based digital image correlation environment.

This manuscript details the application of a stereo vision system to make accuracy-verified measurements of the in-situ 3D build surface variation in metal powder additive manufacturing. We describe how the optical characteristics of metal powder are

leveraged to extract high-precision 3D surface measurements from stereoscopic images of the powder bed. We then propose and experimentally verify a closed-form approximation for stereoscopic depth measurement (z-height) error as a function of vision system geometry and calibration reprojection error. Finally, the prototype system is implemented to monitor layer-wise 3D surface variation during the fabrication of a metal turbine in a ProX 320 production SLM machine.

Materials & Methods

Optical Configuration

The stereo vision system used for this study employed two Grasshopper3 12MP USB 3.0 cameras with 4240 x 2824 pixel resolution (3.1 μm pixel size) on a 1” format monochromatic CCD sensor (Point Grey). The cameras imaged the build platform of a ProX 320 (3D Systems) production SLM machine through custom viewing windows designed to interface with pre-existing access ports (Figure 2.1). In this configuration, with the cameras located outside of the vacuum chamber to avoid extreme environmental conditions, the optical working distance was constrained to approximately 600 mm. The precise baseline distance between cameras and their relative orientation were determined from the extrinsic parameters of the stereo camera calibration process, which is described subsequently. Cameras were angled roughly 27º from vertical.

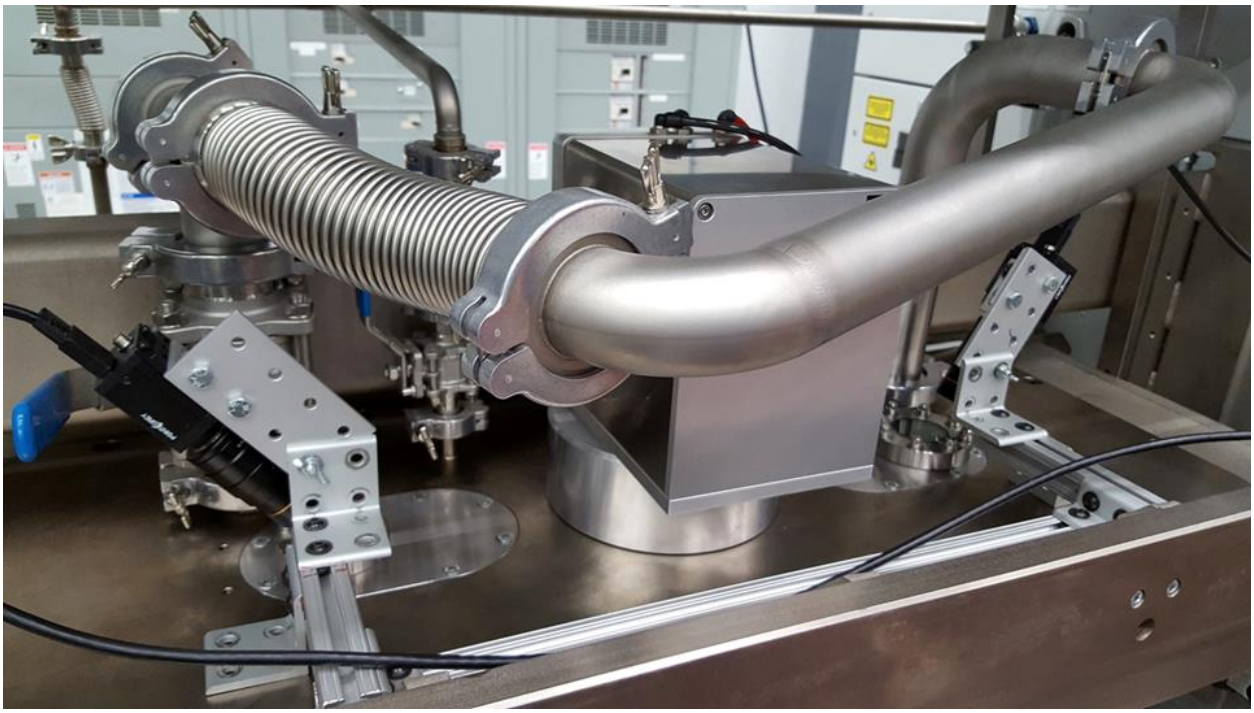

Figure 2.1: Stereo vision system and custom viewing windows integrated into ProX 320 SLM machine. Cameras image through optical ports on the top of the vacuum chamber, adjacent to the laser system.

Two different lens combinations were utilized during the study to adjust spatial resolution by controlling field of view. First, the maximum focusable lens equivalent, 100 mm lens with a 15 mm extension tube was configured to perform experimental verification of stereoscopic z-height measurement accuracy at the spatial resolution limit of the optical configuration (63 mm x 42 mm field of view, 15 µm/pixel). Then 35 mm lenses were equipped to accommodate the entire build platform during in-situ inspection of a turbine build (203 mm x 135 mm field of view, 48 µm/pixel).

Lighting and Polarization

Lighting is a critical component of vision systems used as measurement devices, especially when the objective surface contrast is sub-optimal (e.g. metal powder). To improve the surface contrast in metal powder images, and enable the use of a minimum

lens f-stop for maximum depth of field, two LED light panels (Polaroid 350) were mounted inside the ProX 320 build chamber (Figure 2.2). The light panels provided sufficient illumination, but also produced reflections that interfered with stereo correlation. Reliable image correlation was restored after cross-polarization was implemented between the light sources and lenses to suppress these reflections.

Figure 2.2: Polarized LED light panels were employed in tandem with adjustable lens polarization filters to improve the contrast of metal powder surfaces and suppress reflections that inhibited the stereo correlation process.

Metal Powder Texture as a Tracking Mechanism for Optical Surface Measurement

The basis for high-precision optical surface measurement techniques, such as 3D Digital Image Correlation (DIC) [20], is a locally unique surface pattern that supports the use of template matching algorithms to locate common features within stereo image pairs. In standard DIC applications, a white light speckle pattern is applied to the surface of objects to attain sufficient distinguishability for reliable tracking from image-to-image (Figure 2.3). In this particular application, the optical similarity of metal powder to white light speckle provides a natural tracking mechanism that can be leveraged for the stereo correlation process. This project utilized Inconel 718 powder with a 45 +/- 15 micron

particle size distribution. The metal powder particles are under-resolved in comparison with ideal speckle for DIC [20], but useable images were generated in both large and small field of view configurations.

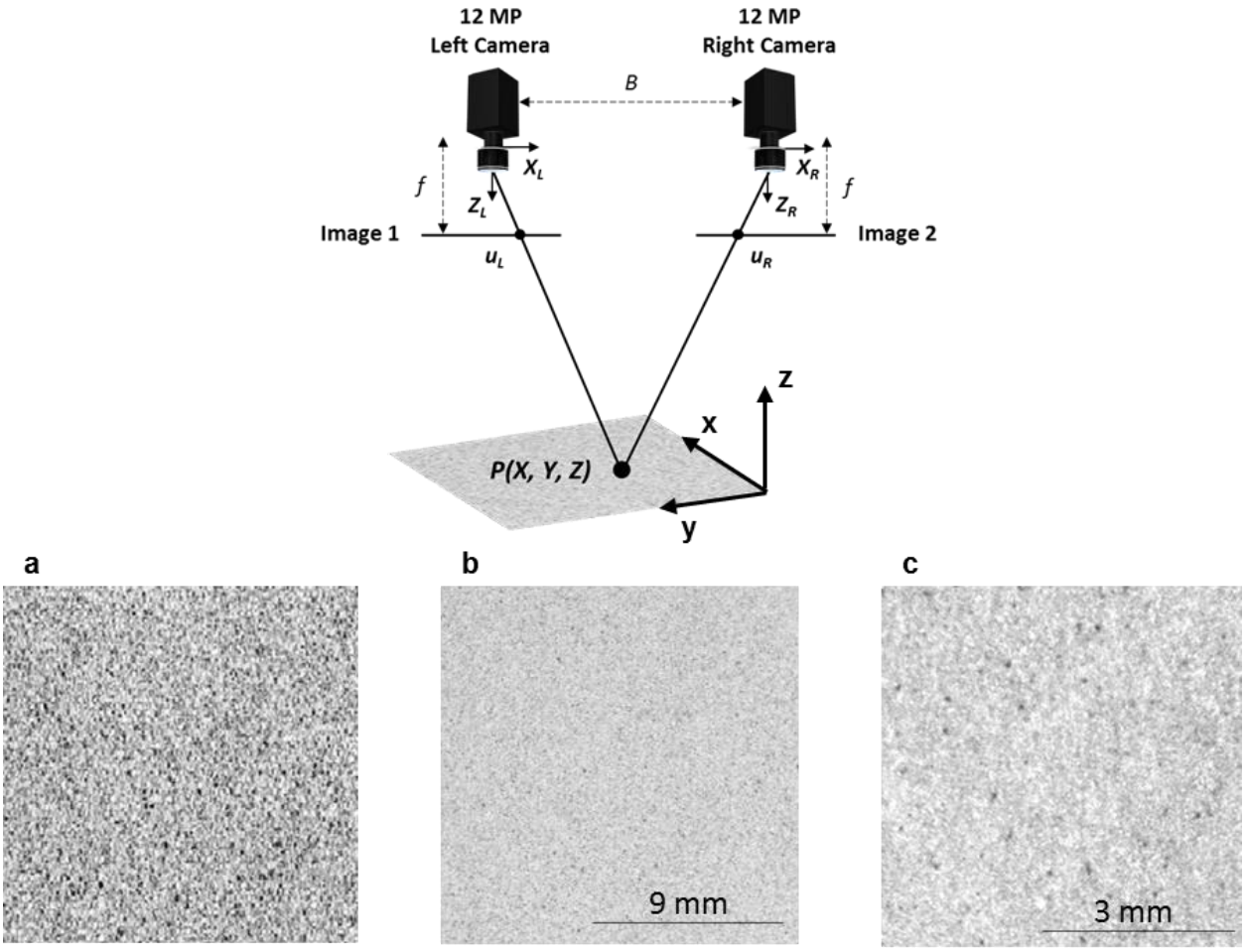

Figure 2.3: (top) Stereovision requires co-locating equivalent points, $P(X,Y,Z)$, in two cameras viewing a scene from different angles. In classic Digital Image Correlation, an applied speckle pattern (a) provides the local features supporting this co-location. Although not ideal, metal powder at both low and high magnification produced suitable images. (b) 203 mm x 135 mm field of view, 48 µm/pixel (c) 63 mm x 42 mm field of view, 15 µm/pixel.

Image Acquisition and Processing

The vision system was controlled by custom LabVIEW (National Instruments) software that supported both manual and automated image capture (Figure 2.4). Manual capture

was used to characterize, tune, and calibrate the vision system parameters pre-build. The automated capture functionality was utilized during the build to acquire layer-wise stereoscopic images of the powder bed. The SLM system sweeps powder back-and-forth from reservoirs, filling space left after controlled drop of the build platform. Automated capture was achieved by monitoring the position of the spreader bar via externally located LEDs that indicated spreader bar motion. A photodiode was used to generate a voltage whenever the spreader bar began to move. The voltage information was converted to a Boolean “on/off” signal that triggered image capture before and after each new powder layer was deposited.

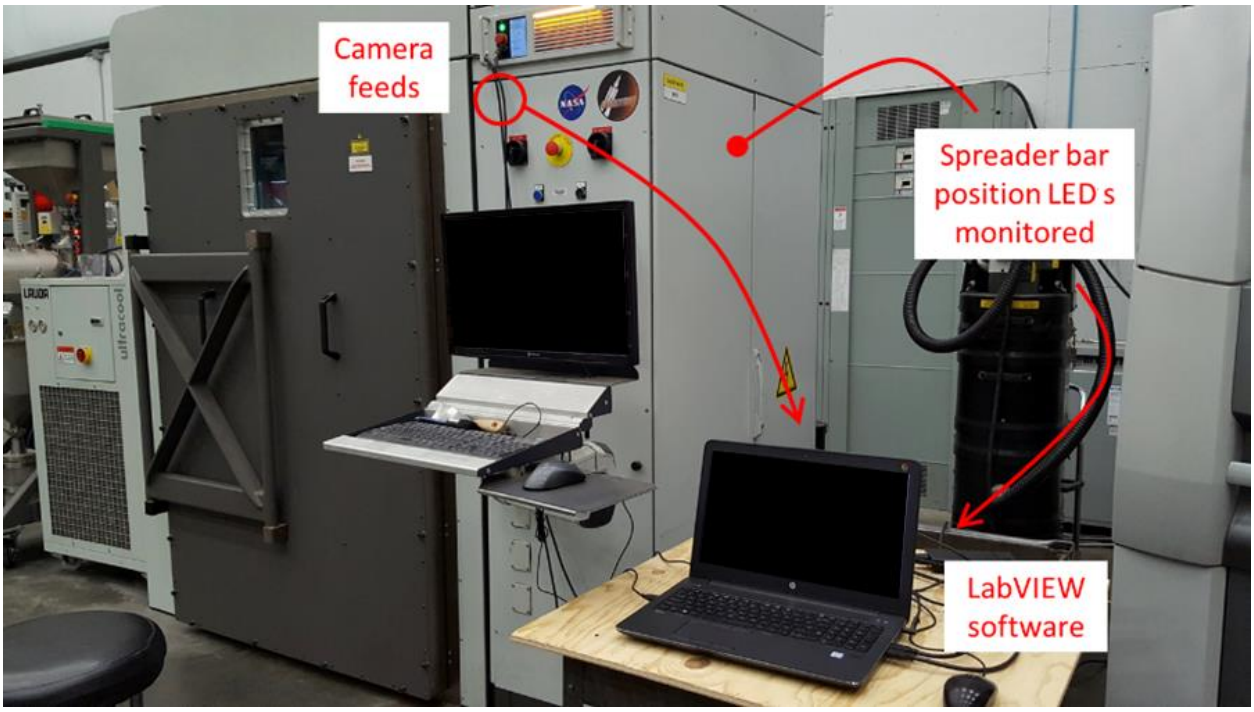

Figure 2.4: Experimental setup utilized to support automated imaging during the build process. Custom LabView software was developed to monitor externally located LEDs that indicate spreader bar motion. Automation was achieved by triggereing image capture before and after each new powder layer was deposited.

3D surface measurements were extracted from stereo images using the commercial DIC software Vic-3D (Correlated Solutions). Vic-3D measures pointwise disparities

between features in stereo image pairs using subset tracking algorithms then uses the disparity information to reconstruct 3D surfaces based on a model of the two-camera system geometry. Therefore, stereo calibration was required to reconstruct 3D surfaces using the Vic-3D software.

Stereo Camera Calibration and Depth Extraction

Stereo camera calibration is used to estimate the optical parameters of a two-camera vision system required to extract quantifiable and accurate depth information from stereo image pairs. The parameters include camera intrinsics, camera extrinsics, and distortion coefficients. Intrinsic parameters are the camera-specific operating characteristics (i.e. the equivalent lens focal length measured in pixels, the coordinates of the true optical center, the pixel skew coefficient, and the distortion parameters). Extrinsic parameters detail the relative position and orientation of both cameras in 3D world coordinates (i.e. the rigid body translation and rotation vectors). Together the intrinsic and extrinsic parameters are used to determine the relationship between measured pixel disparity values and quantifiable z-height. For the simplest case of a calibrated stereo system with parallel optical axes, the geometry looks like Figure 2.5. However, in reality the system can be arbitrarily general.

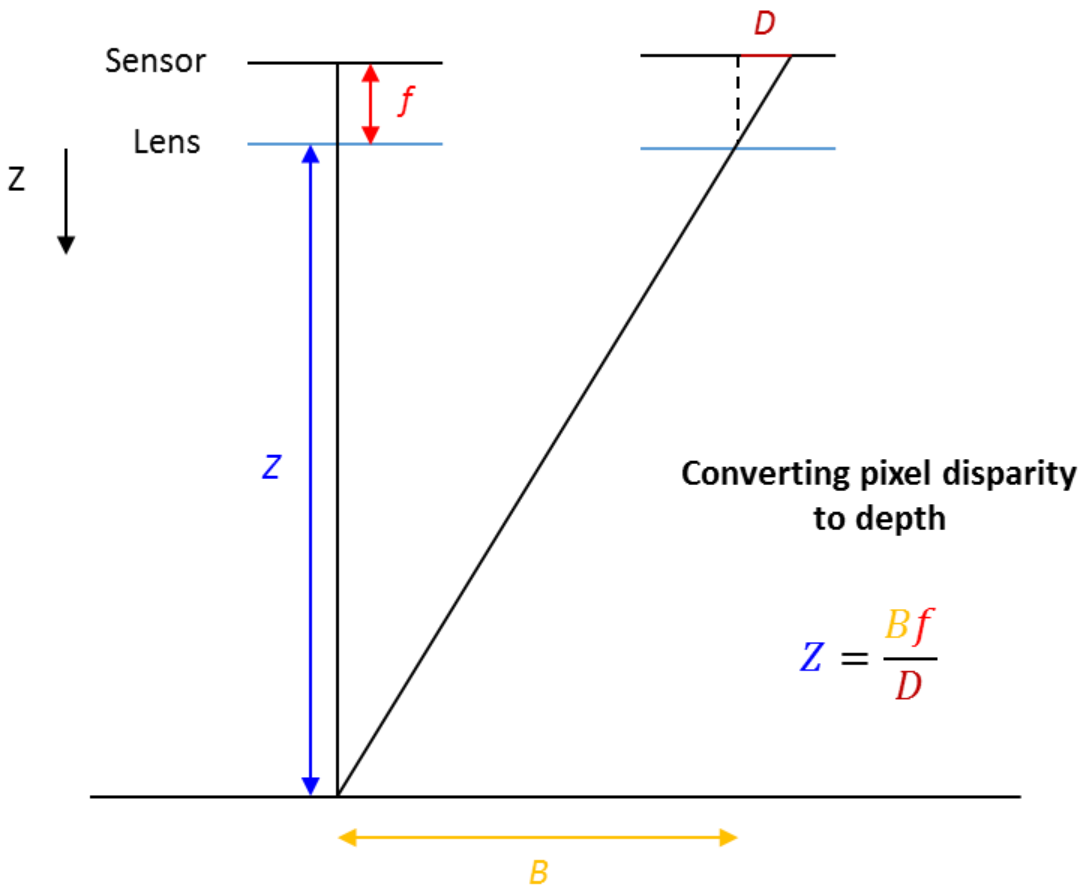

Figure 2.5: Idealized stereo vision geometry used to relate depth to disparity for a rectified system; where Z is the perpendicular distance from the camera system to the target (meters), f is the lens focal length (pixels), B is the baseline distance between cameras (meters), and D is the disparity between common features in stereo images (pixels). The lens focal length and baseline distance parameters are determined from the stereo calibration process.

Stereo camera parameters are estimated algorithmically by analyzing a sequence of calibration images. The images depict a planar calibration target containing a known regular grid pattern positioned at different orientations and tilts within the shared field of view of the two-camera system. The analysis is based on the pinhole camera model that has been modified to account for Seidel lens distortions [20]. The model sets up a parametric fitting process to solve the correspondence problem between 3D world coordinates and their analogous 2D image points. Moving the target around the field of

view, specifically introducing extreme amounts of out-of-plane tilt, improves the parametric fitting process by providing additional correspondence information between 3D world coordinates and 2D image points [20]. The outputs of the pinhole correspondence problem are the intrinsic and extrinsic system parameters. The Seidel modification leverages the constraint that the planar grid pattern should appear uniform in corrected calibration images to calculate the coefficients required to remove lens distortions from subsequent images taken with the camera system. For this study, calibration was performed with two different standard Vic-3D calibration targets: 17 x 14 dots with 2 mm spacing (high-magnification) and 17 x 14 dots with 6 mm spacing (low-magnification). During each calibration, the targets were positioned at 40 different locations, orientations, and tilts within the shared camera field of view.

Due to the nature of the parametric fitting process, calibration results will inherently contain errors that impact the depth measurement accuracy of stereo systems. Extremely thorough approaches for evaluating the sources of measurement error in generic stereo-based systems have been demonstrated [21-22]. These methods would ultimately provide the most comprehensive characterization of system performance, and they should be applied when detailed system understanding is required. However, they are time-consuming and frankly excessive for the level of characterization we desire.

We seek a simplified closed-form alternative that enables us to conservatively approximate the overall stereoscopic measurement uncertainty of a potential system based on hardware, configuration, and calibration error. If we wish to come up with a reasonable approximation for stereoscopic measurement uncertainty, then we need a numerical description of the error associated with the calibration results. Calibration

reprojection error describes the average pointwise deviation from the ideal pinhole camera model in pixels and it can be used to estimate point correspondence errors between stereo images [23]. Calibration of the high-magnification setup yielded a reprojection error of 0.073 pixels. The calibration process for the low-magnification configuration had a reprojection error of 0.064 pixels.

Stereoscopic Z-Height Measurement Uncertainty

The goal of this section is to provide a convenient closed-form approximation for stereoscopic depth measurement uncertainty as a function of vision system hardware, configuration, and calibration reprojection error. We start from the simple parallel optical axes system geometry, then reintroduce uncertainties associated with realistic implementation to arrive at a convenient equation for estimating stereo depth extraction performance. To be clear, the methods described in [21-22] will still provide the most comprehensive understanding of stereo system performance, and should be applied when detailed characterization of error sources is required for specific system instantiations. However, as shown through subsequent experimental validation, the closed-form approximation presented herein can be useful for broadly estimating stereoscopic depth measurement performance and applying confidence intervals to z-height measurements made with generically configured stereo systems.

From the geometry shown in Figure 2.5, it is straightforward to determine the relationship between a measured stereo pixel disparity D and the corresponding distance Z for an idealized stereo vision system, without misalignment, relative rotations, or lens distortions, such that resulting stereo image pairs are rectified [23]:

$$Z = \frac{Bf}{D}$$

where B is the baseline distance between cameras and f is the lens focal length. While this rectified geometry does not directly reflect the angled system implemented in this study, it also does not misinform the relationship between depth and disparity for the purposes evaluating uncertainty associated with stereo depth extraction. Image rectification is an established method in computer vision for simplifying the stereo depth extraction process in which stereo image pairs are projected onto a common image plane [20, 23]. In the present case, we are effectively performing a virtual system rectification as an alternative to subsequently rectifying stereo image pairs during post-processing. Therefore, errors associated with calibration and image interpolation will need to be included in our estimate for disparity measurement uncertainty to accurately reflect the equivalent post-processing rectification procedure [20].

From the above result, the difference in any two z-height measurements taken with the same stereo vision system can be written as follows:

$$\Delta Z = Z_2 - Z_1 = \frac{Bf}{D_2} - \frac{Bf}{D_1} = Bf\left(\frac{\Delta D}{D_1 D_2}\right)$$

We can obtain the theoretical z-height measurement resolution by minimizing this result:

$$min(\Delta Z) = Bf\left(\frac{min(\Delta D)}{D^2}\right)$$

where $\min(\Delta Z)$ is the theoretical resolution of stereoscopic z-height measurements, $\min(\Delta D)$ is the level of sub-pixel interpolation error associated with measuring pixel disparity between common features in stereo image pairs, and $D_1 D_2$ becomes D^2 because the two disparity values are virtually identical. This result considers the limitations of measuring pixel disparity from discrete digital data for a generalized stereo

vision system when subset size and stereo angle are properly considered in the estimation of $min(\Delta D)$. However, to realistically model the error associated with stereoscopic depth measurements, the error associated with the calibration process must also be incorporated in the estimate for disparity measurement uncertainty [20].

We can thus add the potential random variation described by the calibration reprojection error to the level of sub-pixel interpolation error to yield the following closed-form approximation for stereoscopic z-height measurement error:

$$Z_{error} = Bf\left(\frac{min(\Delta D) + \varepsilon}{D^2}\right)$$

where ε is the calibration reprojection error term. An alternative form of the above equation, more suitable for experimentation, can be written as follows:

$$Z_{error} = Z^2\left(\frac{min(\Delta D) + \varepsilon}{Bf}\right)$$

where Z is the distance from the stereo vision system to the measurement plane (optical working distance), which was measured as 600 mm during experimentation. A conservative estimate of 1/16th of a pixel for $min(\Delta D)$ is obtained by evaluating factors that contribute to sub-pixel interpolation error [20], including subset size, stereo angle, and the sub-optimal nature of the texture in images of metal powder surfaces being leveraged to perform template matching. The other variables were determined during stereo camera calibration, and the error associated with the virtual rectification process is contained in the reprojection error term. The average focal length of both cameras was used to calculate the stereoscopic z-height error in this study.

Table 2.1 outlines the projected z-height measurement error for both instantiations of the prototype vision system used in this study. According to the results, the system was

projected to measure z-height variation within ±1.4 µm at high magnification and within ±6.0 µm at low magnification. For standard fixed focal length lenses, the focal length in pixels can be approximated by dividing the lens focal length by the sensor pixel size. However, for the high-magnification configuration, the use of 100 mm lenses in combination with 15 mm extension tubes altered the magnification properties such that the actual equivalent focal length was 158 mm according to calibration results. Consideration of this nonlinearity should be made when applying the approximation to a system with extension tubes in the future.

Table 2.1: Projected z-height measurement error for both instantiations of the prototype vision system and the relevant stereo camera parameters used to perform the approximation.

$Lenses$	Z_{error}	Z	$min(\Delta D)$	ε	B	f
115 mm	**±1.4 µm**	600 mm	0.063 pixel	0.073 pixel	687 mm	51521 pixels
35 mm	**±6.0 µm**	600 mm	0.063 pixel	0.064 pixel	676 mm	11328 pixels

Figure 2.6 illustrates the sensitivity of these approximations to imprecise measurement of the optical working distance. It would take an error of over 50 mm to alter the projected measurement accuracy of the 35 mm instantiation by ±1 µm; the same error would only alter the projected measurement accuracy of the 115 mm instantiation by ±0.3 µm. The result also demonstrates that the z-height measurement accuracy of this

technique is not significantly affected by out-of-plane variations in the powder bed, which typically do not exceed a few hundred microns.

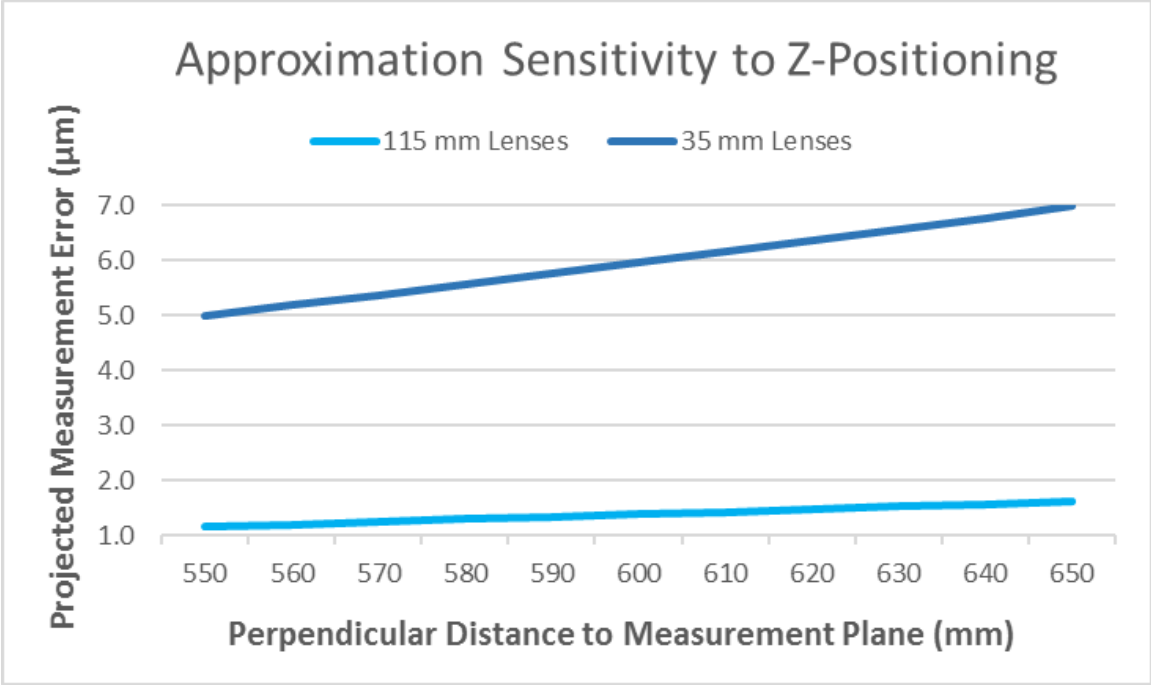

Figure 2.6: Sensitivity of the closed-form approximation to mismeasurements of working distance for both instantiations of the stereo vision system used in this study.

Results

Experimental Verification of Stereoscopic Z-Height Measurement Accuracy

Among the goals of this study was to (1) verify the z-height measurement accuracy of the prototype stereo vision system and (2) provide experimental validation for the closed-form approximation for z-height measurement accuracy derived in the previous section. A straightforward method for verifying the accuracy of a measurement system is to compare experimental measurement results against established known values. If the experimental results can also be corroborated with predicted performance, then we can justify validation of the closed-form approximation. In the case of the ProX 320,

adjustment of the build platform is highly controlled and known within a typical accuracy of ±0.2% the adjusted distance. Therefore, the build platform was utilized to create known changes in z-height that could be compared to the experimental values measured by the stereo vision system (Figure 2.7).

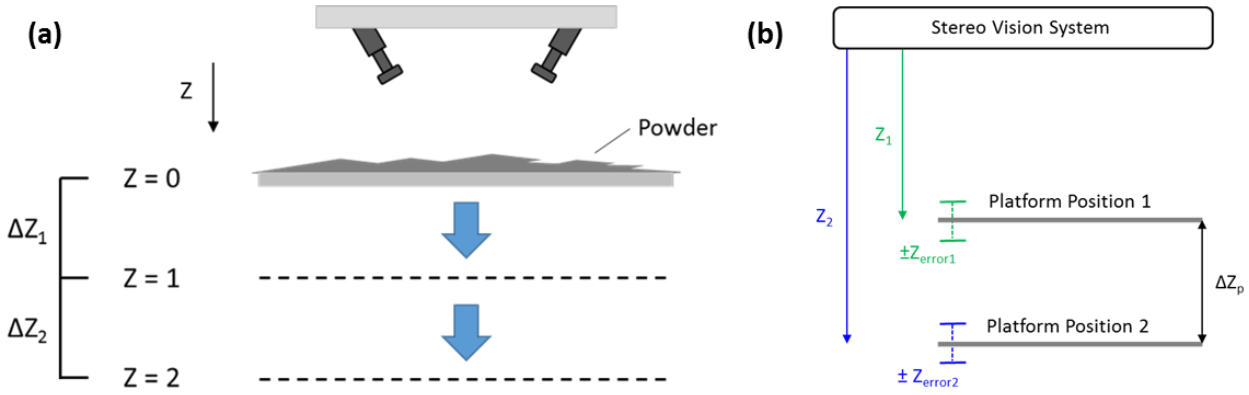

Figure 2.7: (a) Strategy for experimental verification of stereoscopic z-height measurement accuracy (b) Diagram of the error associated with measuring changes in z-height created by adjusting the build platform position in the ProX 320.

Three repeat stereo image pairs were initially acquired with the platform at a nominal position (Z = 0). Subsequent triads of stereo images were then acquired after the platform was dropped 30 µm below the nominal position (Z = 1) and again at 60 µm below the nominal position (Z = 2). After calibration (ε = 0.073 pixel), Vic-3D was used to measure the platform drops at nearly 9,000 locations within the field of view using 55-pixel subsets. Data for each platform position was obtained by correlating stereoscopic images taken at the dropped position with stereoscopic images from the nominal platform position. Multiple experimental trials were performed with no significant change in measurement results. Figure 2.8 shows representative results from a single trial plotted alongside the upper and lower theoretical bounds predicted by the closed-form approximation for

stereoscopic z-height measurement error. The code for generating this plot can be found in Appendix A.

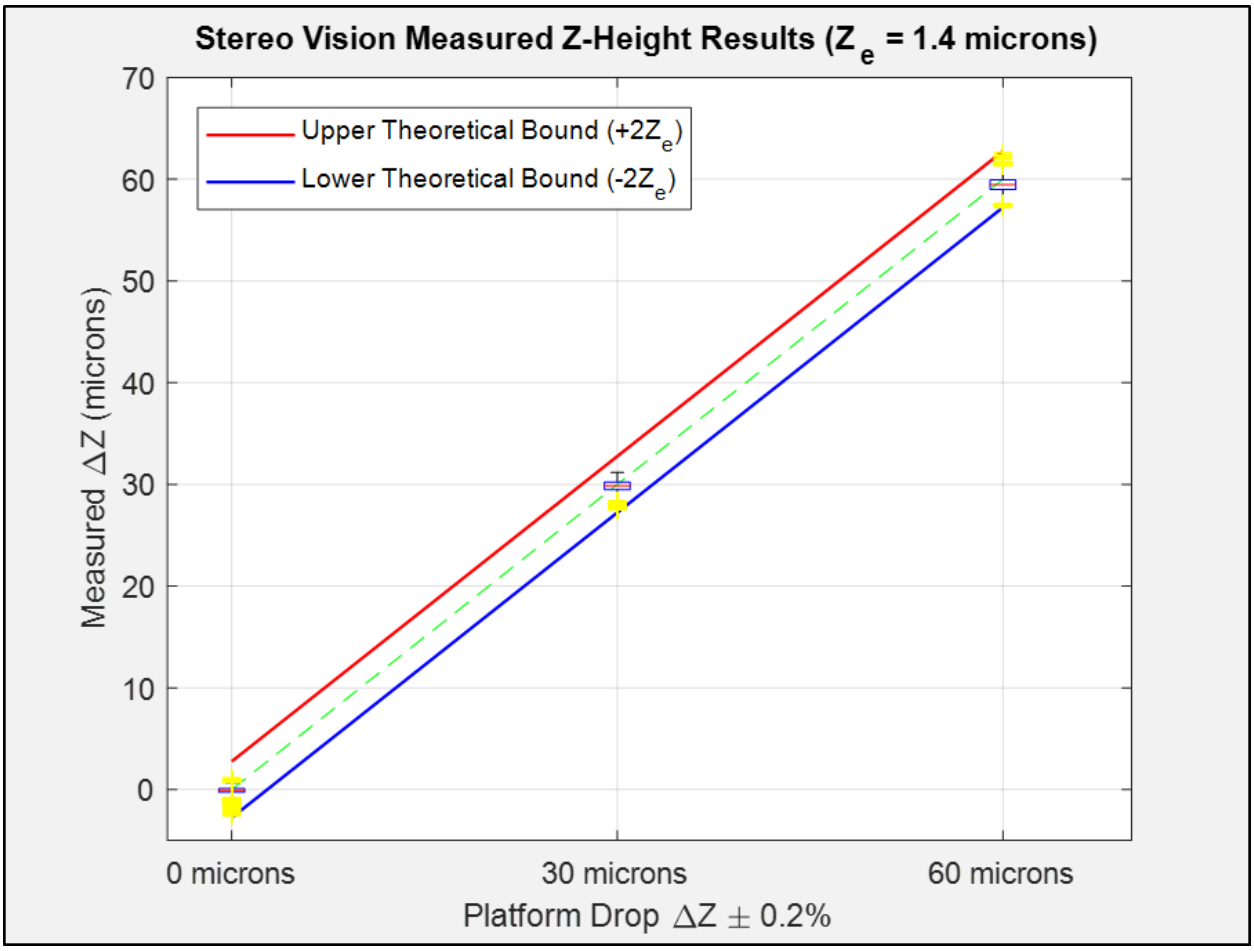

Figure 2.8: Plot of experimental ΔZ data with corresponding maximum and minimum bounds provided by the theory (ε = 0.073 pixel, min(ΔD) = 0.063 pixel, B = 687 mm, Z = 600 mm). The 8,892 measurements made at each platform position are displayed as boxplots for convenience (yellow "+" indicates outliers).

The primary reason for developing an approximation of the extreme limits of a stereoscopic measurement system is to establish a confidence interval that can be applied to all measurement results. In reality, it can be seen that the z-height measurement data is normally distributed, with a mean and standard deviation of -0.09 ± 0.33 µm, 29.81 ± 0.56 µm, 59.46 ± 0.72 µm for platform drops of 0 µm, 30 µm, and 60

μm, respectively (where 0 μm indicates correlation with a repeat image pair at the nominal platform position). This means most measurements were accurate within $\pm Z_e/2$. However, the critical observation is that all measurement data, including outliers, falls within the range predicted by the closed-form approximation. Based on this result, it is logical to conclude that we have developed a valid model for predicting the extent of stereoscopic z-height measurement error for a particular vision system. It should be noted that failure to include the calibration reprojection error term would cause approximately 25% of the z-height measurement data to fall outside of the predicted range.

In-Situ Layer-Wise 3D Surface Measurements in Metal SLM

The accuracy-verified prototype system was applied to monitor layer-wise 3D surface variation during the SLM fabrication of a turbine from Inconel 718. For this analysis, the cameras were equipped with 35 mm lenses to accommodate the entire 203 mm x 135 mm build platform in the ProX 320. With a spatial resolution of 48 μm/pixel, surface measurements were made every 3 pixels (144 μm) using 55-pixel subsets. According to the validated closed-form approximation for stereoscopic measurement accuracy, pointwise z-height measurements are reliable within ±6.0 μm.

The layer-wise z-height data obtained from monitoring the turbine build exposed a significant amount of inherent variation within the SLM build process. This becomes immediately apparent when looking at a side-by-side comparison of powder spread surface variation from the beginning and end of the build (Figure 2.9). The ProX 320 utilizes a silicone spreader blade to distribute powder onto the build platform. Over the course of a build, the edge of the silicone material accumulates damage from repetitively encountering sharp metal surfaces during the spreading process. The result is that by the

end of this particular build, the z-height variation within the spread powder surface was nearly three-times greater than the 30 µm layer thickness used to construct the turbine. On a layer-by-layer basis, there is even more to be learned about the SLM process.

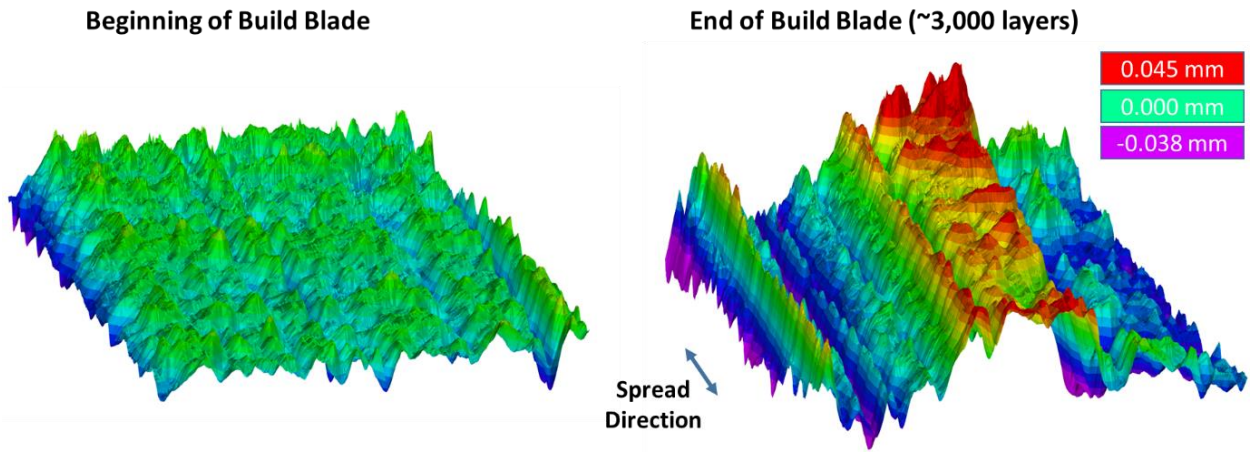

Figure 2.9: Side-by-side comparison of powder spread surface variation from before and after the build over the same 70 mm x 90 mm area.

Figure 2.10 shows a side-by-side comparison of z-height data from typical build layers with right and left spread directions. The first noteworthy phenomenon is that powder accumulates near part edges as a function of spread direction. More specifically, the silicone spreader blade tended to deposit isolated mounds of powder immediately after passing over the fused part geometry. Although it is not clear why this behavior occurs, it is possible that lifted part edges impart mechanical forces on the blade that persist due to the visco-elastic properties of the silicone material.

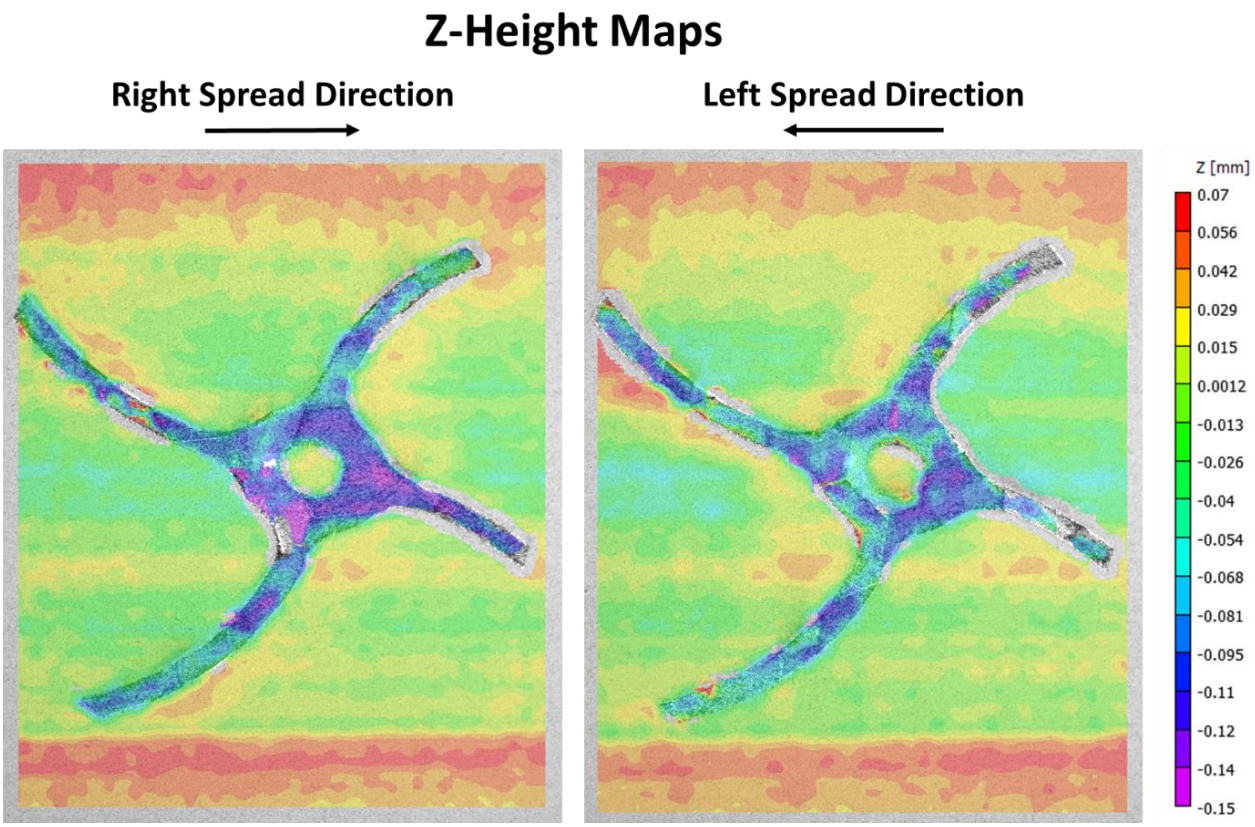

Figure 2.10: Side-by-side comparison of build layers with right and left spread directions; observations include directional powder accumulation, fused material densification, and a broad band of depressed powder across the span of the fused region due to thermal expansion of the silicone spreader blade.

The second phenomenon illustrated in Figure 2.10 is that the fused material region is considerably depressed compared to the surrounding unfused powder, with a typical difference in elevation between 50 and 200 µm. The elevation disparity is clearly a function of material densification during the fusing process, when powder particles are melted and bonded to the solid structure below. While the concept of layer-wise material densification in PBF AM is not necessarily novel, it is revealing to observe systematic powder bed variations over six-times greater than the 30 µm layer thickness used in this build. These deep valleys result in subsequent powder layers that are significantly thicker

than expected, which contributes to insufficient material fusion and porosity in the final part.

Finally, Figure 2.10 reveals a broad band of depressed powder that developed parallel to the spread direction across the span of the fused material region. The unfused powder within this band is up to 60 µm lower than powder outside of the fused material region. A possible explanation for this phenomenon is that the silicone blade is picking up heat from the fused material and thermally expanding, thus pushing down into the powder bed as spreading occurs.

In addition to the powder surface observations described above, the layer-wise z-height data produced by the stereo measurement system uncovered anomalous process behavior that ultimately resulted in a noticeable surface defect in the final part (Figure 2.11). A deep gouge formed parallel to the spread direction and persisted over several layers due to a large particle sweeping back-and-forth across the powder bed. The particle eventually adhered to the part surface and the anomalous behavior disappeared. The disconcerting fact that this irregularity did not cause the build to abort emphasizes the need for in-situ monitoring in PBF AM. If not located on a visible surface, the defect would have gone undetected without this technique.

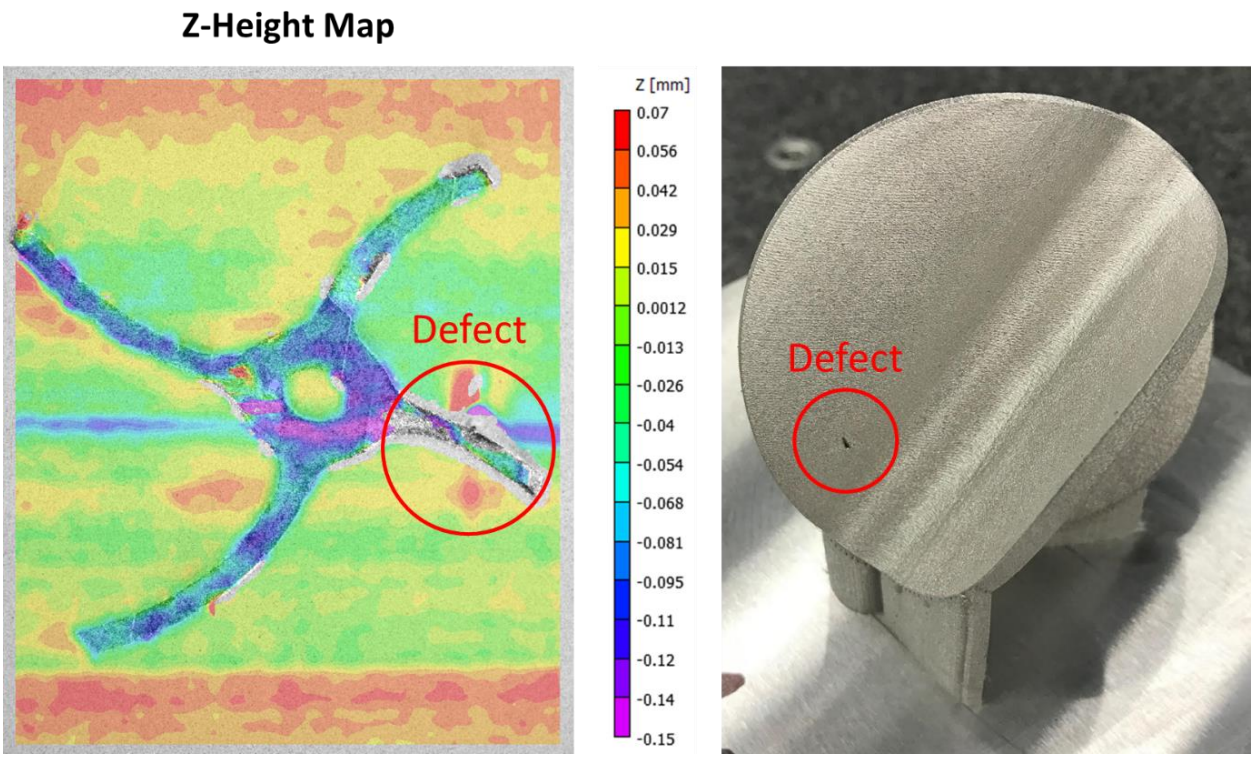

Figure 2.11: Anamolous process behavior showing a deep gouge in the powder bed and the resulting surface defect in the final part.

Conclusions

In this manuscript, we have demonstrated an accuracy-verified technique for monitoring the 3D build surface variation in metal SLM. The technique leverages a stereo vision system along with concepts and algorithms utilized in established high-precision optical surface measurement techniques, such as 3D DIC, to achieve z-height measurement accuracy on the order of one-tenth the spatial resolution of the camera system. Optimizations to optical configuration, lighting, and camera calibration can be made to further improve measurement capabilities in future system instantiations. With this level of measurement precision, it is possible to observe the subtle layer-wise build surface variations that contribute to anomalous behavior and consistency issues

associated with PBF systems. Documented observations include broad powder surface height variations, spreader bar wiper blade wear, interactions between powder spreading and part geometry, and powder irregularities linked to a focal build defect.

Future work will involve extending stereoscopic surface measurements into a set of build variance metrics that describe the PBF process zone. Applied powder layer thickness, material densification, and incremental build height can be calculated from layer-wise z-height when proper datum concepts are applied. Theoretically, these metrics are also useful for determining real-time parameter adjustments that address the inherent process variations exposed herein.

References

1. Tapia G, Elwany A (2014) A Review on Process Monitoring and Control in Metal-Based Additive Manufacturing. J. Manuf. Sci. Eng 136(6), 060801

2. King WE, Anderson AT, Ferencz RM, Hodge NE, Kamath C, Rubenchik AM (2015) Laser Power Bed Fusion Additive Manufacturing of Metals; Physics, Computational, and Materials Challenges. Applied Physics Review 2(4)

3. Spears TG and Gold SA (2016) In-process sensing in selective laser melting (SLM) additive manufacturing. Integrating Materials and Manufacturing Innovation (2016) 5(2)

4. Purtonen T, Kalliosaari A, Salminen A (2014) Monitoring and Adaptive Control of Laser Processes. Physics Procedia 56(2014):1218-1231

5. Bi G, Gasser A, Wissenbach K, Drenker A, Poprawe R (2006) Characterization of the Process Control for the Direct Laser Metallic Powder Deposition. Surface and Coatings Technology 201(6):2676-2683

6. Bi G, Shürmann B, Gasser A, Wissenbach K, Poprawe R (2007) Development and Qualification of a Novel Laser-Cladding Head with Integrated Sensors. International Journal of machine Tools and manufacturing 47(3):555-561

7. Lott P, Schleifenbaum H, Meiners W, Wissenbach K, Hinke C, Bultmann J (2011) Design of an Optical system for the In Situ Process Monitoring of Selective Laser Melting (SLM). Physics Procedia 12(2011):683-690

8. Craeghs T, Bechmann F, Berumen S, Kruth JP (2010) Feedback control of Layerwise Laser Melting using Optical Sensors. Physics Procedia 5(2010):505-514

9. Craeghs T, Clijsters S, Yasa E, Bechmann F, Berumen S, Kruth JP (2011) Determination of geometrical factors in Layerwise Laser Melting using optical process monitoring. Optics and Lasers in Engineering 49(2011):1440-1446

10. Doubenskaia M, Pavlov M, Grigoriev S, Tikhonova E, Smurov I (2012) Comprehensive Optical Monitoring of Selective Laser Melting. Journal of Laser Micro/Nanoengineering 7(3):236-243

11. Krauss H, Eschey C, Zaeh MF (2012) Thermography for Monitoring the Selective Laser Melting Process. Proceedings of the Solid Freeform Fabrication Symposium

12. Craeghs T, Clijsters S, Yasa E, Kruth JP (2011) Online Quality Control of Selective Laser melting. Proceedings of the 22nd Annual International Solid Freeform Fabrication Symprosium

13. Dunsky C (2014) Process Monitoring in Laser Additive Manufacturing. Industrial Laser Solutions

14. Wegner A, Witt G (2011) Process Monitoring in Laser Sintering using Thermal Imaging. Solid Freeform Fabrication: Proceedings, August 2011: University of Texas at Austin 2011

15. Cooke AL, Moylan SP (2011) Process Intermittent Measurement for Powder-Based Additive Manufacturing. Proceedings of the 22nd International SFF Symposium – An Additive Manufacturing Conference

16. Kleszczynski S, Jacobsmühlen J zur, Sehrt JT, Witt G (2012) Error Detection in Laser Beam Melting Systems by High Resolution Imaging. Proceedings of the 23rd Annual International Solid Freeform Fabrication Symposium

17. Colla et al. (2014) Monitoring Concepts for a 3D Printer Applied to Build a Human Outpost on the Moon. 16th International Conference on Computer Modelling and Simulation

18. Townsend A, Senin N, Blunt L, Leach RK, Taylor JS (2016) Surface Texture Metrology for Additive Manufacturing: A Review. Prec. Eng. 46(2016):34-47

19. Holzmond H, Li X (2017) In Situ Real Time Defect Detection of 3D Printed Parts. Journal of Additive Manufacturing 17(2017):135-142

20. Sutton MA, Orteu JJ, and Schreier H (2009) Image Correlation for Shape, Motion and Deformation Measurements. Springer, NY, USA. doi: 10.1007/978-0-387-78747-3

21. Wang YQ, Sutton MA, Ke XD, and Schreier H (2011) Error Assessment in Stereo-Based Deformation Measurements, Part I: Theoretical Developments for Quantitative Estimates. Exp. Mechanics 51(4):405-422

22. Wang YQ, Sutton MA, Ke XD, and Schreier H (2011) Error Assessment in Stereo-Based Deformation Measurements, Part II: Experimental Validation of Uncertainty and Bias Estimates. Exp. Mechanics 51(4):423-441

23. Hartley R and Zisserman A (2003) Multiple View Geometry in computer vision. Cambridge University Press. ISBN 0-521-54051-8.

Chapter 3

Layer-Wise Build Variance Metrics for Metal Powder Bed Fusion Additive Manufacturing

Daniel P. Mosher[1,2], Brian K. Bay[1,2]

[1]Oregon State University, Corvallis, Oregon

[2]Department of Mechanical, Industrial, and Manufacturing Engineering

mosherd@oregonstate.edu

Abstract

Powder Bed Fusion (PBF) techniques are Additive Manufacturing (AM) technologies that construct parts through the process of sequentially spreading and fusing thin layers of powder. Although high quality potential has been demonstrated in the realm of metal AM, improvements to the consistency and repeatability of these techniques is required before they can be reliably used as production solutions for quality critical industries. As the industry moves towards in-process control to reduce variability, there is a need for in-situ sensing systems that characterize process variation and analytical techniques for relating sensor data back to input parameters. This work extends in-situ stereoscopic measurement data to into layer-wise Build Variance Metrics (BVM) that describe the process zone permutations in PBF. We also describe how the resulting information can be used to perform in-process parameter adjustment with closed-loop feedback. The pointwise uncertainty associated with sample stereoscopic BVMs is estimated to be ±12.0 μm, while accurate x-y spatial reconstruction is observed for features above 480 μm in size through numerical simulation of spatial convolution effects. Improved performance can be achieved by increasing the effective spatial resolution of the camera system, enhancing image contrast, or both.

Introduction

Additive Manufacturing (AM) is the process of constructing parts through the incremental addition of material. Powder Bed Fusion (PBF) techniques, such as Selecting Laser Melting (SLM), are a subset of AM technologies that perform this task by sequentially spreading and fusing thin layers of powder. These techniques have recently

seen an increase in popularity, especially in the realm of metal AM, because they produce high-strength parts with higher feature resolution and tighter dimensional accuracy than wire or powder feed systems [1]. State of the art systems are even capable of fabricating functional metal components with shorter lead times and lower direct costs than traditional manufacturing methods [2]. However, the same layer-by-layer build process that gives metal PBF technologies their unprecedented speed and flexibility also creates tremendous challenges regarding quality assurance [2-4]. Although high quality potential has been demonstrated, improvements to the consistency and repeatability of these techniques is required before they can be reliably used as production solutions for quality critical industries [2-4]. Furthermore, for AM to really thrive in these industries, it has to be able to produce parts with less effort and in fewer iterations than traditional manufacturing methods.

Repeatability issues in PBF are due in part to a fundamentally variable layer construction process. Spreading and fusion layering operations have been shown to produce significant out-of-plane surface variation that can evolve throughout the course of a build [5-6]. Despite known variability, critical input parameters such as layer thickness, laser energy, scan speed, and scan pattern are held fixed over the entire build process [2]. A conceivably better approach would be to adjust the process in response to observed variations in layer thickness, which is known to directly impact final part properties [4]. For this to be realized, there is a need for in-situ sensing systems that characterize the complex and interdependent layering operations [7] and analytical methods that relate sensor data back to input parameters [8].

Researchers have recently demonstrated the use of in-situ metrology techniques to monitor 3D build surface variation in AM. Land et al. implemented a fringe projection system to monitor post-fuse powder surface variation in metal SLM with a relatively high vertical noise floor of 20 µm over a 100 mm^2 area [9]. Holzmond et al. showed that in-situ stereo vision could be used to identify defects in fused deposition modeling when a texturing agent is added [10]. However, neither of these approaches address the problem of characterizing powder bed system process variation in the context of the interdependent layering operations they employ. Additionally, the out-of-plane accuracy demonstrated by fringe projection techniques [9] would likely be insufficient for this work considering that characterizing the layer construction operations will require calculations that compound inherent measurement system error.

Sufficient description of the layer construction process requires the measurement and subsequent comparison of post-spread and post-fuse surface variation. For example, the thickness of an applied powder layer is determined not only by the variation of the post-spread powder surface, but also by the underlying variation in the fused surface from the prior layer. By the same logic, the material densification experienced during layer fusion will be a function of build surface variation measured before and after fusing occurs. These incremental build volume changes occur in what we are calling the PBF process zone, the interface between successive build surfaces. This work seeks the extraction of quantitative information that describes all permutations of the process zone (Figure 3.1), meaningful metrics that can be related to input parameters in powder bed systems.

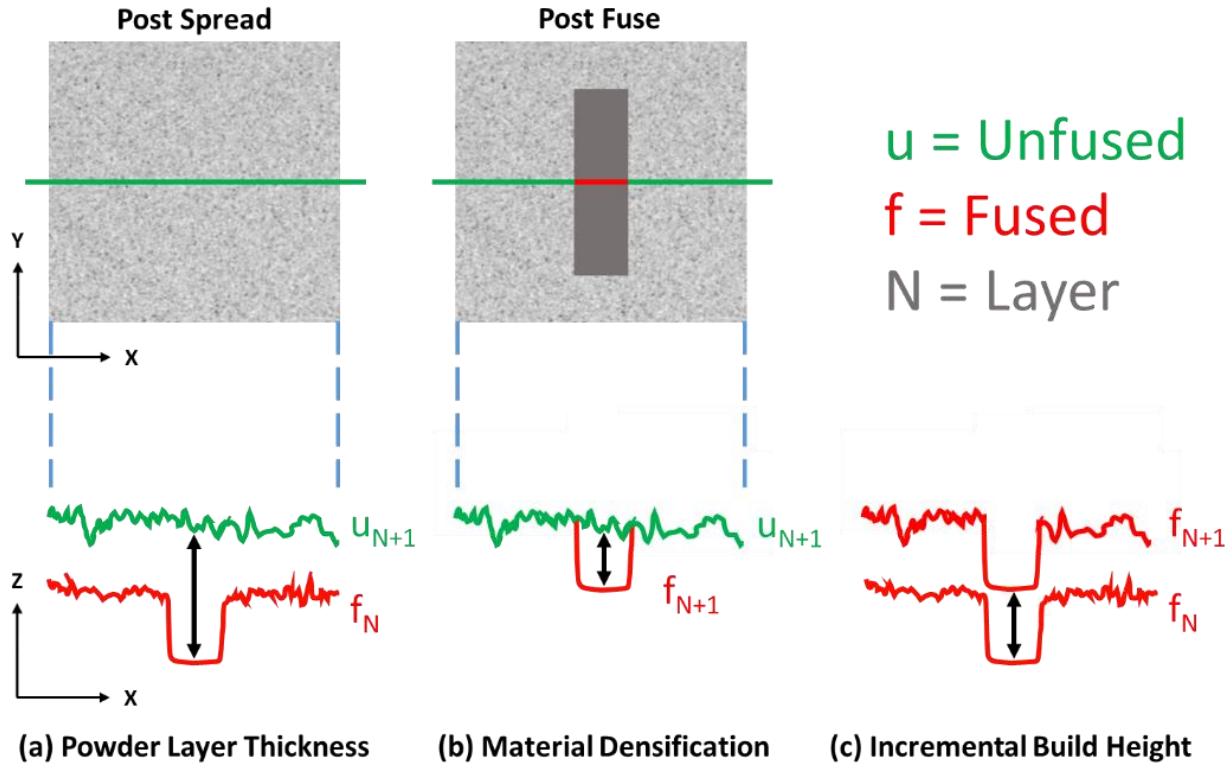

Figure 3.1: Illustration showing successive build surfaces, process zone permutations and corresponding build variance metrics. (a) Successive fused and unfused surfaces describe powder layer thickness (b) Successive unfused and fused surfaces describe material densification (c) Successive fused surfaces describe incremental build height.

In this manuscript, we extend in-situ stereoscopic build surface measurements in metal SLM to calculate local measures of powder layer thickness, material densification, and incremental build height. We are calling these measures Build Variance Metrics (BVMs). If appropriately applied, these metrics can be used to determine necessary real-time parameter adjustments to correct for observed in-process variation. Observations include spread-direction and geometry-dependent variation in powder layer thickness, inconsistent material densification, and discrepancies between measured and assumed build height based on nominal layer thickness values. A root of the sum of the squares (RSS) uncertainty analysis [11] is conducted to estimate the pointwise uncertainty in the

BVMs presented, and a numerical simulation is used to determine the spatial feature resolution limitations associated with stereoscopic surface reconstruction.

Materials & Methods

Experimental Setup

For this study, a stereo vision system was integrated into a ProX 320 (3D Systems) production metal SLM machine and used to acquire in-situ images of the build surface after spreading and again after fusing (Figure 3.2). The ProX 320 utilizes a silicone spreader bar to distribute powder onto a build platform before selectively fusing it with a laser energy source.

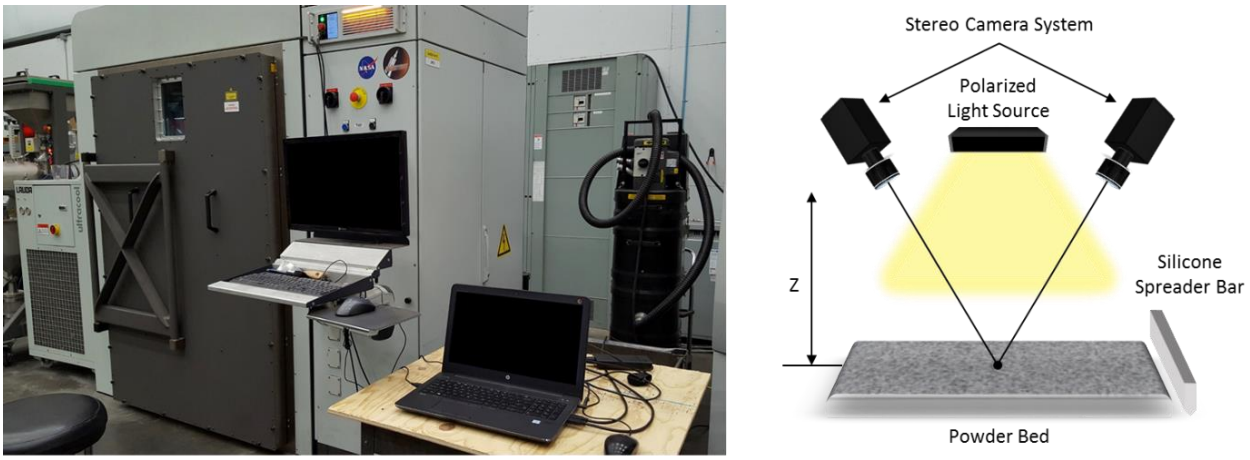

Figure 3.2: ProX 320 SLM machine and conceptual stereo integration plan.

The vision system employed two Grasshopper3 12MP USB 3.0 cameras with 4240 pixel x 2824 pixel resolution (3.1 µm pixel size) on a 1" format monochromatic CCD sensor (Point Grey). The cameras examined the build platform from above, through custom viewing windows designed to interface with pre-existing access ports (Figure 3.3). Inside of the chamber, a cross-polarized lighting scheme was implemented to adequately illuminate the powder bed and suppress reflections. With the cameras located outside of

the vacuum chamber to avoid extreme environmental conditions, the optical working distance was measured to be 600 mm. The precise baseline distance and relative camera angles were determined from the extrinsic calibration parameters. However, the distance between cameras was roughly 687 mm and the cameras were approximately 27º from vertical. In this configuration, the cameras were equipped with 35 mm lenses to accommodate the entire 203 mm x 135 mm build platform at a spatial resolution of 48 µm/pixel. At this resolution, images of metal powder and fused surfaces exhibit a locally unique surface pattern that supports the use of stereo image correlation to reconstruct 3D surface geometry.

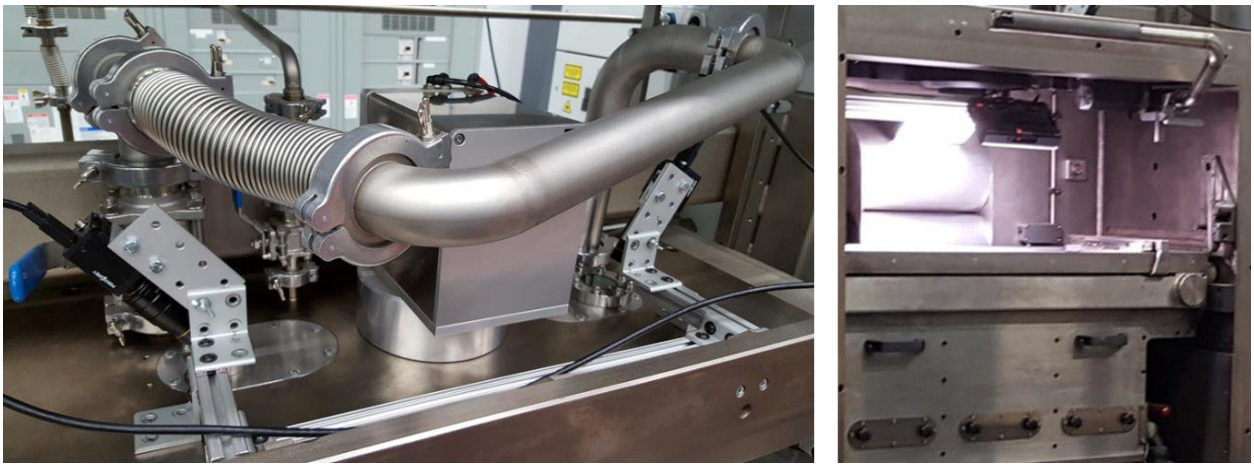

Figure 3.3: Actual vision system implementation with custom viewing windows (left) and polarized internal chamber lighting (right).

Figure 3.4 shows example images of the 102 mm x 76 mm sub-region of the build platform analyzed in this study. The extrusion-type geometry was constructed from stainless steel 316L with a particle size distribution (PSD) of 45 ± 15 µm. The nominal layer thickness for the build was set to 60 µm.

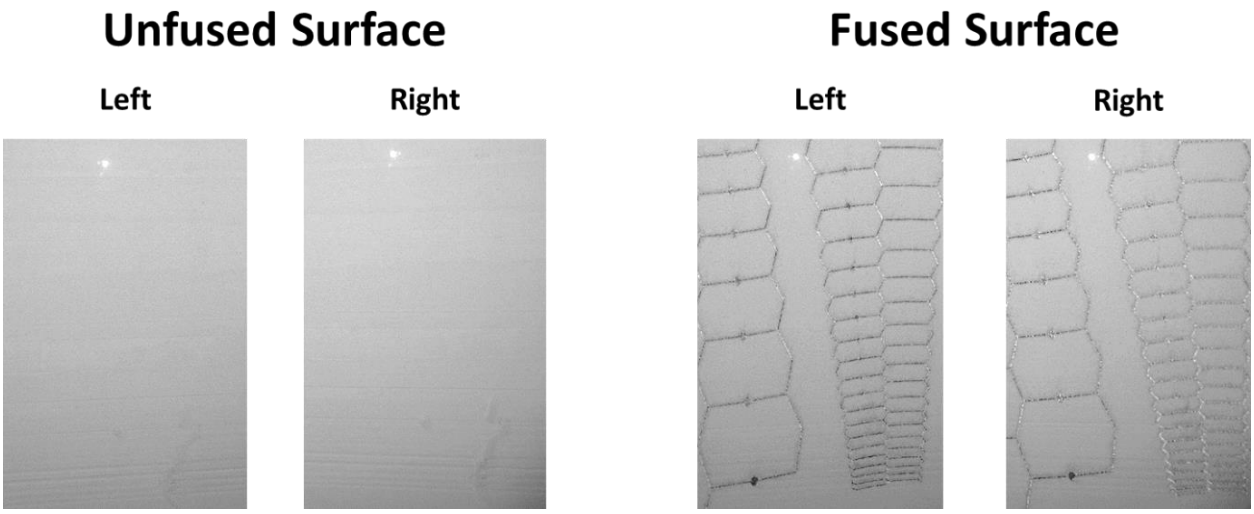

Figure 3.4: Example high-resolution images of unfused and fused stainless steel 316L powder surfaces (102 mm x 76 mm).

Stereoscopic Depth Extraction using 3D Digital Image Correlation

3D surface measurements were extracted from stereoscopic images of the build platform using 3D Digital Image Correlation (DIC) [12]. In traditional DIC applications, a white light speckle pattern is applied to the surface of the specimen to provide a locally distinguishable pattern for reliable tracking from image-to-image (Figure 3.5). In this application, the optical similarity of metal powder surfaces to white light speckle patterns is leveraged as a tracking mechanism to locate common features in stereo image pairs.

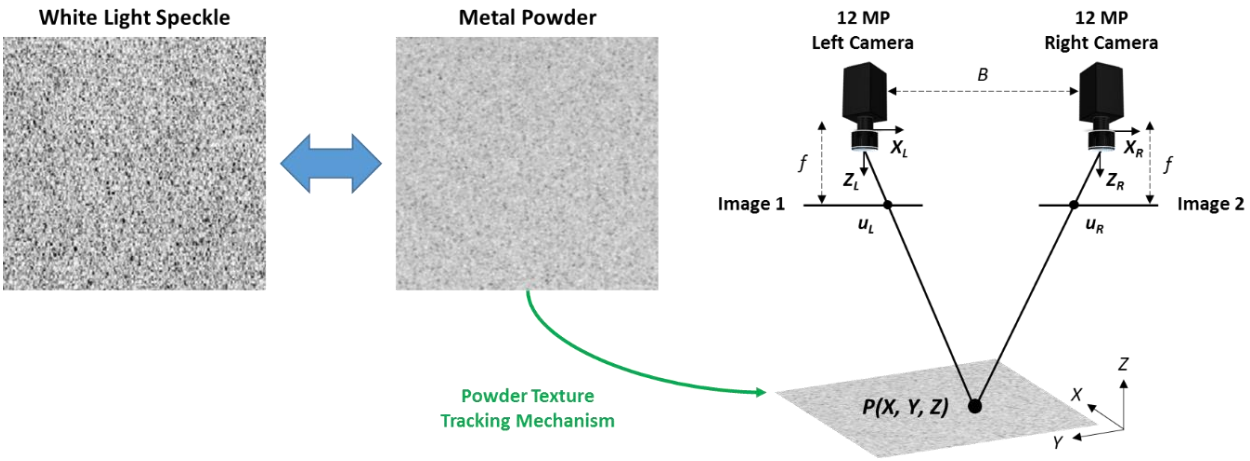

Figure 3.5: The optical similarity between illuminated metal powder and white light speckle is leveraged to extract 3D surface measurements from stereoscopic images of the SLM powder bed.

The commercial DIC measurement software Vic-3D (Correlated Solutions) was employed to perform stereo correlation and reconstruct 3D surfaces for both unfused and fused powder surfaces. Surface measurements were extracted within the analysis region at control points spaced by 5 pixels (~240 µm) using 55-pixel subsets. Stereo camera calibration is required to reconstruct 3D surfaces using Vic-3D. The system used in this study was calibrated using a standard Vic-3D dot grid target (17 x 14 dots with 6 mm spacing). The target was imaged at 40 different locations, orientations, and tilts within the shared camera field of view. Calibration of the prototype system for this study yielded a reprojection error (epipolar error) of 0.064 pixels. Reprojection error describes the average pointwise deviation from the ideal pinhole camera model in pixels, which can be used to estimate point correspondence errors between two images [13].

The output of the Vic-3D analysis is 3D point cloud information of the form $[X, Y, Z]$ in world metric coordinates. However, since the measurements were made according to a regularly spaced pixel grid (control points), the planar sampling location in world

coordinates will vary slightly from surface-to-surface due to platform drops and general build surface height variations. To address this discrepancy, the z-height data associated with each surface was resampled onto a consistent spatial grid using cubic spline interpolation at a spacing of 240 µm (code found in Appendix B). Registering the data in this way yields a comprehensive set of layer-wise z-height data of the form:

$$Z(X,Y)_{N,unfused}$$

and

$$Z(X,Y)_{N,fused}$$

where N is used to denote the build layer number. For visualization purposes, it is convenient to display the data as contour maps (Figure 3.6), which we refer to as "z-height maps". The registered z-height data can also be extended to calculate layer-wise variance measures that relate directly to Powder Bed Fusion (PBF) process parameters.

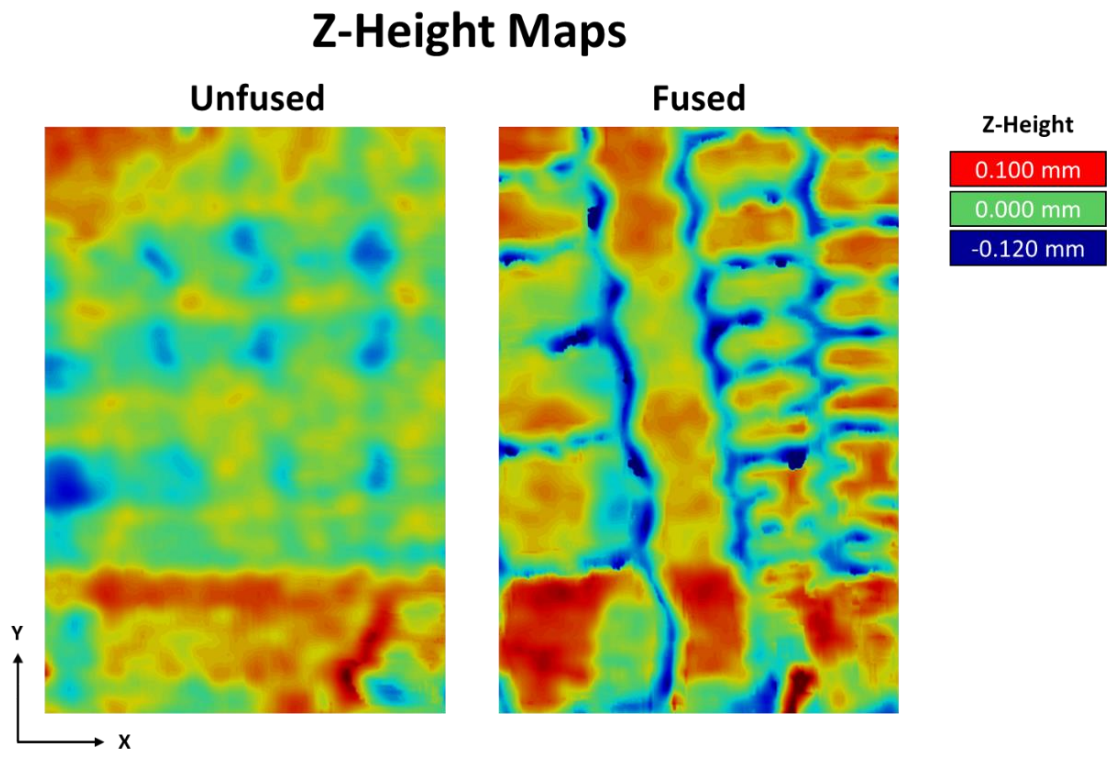

Figure 3.6: Z-height maps showing out-of-plane build surface variation in SLM as a color map; unfused maps display measured variation in post-spread surfaces and fused maps display measured variation in post-fusion surfaces (102 mm x 76 mm).

Build Variance Metrics (BVMs)

This section demonstrates the extension of in-situ stereoscopic z-height data to calculated layer-wise measures of powder layer thickness, material densification, and incremental build height. We also discuss potential ways the measures could be used to perform in-process parameter adjustments in PBF. We are calling these measures BVMs. Each BVM describes one permutation of powder bed process zone and thus assists in describing the layer construction operations (Figure 3.7).

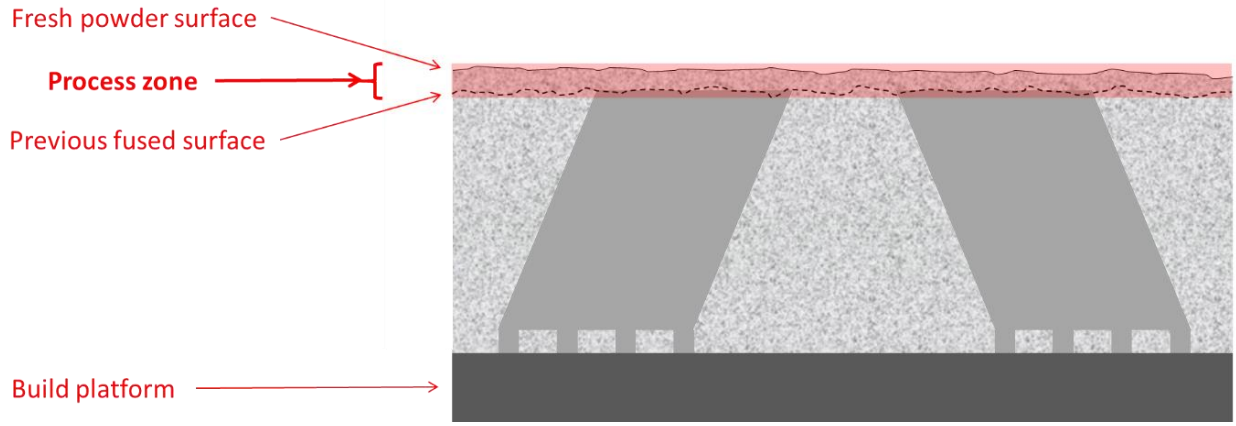

Figure 3.7: Illustration showing cross-section view of the powder bed and developing part, where successive build surfaces define the process zone. We seek accurate characterization of all process zone permutations to fully describe PBF AM.

Powder Layer Thickness

Powder layer thickness is a critical process parameter in PBF. The thickness of an unfused powder layer impacts requirements for laser power, scan speed, and scan pattern [4]. Due to known surface variations in PBF (5-6, 9), powder layer thickness is unlikely to remain consistent and uniform throughout the course of a build. When unaccounted for, deviations in layer thickness significantly impact the mechanical properties of parts in metal SLM [14]. With in-process measurements of powder layer thickness, dependent input parameters could be adjusted as a function of observed variations to mitigate these effects. In this section, we show how layer-wise measurements of powder layer thickness can be extracted from in-situ stereoscopic z-height data.

The thickness of applied powder at layer N can be calculated using z-height data acquired before and after the powder spreading operation. Mathematically, the definition for extracting powder layer thickness from z-height data is written as follows:

$$T(X,Y)_N = Z(X,Y)_{N,\,unfused} - Z(X,Y)_{N-1,fused} + \Delta Z_{platform}$$

where $T(X,Y)_N$ is the thickness of applied powder at layer N, $Z(X,Y)_{N,unfused}$ is the measured variation in the post-spread powder surface at layer N, $Z(X,Y)_{N-1,fused}$ is the z-height variation in the fused powder surface at layer $N-1$, and $\Delta Z_{platform}$ is the distance the platform drops before spreading occurs. Figure 3.8 illustrates the concept of using the fused powder surface profile from the previous layer as an updating datum for calculating the actual thickness of a freshly applied powder layer. Depending on the accuracy and repeatability of the build platform in the printer, $\Delta Z_{platform}$ can either be determined from system specifications or measured experimentally. In the case of the ProX 320 SLM machine used in our study, adjustment of the build platform is highly controlled and known within a typical accuracy of ±0.2% of the adjusted distance. Therefore, the assumption for this study was that the build platform consistently dropped by the nominal 60 µm layer thickness.

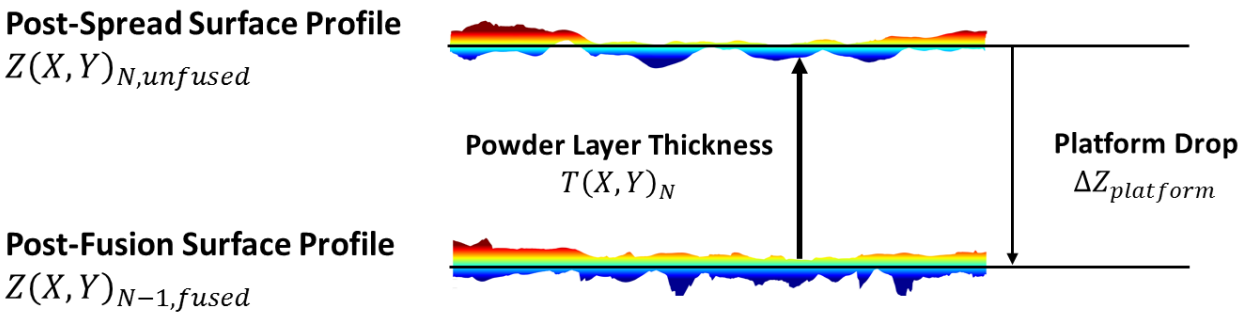

Figure 3.8: Datum relationships used to calculate a measure of spatially resolved powder layer thickness from stereoscopic z-height data measured before and after the PBF spreading operation.

Figure 3.9 shows example powder layer thickness maps calculated from SLM build data for each spread direction. In these maps, colors indicate the measured thickness of applied powder at specific locations across the build platform. The first thing we notice when analyzing the maps is that applied layer thickness varies considerably over the

analysis region. Measured values range from 20 µm to 200 µm, or one-third to over triple the intended 60 µm nominal thickness. We can also deduce that thick powder regions generally correspond to areas above fused part surfaces. This is likely a function of material densification experienced during the previous fusion operation, which is corroborated by the fact that the approximate fused part geometry is outlined in the thickness map. In contrast to the regions of thick powder seen in Figure 3.9, there are clear pockets of undercoating that occur in several locations across the powder bed. Further, the locations where undercoating occurs tend to shift as a function of spread direction and part geometry.

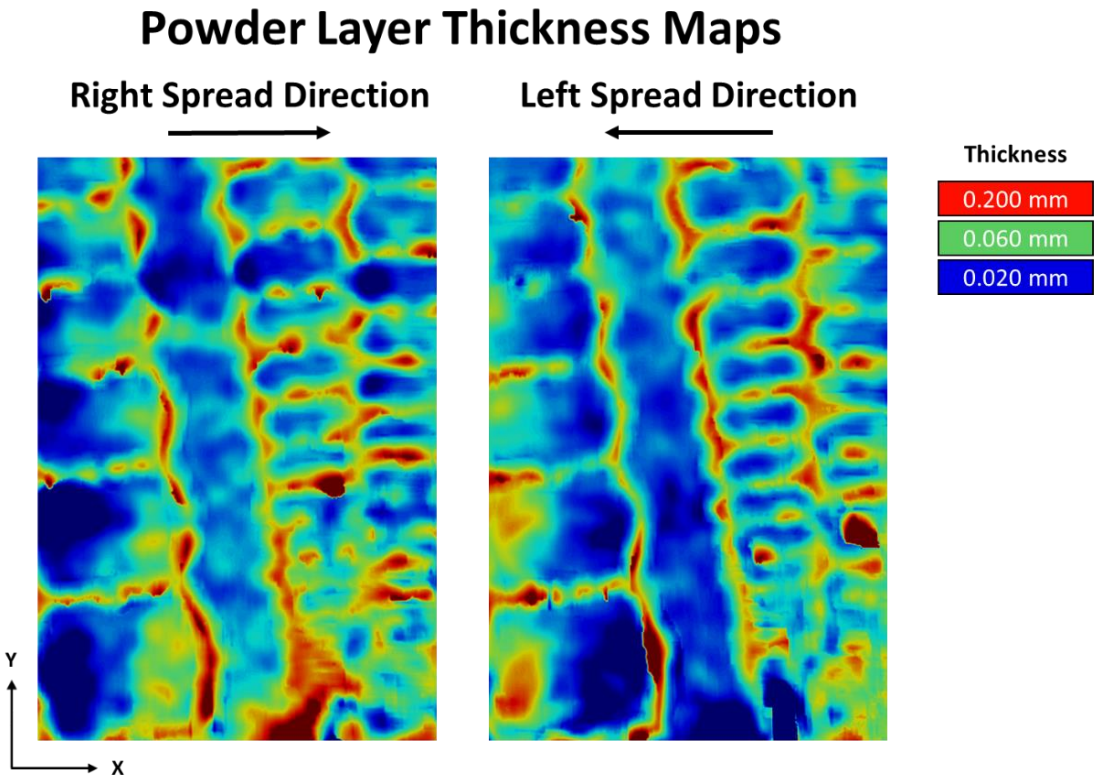

Figure 3.9: Powder layer thickness maps extracted from sample SLM build data for both spread directions (102 mm x 76 mm).

Based on this information, the optimization of input parameters, such as laser energy, based on an assumed layer thickness seems decidedly sub-optimal. The information provided by powder layer thickness maps could instead be used to spatially adjust laser power, scan speed, and scan pattern as a function of available fusible material. Localized optimization of these parameters could theoretically improve mechanical properties [14], reduce porosity [15] and improve surface roughness [16] in PBF parts.

Material Densification

Material densification in PBF is a function of laser power, scan speed, scan pattern, layer thickness, and spread density [4]. Since we now have the ability to measure local layer thickness values, material densification information could be used to provide feedback to parameter adjustments we make according to powder layer thickness maps. It can also provide insight into difficult to measure characteristics, such as spread density [17]. In this section, we show how layer-wise measures of material densification can be extracted from in-situ stereoscopic z-height data.

The change in build surface height due to material densification at layer N can be calculated by taking the mathematical difference between z-height data measured before and after the fusing operation occurs:

$$D(X,Y)_N = Z(X,Y)_{N,\,unfused} - Z(X,Y)_{N,fused}$$

where $D(X,Y)_N$ is the out-of-plane material densification due to fusion at layer N, $Z(X,Y)_{N,\,unfused}$ is the measured variation in the post-spread powder surface at layer N, and $Z(X,Y)_{N,fused}$ is the measured variation in the post-fusion powder surface at layer N.

Figure 3.10 shows example material densification maps calculated from SLM build data for each spread direction. In these maps, colors indicate the change in build surface

height due to material densification at specific locations across the build platform. As expected, larger amounts of densification occur within the vicinity of the scanned section geometry. However, it is less expected that densification in these regions varies parabolically from 120 µm at the center to 60 µm near the edges. Depending on whether the profile extends beyond the part boundary, this parabolic densification behavior could introduce systematic porosity gradients within fused part geometries [15] or contribute to surface roughness issues commonly associated with PBF parts [16]. In either case, accounting for this variation during parameter optimization would likely improve final part quality.

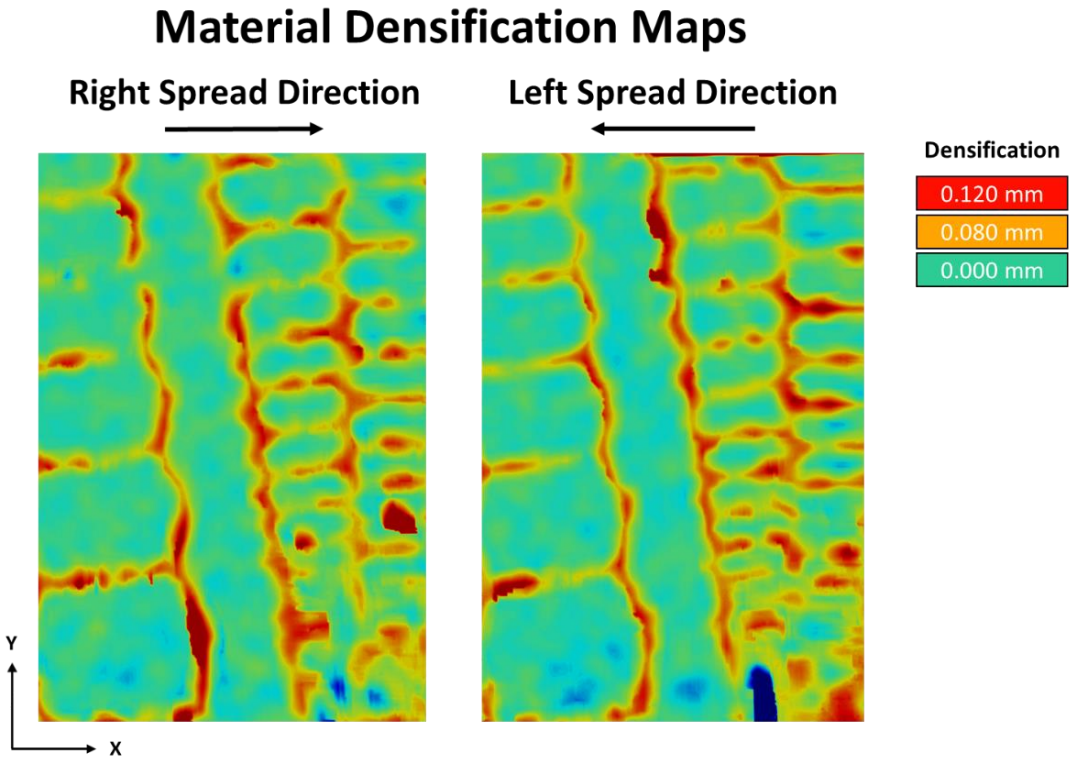

Figure 3.10: Material densification maps extracted from sample SLM data for both spread directions (102 mm x 76 mm). Evidence of part curl due to residual stress buildup can be seen in near the bottom right-corner of the map.

Figure 3.10 also displays evidence of part curl associated with the build-up of residual stresses [18]. In the bottom right-corner of the densification map, we can see that the build surface height changes are in the opposite direction as expected. From the raw images in Figure 3.3, it becomes apparent that there is an elevated mound of powder that has formed within this vicinity.

In addition to identifying irregular process behavior, the information in material densification maps could be used to iteratively optimize the adjustments made to input parameters according to powder layer thickness maps. The feedback provided by densification maps could be used to determine if particular parameter adjustments were insufficient, excessive, or on target. In this theoretical control system, powder layer thickness and material densification maps would effectively function as opposite ends of a feedback loop to control the PBF process. The configuration could be used to vastly decrease the number of iterations required to optimize process parameters and provide the foundation for a machine learning approach to PBF process control.

Incremental Build Height

Incremental build height combines layer-wise measurements of powder layer thickness and material densification to provide a high-level evaluation of build performance. While localized optimization of process parameters is being conducted at the layer level, incremental build height measurements can be used to assure the build is progressing towards a successful finish. In this section, we describe a method for extracting a layer-wise measure of incremental build height from in-situ stereoscopic z-height data.

We can calculate a measure of incremental build height by considering the effect of material densification in combination with measured powder layer thickness. For conceptual purposes, we can mathematically define a so-called fused layer thickness that represents the incremental addition of material to the build volume following both layering operations (spreading and fusing):

$$F(X,Y)_N = T(X,Y)_N - D(X,Y)_N$$

where $F(X,Y)_N$ represents the thickness of fused and unfused material added to the build volume during the creation of layer N, $T(X,Y)_N$ is the thickness of applied powder at layer N, and $D(X,Y)_N$ is the out-of-plane material densification experienced during fusion at layer N. From this result, we can construct a measure of the incremental build height at layer N by summing all fused layer thicknesses occurring up to that point:

$$H(X,Y)_N = \sum_{i=1}^{N} F(X,Y)_i$$

where $H(X,Y)_N$ is the measured incremental build height at layer N. Through substitution and simplification, the above result can be written conveniently in terms of measured z-height data:

$$H(X,Y)_N = \sum_{i=1}^{N} \left[Z(X,Y)_{i,fused} - Z(X,Y)_{i-1,fused} + \Delta Z_{platform} \right]$$

where $Z(X,Y)_{i,fused}$ and $Z(X,Y)_{i-1,fused}$ are the measured variation for each post-fusion powder surface from layer 1 to N, $Z(X,Y)_{0,fused}$ is the platform surface variation, and $\Delta Z_{platform}$ is the distance the platform drops before spreading occurs. For this study, platform variation is assumed to be negligible, so $Z(X,Y)_{0,fused}$ becomes an array populated with zero values.

Figure 3.11 shows incremental build height measurements according to the above equation juxtaposed against the incremental build height resulting from a perfect process producing nominal 60 µm layers. The side-by-side comparison exposes significant discrepancies between assumed and measured values both on a layer-by-layer basis and over the course of several layers. After seven layers, the height of the as-built geometry is lower than expected by approximately 100 µm. Depending on tolerance requirements, the accumulation of these deviations could quickly cause a part to go out of specification.

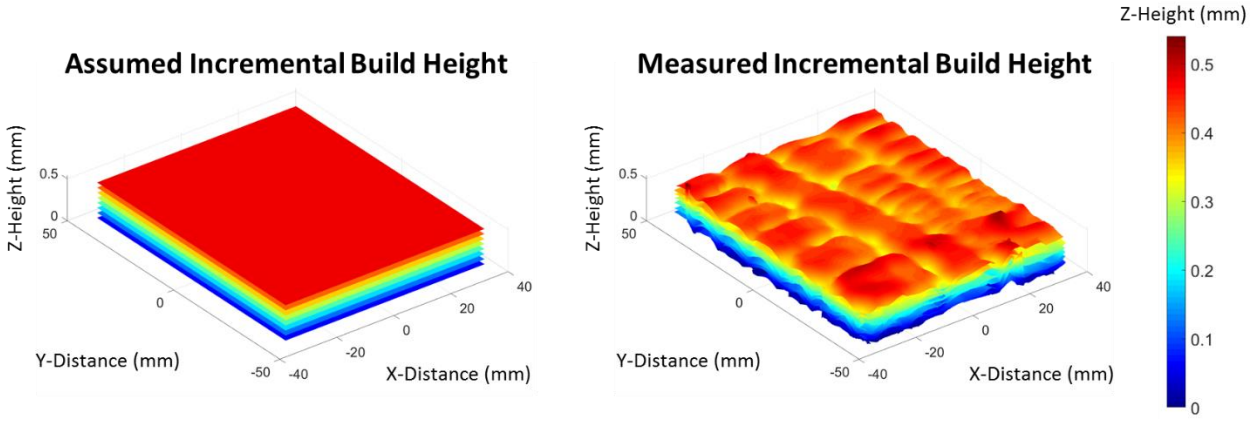

Figure 3.11: Incremental build height measurements provide a high-level indication of process performance. When not accounted for, deviations from expected build height perpetuate the knowledge gap between process inputs and outputs, and contribute to repeatability issues in PBF AM.

In a passive application, incremental build height measurements can be used to monitor long-term trends, evaluate the fidelity of as-built layers compared to design geometry, and accurately document the 3D location of observed defects within the build volume. However, they could also be used to determine real-time adjustments to nominal layer thickness values that account for discrepancies in build height throughout the course of the build.

Stereoscopic Z-Height Measurements and Metric Uncertainty

The z-height data and related BVMs metrics presented in this manuscript will contain error due to uncertainties in both the stereo correlation and calibration processes. Rigorous methods for comprehensively evaluating the sources of measurement error associated with generic stereo-based systems have been demonstrated [19-20], however they require extensive characterization and Monte Carlo experimentation to evaluate individual system configurations at a level of detail which is both unnecessary for this application and impractical for the streamlined environment of AM. What we desire is a convenient design tool that will enable the specification of appropriate system components as a function of desired performance and constraints. Therefore, this section aims to demonstrate an alternative method for conservatively estimating the z-height measurement performance of a stereo system according to the primary design variables. We perform an uncertainty analysis on the stereoscopic depth extraction process using a standard root of the sum of the squares (RSS) approach [11]. Then we use the approach to approximate the error associated with the z-height data and related BVMs presented in this work. The derived closed-form result can also be applied to specify system components and configurations according to desired performance.

In the RSS approach, an estimation of the total uncertainty associated with the calculated result $R = f(x_1, x_2, \dots, x_n)$ can be obtained from the uncertainties of the individual variables:

$$\omega_R = \left(\sum_{i=1}^{n} \left[\omega_{x_i} \frac{\partial R}{\partial x_i} \right]^2 \right)^{1/2}$$

where ω_R is the estimate of the total uncertainty in the calculated result R, ω_{x_i} is the estimate of the uncertainty in variable x_i, and $\partial R / \partial x_i$ is the sensitivity coefficient for the variable x_i. From the geometry in Figure 3.12, we can determine the relationship between a measured stereo pixel disparity D and the corresponding distance Z for an idealized stereo vision system without misalignment, relative rotations, or lens distortions, such that resulting stereo image pairs are rectified:

$$Z = \frac{Bf}{D}$$

where B is the baseline distance between cameras and f is the lens focal length. While this rectified geometry does not directly reflect the angled system implemented in this study, it also does not misinform the relationship between depth and disparity for the purposes evaluating uncertainty associated with stereo depth extraction. Image rectification is an established method in computer vision for simplifying the stereo depth extraction process in which stereo calibration and image interpolation errors contribute to disparity measurement uncertainty [12]. In the present case, we are effectively performing a virtual system rectification as an alternative to subsequently rectifying stereo image pairs during post-processing. Therefore, the errors associated with stereo calibration and image interpolation will need to be included in our estimate for disparity measurement uncertainty as would be the case with an equivalent post-processing rectification procedure [12].

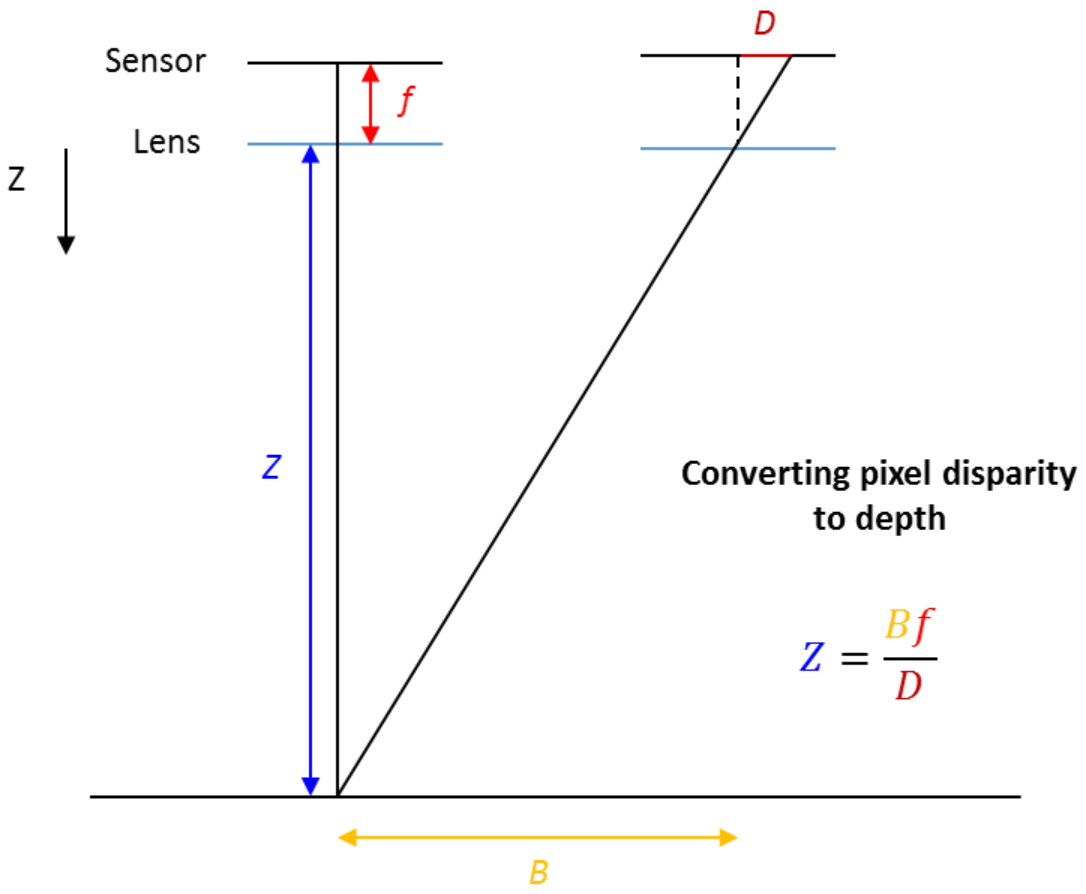

Figure 3.12: Idealized parallel optical axes stereo system geometry; where Z is the perpendicular distance from the camera system to the target (meters), f is the lens focal length (meters), B is the baseline distance between cameras (meters), and D is the disparity between common features in stereo images (pixels).

Plugging the depth-to-disparity relationship into the RSS yields the factors that contribute to z-height measurement uncertainty for a rectified stereo vision system:

$$\omega_Z = \left(\left[\omega_{Z_D} \frac{Bf}{D^2} \right]^2 + \left[\omega_{Z_B} \frac{f}{D} \right]^2 + \left[\omega_{Z_f} \frac{B}{D} \right]^2 \right)^{1/2}$$

where ω_Z is the estimate for z-height measurement uncertainty, ω_{Z_D} is the estimate of the uncertainty in the stereo pixel disparity D, ω_{Z_B} is the estimate of the uncertainty in the baseline distance B, and ω_{Z_f} is the estimate of the uncertainty in the camera focal length f. While this formulation is useful for isolating the sensitivity associated with absolute

stereo pixel disparity, it is difficult to interpret in a physical sense. A more practical arrangement would replace D with relevant system design variables. An equivalent version of the above equation can be written as follows:

$$\omega_Z = \left(\left[\omega_{Z_D} \frac{Z^2}{Bf} \right]^2 + \left[\omega_{Z_B} \frac{Z}{B} \right]^2 + \left[\omega_{Z_f} \frac{f}{B} \right]^2 \right)^{1/2}$$

where Z is the distance from the stereo vision system to the measurement plane (optical working distance). In this more intuitive form, we can see that the first term contains all of the relevant design variables. Also, since a rectified system geometry was used, uncertainties associated with determining B and f through stereo calibration will ultimately contribute to disparity measurement uncertainty as well [12]. Furthermore, we see that the second and third terms have relatively low sensitivity coefficients compared to the first, which means including the calibration uncertainty in the first term will actually produce a conservative estimate. Therefore, we disregard the contribution of the final two terms and arrive at the following approximation for stereoscopic z-height measurement uncertainty:

$$\omega_Z = \left[\omega_{Z_D} \frac{Z^2}{Bf} \right]$$

To realistically approximate stereoscopic depth extraction error for angled systems using our rectified system geometry, the uncertainty variable ω_{Z_D} must include errors associated with both sub-pixel interpolation and stereo camera calibration [12]. The combined result also needs to be converted to consistent units, which can be done by multiplying the uncertainty estimates by the sensor pixel size scaling factor:

$$\omega_{Z_D} = (\omega_i + \omega_\varepsilon) s_p$$

where ω_i is the uncertainty in sub-pixel interpolation of discrete digital image data for stereo matching, ω_ε is the uncertainty in calibration given by the reprojection error, and s_p is the sensor pixel size. A conservative estimate of 1/16th of a pixel is obtained for ω_i by evaluating factors that contribute to sub-pixel interpolation error [12], including subset size, stereo angle, and the sub-optimal nature of the texture in images of metal powder surfaces being leveraged to perform template matching. The remaining values used to approximate stereoscopic z-height measurement uncertainty for the system used in this study are found in Table 3.1.

Table 3.1: Predicted z-height measurement uncertainty for the stereo vision system and the relevant stereo camera parameters to perform the approximation.

ω_Z	Z	B	f	ω_i	ω_ε	s_p
±6.0 µm	600 mm	676 mm	35 mm	0.063 pixel	0.064 pixel	3.1 µm/pixel

The result indicates a total uncertainty of ±6.0 µm for the z-height measurements extracted from each stereo image pair. In other words, the out-of-plane measurement uncertainty associated with each z-height map is ±6.0 µm. To determine how this impacts the accuracy of the presented BVMs, we will conservatively assume the worst-case pointwise error for each z-height measurement. In this case, the uncertainty in each BVMs would be equal to the product of the z-height measurement uncertainty and the number of z-height maps used to perform the calculation. By this logic, since each BVMs is calculated using data from two z-height maps, the worst-case uncertainty associated with the results is ±12.0 µm. If we also consider the 0.2% typical uncertainty in ProX 320 build platform adjustments, then the uncertainty in both powder layer thickness and fused layer thickness would include an additional ±0.1 µm. Although the contribution from platform position is not significant in this study, it is still recommended that the effect of platform

accuracy is considered when determining the uncertainty of BVMs. This is particularly relevant in cases where platform position is less reliable or unknown and needs to be measured experimentally.

Considerations Regarding Spatial Feature Resolution in Reconstructed Surfaces

The process of using template (subset) matching to measure pointwise disparities in stereoscopic images will ultimately cause the resulting 3D surface data to experience a spatial smoothing effect during reconstruction similar to convolution [21] in image processing. In DIC, spatial convolution is commonly described as the loss of feature resolution in reconstructed surfaces incurred as a function of increasing subset size and measurement spacing [12]. In the previous section, the absolute pointwise error due to subset-based stereoscopic depth extraction was evaluated, then used to define an uncertainty interval for the BVMs presented in this study. Here we consider practical limitations associated with the feature resolution of stereoscopically reconstructed powder surfaces.

In addition to subset size and measurement spacing, the impact of feature smoothing in DIC will also depend on characteristics of the actual surface being measured. For this reason, it is difficult to directly quantify the error associated with spatial smoothing for generalized surface reconstruction. Therefore, we will utilize a numerical simulation to demonstrate what the effect of spatial convolution looks like for various scales of surface features encountered in AM powder beds. For simplicity, the simulation is performed along one planar dimension under the justification that convolution effects can be extrapolated dimensionally without loss of meaning [21].

To create the simulated surface shown in Figure 3.13, we first constructed a reasonable 2D representation of unfused powder surface height according to the PSD used in this study (45 ± 15 µm). This was done by generating a random vector of numbers in the range ±0.030 mm over a span of 2,125 pixels (equivalent to the analysis dimension perpendicular to the spread direction at a spatial resolution of 0.048 mm/pixel). Step functions of -0.100 mm were subsequently added to represent fused material regions of width 2.40 mm (50 pixels), 1.20 mm (25 pixels), 0.480 mm, and 0.240 mm (5 pixels) labeled A-D. The reconstructed surface shown in Figure 3.13 was generated by convolving the simulated surface with a gaussian window of 55 pixels and sample spacing of 5 pixels, representative of the stereo search parameters used in this study. The code for this simulation can be found in Appendix C.

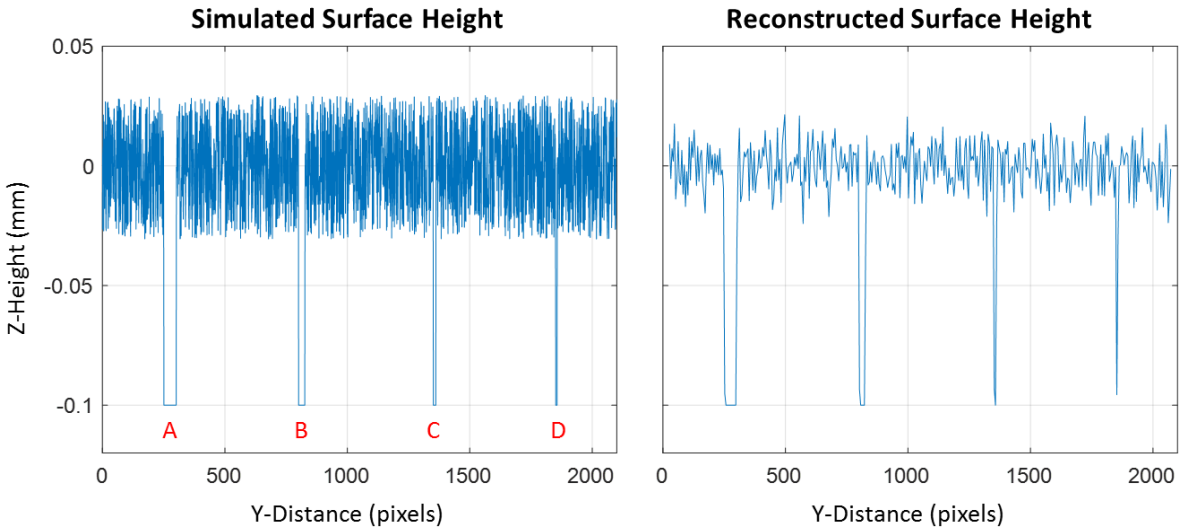

Figure 3.13: Simulated 2D representation of powder bed surface height and the resulting effect of spatial convolution during reconstruction for a Gaussian window of 55 pixels sampled every 5 pixels. High frequency random variation represents individual unfused particles and step functions represent fused powder regions of various widths (50, 25, 10, and 5 pixels: labeled A-D).

From the analysis, we can see that the results presented in this study are not suitable for evaluating surface roughness at the particle level. The high frequency particle-level variation is reconstructed with significant aliasing in the convolved surface. This is to be expected considering that our sampling rate of 5 pixels (240 μm) is 10-times below the Nyquist frequency of the variation representing individual unfused particle height (0.5 pixels or 24 μm). Therefore, we turn our attention to reconstruction of the individual step functions to determine spatial feature resolution limitations of the stereoscopic technique applied in this study.

The applied spatial convolution parameters had little effect on the reconstruction of the two largest fused regions (50-pixel and 25-pixel widths). Both features experienced only subtle smoothing in their bottom left corners and maintained consistent magnitudes and widths throughout the simulation. The 10-pixel region was reconstructed with accurate magnitude, but the thickness of the convolved feature decreased to a singularity at its base. This is not the case, however, for the smallest region (5-pixel width). For this region, we are beginning to significantly under-predict the densification. If the feature were any smaller, we would run the risk of not capturing it with these parameters. Based on these observations, it is reasonable to expect accurate detection of x-y surface features on the order of twice the measurement spacing, which corresponds to features of 480 um for the results presented in this work. Improving upon this performance can be accomplished by increasing the spatial resolution of the system, enhancing image contrast, or reducing measurement spacing. The first two implements will also benefit z-height measurement accuracy.

Conclusions

This manuscript demonstrated the extension of in-situ stereoscopic build surface measurements into local measures of powder layer thickness, material densification, and incremental build height in metal SLM. Furthermore, we described a strategy for using layer-wise BVMs to perform in-process parameter optimization with closed-loop control. Tools for evaluating BVM uncertainty and specifying appropriate system components as a function of desired performance and constraints were presented. The spatial limitations of the stereo measurement technique and suggestions for improving performance were also described. Furthermore, considering that only one-quarter of the field of view was analyzed in this work indicates that the 12 MP system is capable of higher performance over the same area.

Future work will involve implementation of the closed-loop process control strategy described in this manuscript. There is also value in volumetrically rendering in-situ stereoscopic surface data to produce a holistic snapshot representation of build variation. This quasi-tomographic stereovision-based approach to evaluation has the potential to assist with real-time quality assurance and part certification. Despite being demonstrated on stainless steel, the methods described herein are applicable to any powder material exhibiting sufficient surface contrast to perform stereoscopic image correlation.

References

1. Frazier WE (2014) Metal Additive Manufacturing: A Review. Journal of Materials Engineering and Performance 23(6)
2. Tapia G, Elwany A (2014) A Review on Process Monitoring and Control in Metal-Based Additive Manufacturing. J. Manuf. Sci. Eng 136(6), 060801

3. King WE, Anderson AT, Ferencz RM, Hodge NE, Kamath C, Rubenchik AM (2015) Laser Power Bed Fusion Additive Manufacturing of Metals; Physics, Computational, and Materials Challenges. Applied Physics Review 2(4)

4. Spears TG and Gold SA (2016) In-process sensing in selective laser melting (SLM) additive manufacturing. Integrating Materials and Manufacturing Innovation (2016) 5(2)

5. Craeghs T, Clijsters S, Yasa E, Kruth JP (2011) Online Quality Control of Selective Laser Melting. Proceedings of the 22nd Annual International Solid Freeform Fabrication Symposium

6. Kleszczynski S, Jacobsmühlen J zur, Sehrt JT, Witt G (2012) Error Detection in Laser Beam Melting Systems by High Resolution Imaging. Proceedings of the 23rd Annual International Solid Freeform Fabrication Symposium

7. Everton SK, Hirsch M, Stravroulakis P, Leach RK, Clare AT (2016) Review of in-situ process monitoring and in-situ metrology for metal additive manufacturing. J. Materials & Design 95(2016)

8. O'Regan P, Prickett P, Setchi R, Hankins Gareth, Jones N (2016) Metal Based Additive Layer Manufacturing: Variations, Correlations, and Process Control. Procedia Computer Science 96(2016):216-224

9. Land WS, Zhang B, Ziegert J, Davies A (2015) In-Situ Metrology System for Laser Powder Bed Fusion Additive Process. Procedia Manufacturing 1(2015)

10. Holzmond H, Li X (2017) In Situ Real Time Defect Detection of 3D Printed Parts. Journal of Additive Manufacturing 17(2017):135-142

11. Wheeler AJ, Ganji AR (2009) Introduction to Engineering Experimentation 3rd Edition. Englewood Cliffs, NJ, USA. ISBN 0131742760

12. Sutton MA, Orteu JJ, and Schreier H (2009) Image Correlation for Shape, Motion and Deformation Measurements. Springer, NY, USA. doi: 10.1007/978-0-387-78747-3

13. Hartley R and Zisserman A (2003) Multiple View Geometry in computer vision. Cambridge University Press. ISBN 0-521-54051-8

14. Sufiiarov VS, Popovich AA, Borisov EV, Polozov IA, Masaylo DV, Orlov AV (2017) The Effect of Layer Thickness at Selective Laser Melting. Procedia Engineering 174(2017):126-134

15. Zhang M, Sun CN, Zhang X, Goh PC, Wei J, Li H, Hardacre D (2017) Competing Influence of Porosity and Microstructure on the Fatigue Property of Laser Powder Bed Fusion Stainless Steel 316L. Proceedings of the 28th Annual International Solid Freeform Fabrication Symposium

16. Craeghs T, Clijsters S, Yasa E, Bechmann F, Berumen S, Kruth JP (2011) Determination of geometrical factors in Layerwise Laser Melting using optical process monitoring. Optics and Lasers in Engineering 49(2011):1440-1446

17. Jacob G, Donmez A, Slotwinski J, Moylan S (2016) Measurement of Powder Bed Density in Powder Bed Fusion Additive Manufacturing Processes. Measurement Science and Technology 27(2016)

18. Vlasea ML, Lane B, Lopez F, Mekhonstev S, Donmez A (2015) Development of Powder Bed Fusion Additive Manufacturing Test Bed for Enhanced Real-Time Process Control. Proceedings of the 26th Annual International Solid Freeform Fabrication Symposium

19. Wang YQ, Sutton MA, Ke XD, and Schreier H (2011) Error Assessment in Stereo-Based Deformation Measurements, Part I: Theoretical Developments for Quantitative Estimates. Exp. Mechanics 51(4):405-422

20. Wang YQ, Sutton MA, Ke XD, and Schreier H (2011) Error Assessment in Stereo-Based Deformation Measurements, Part II: Experimental Validation of Uncertainty and Bias Estimates. Exp. Mechanics 51(4):423-441

21. Cyganek B, Siebert JP (2009) An Introduction to 3D Computer Vision Techniques and Algorithms. John Wiley & Sons, NJ, USA. ISBN 047001704X

Chapter 4

Stereo-CT for Metal Powder Bed Fusion Additive Manufacturing: Volumetric Rendering of In-Situ Stereoscopic Build Surface Data

Daniel P. Mosher[1,2], Brian K. Bay[1,2]

[1]Oregon State University, Corvallis, Oregon

[2]Department of Mechanical, Industrial, and Manufacturing Engineering

mosherd@oregonstate.edu

Abstract

Metal Additive Manufacturing (AM) has the potential to revolutionize customized low-volume industries, but quality assurance issues continue to limit its widespread application. Due to high process variability, parts need to be individually assessed for the presence of defects that contribute to mechanical deficiencies. Current part-by-part inspection solutions are costly, time-consuming, and antithetical to the fundamental benefits of metal AM. This work investigates a streamlined alternative method for part evaluation that uses in-situ process variation as a proxy for defect formation. A stereo vision system is employed to monitor 3D build surface variation in a production Selective Laser Melting machine, then the stereoscopic data is used to produce quasi-tomographic representations of unfused surface variation, fused surface variation, and powder layer thickness. The volumetric stereo-CT data is shown to capture part lifting associated with residual stress formation and layer uniformity deviations linked to typical defects resulting from the PBF build process. Upon development of deterministic models that reliably correlate process variation observations to build outcomes, the stereo-CT approach can be useful as a real-time qualification tool for metal AM parts.

Introduction

Powder Bed Fusion (PBF) techniques, such as Selective Laser Melting (SLM), are Additive Manufacturing (AM) technologies that construct 3D parts through the sequential process of spreading and fusing thin layers of powder. This layer-by-layer approach to manufacturing offers tremendous advantages in terms of speed and flexibility compared to traditional manufacturing methods. One of the primary advantages is that AM requires

no custom tooling during fabrication, which enables streamlined production of complex geometries at an unprecedented rate. Current production powder bed systems are capable of producing functional metal components with shorter lead times and lower direct costs than traditional manufacturing methods [1]. However, the same layer-by-layer build process that provides AM with its unique advantages also creates tremendous challenges with regard to quality assurance [1-3]. Given that each individual layer presents an opportunity for the process to deviate from an expected outcome, it is nearly impossible to blindly predict how parts will perform from build-to-build, let alone from machine-to-machine. Additionally, it can be equally difficult to identify problematic parts during visual post-processing inspection. While some parts will contain clear focal defects, others will be rendered inadequate for their intended application due to inconspicuous mechanical deficiencies that also need to be recognized.

For AM to be successful in quality critical industries, mechanically insufficient parts cannot not be permitted to reach circulation. Mechanical deficiencies in AM parts are strongly correlated with the presence of porosity [4-6], surface roughness [6], and residual stresses [6-7]. While there are currently no consensus standards for non-destructive evaluation of AM parts, one of the tools universally involved in qualification efforts is x-ray computed tomography (XCT) for its ability to detect and document the location of common AM defects including porosity, voids, and high-density inclusions or contaminations [8]. Unfortunately, the slow speeds and high costs associated with XCT are antithetical to the fundamental benefits of AM [4]. As a result, these methods are generally limited in their applicability as a long-term solution for metal AM part

qualification. Ideally, there would be a qualification tool for identifying problematic parts more suited for the streamlined landscape of AM.

A potential alternative to post-production inspection using XCT is to evaluate in-situ build surface variation as a proxy for defect formation. Layer uniformity deviations caused by build surface variation are known to directly impact porosity [5, 9], surface roughness [10], and the mechanical performance of PBF parts [3, 5, 9]. Furthermore, extreme build surface variations, and the tendency of surfaces to lift and curl over time, have been linked to the formation of residual stresses in PBF parts [11]. Therefore, it is conceivable that all of the typical causes of mechanical deficiencies in AM parts can be identified by evaluating build variations and their effect on layer uniformity. Although robust deterministic models for how sensor data relates to defect formation will be required eventually, the first step is to establish tools and methodologies for measuring and visualizing process variation holistically throughout the build volume. Moreover, a method capable of providing the measurement information in real time is desirable.

In this manuscript, we describe the implementation of an in-situ stereo vision system to measure 3D build surface variation in a production SLM machine. We then describe a methodology for rendering stereoscopic surface measurement data volumetrically to produce a quasi-tomographic representation of process variation for both unfused and fused surfaces. In a similar fashion, stereoscopic data is used to produce a result that shows how powder layer thickness varies throughout the build volume (Figure 4.1). If appropriate models are developed to deterministically relate process variation to defect formation in powder bed systems, it is possible that this so-called stereo-CT method can

eventually supplant XCT as a faster and less-expensive alternative for AM part qualification.

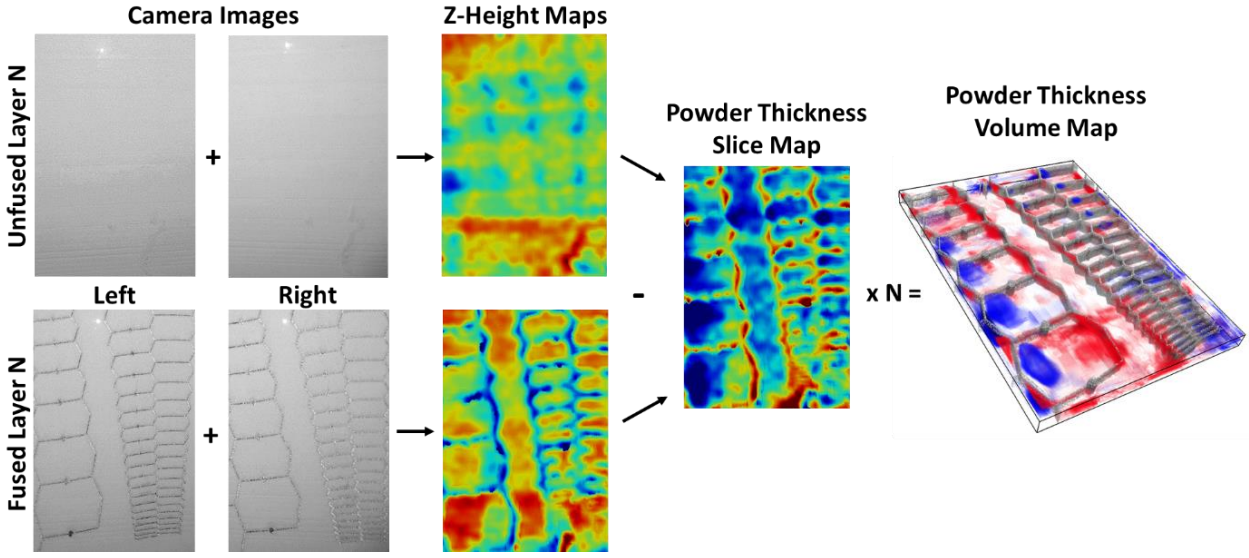

Figure 4.1: Data processing path from images to volumes used to produce quasi-tomographic representation of process variation in metal SLM.

Materials & Methods

Experimental Setup

This study utilized a stereo vision system (Figure 4.2) to monitor build surface variation in a ProX 320 (3D Systems) production SLM machine. The system employed two Grasshopper3 12MP USB 3.0 cameras with 4240 pixel x 2824 pixel resolution (3.1 µm pixel size) on a 1” format monochromatic CCD sensor (Point Grey). While mounted outside of the vacuum chamber to avoid extreme environmental conditions, the cameras examined the build platform through custom viewing windows designed to interface with pre-existing access ports. From this position, the optical working distance was measured to be 600 mm. Although precise values were determined from the extrinsic calibration

parameters, the distance between cameras was roughly 687 mm and the cameras were approximately 27º from vertical.

Figure 4.2: Conceptual experimental setup (left) actual implementation with custom viewing windows designed to interface with the production SLM machine (right).

The cameras were equipped with 35 mm lenses (Kowa) to accommodate the entire 203 mm x 135 mm build platform at a spatial resolution of 48 µm/pixel. However, this project only utilized the 102 mm x 76 mm sub-region of the build platform pictured in Figure 4.3. The extrusion-type geometry illustrated in the fused surface images was built from stainless steel 316L powder with a particle size distribution of 45 ± 15 µm, and a nominal layer thickness of 60 µm. Inside the chamber, two LED light panels (Polaroid 350) were employed to improve the contrast of metal powder surfaces for imaging. A cross-polarization scheme was implemented between the light panels and lenses to suppress specular reflections.

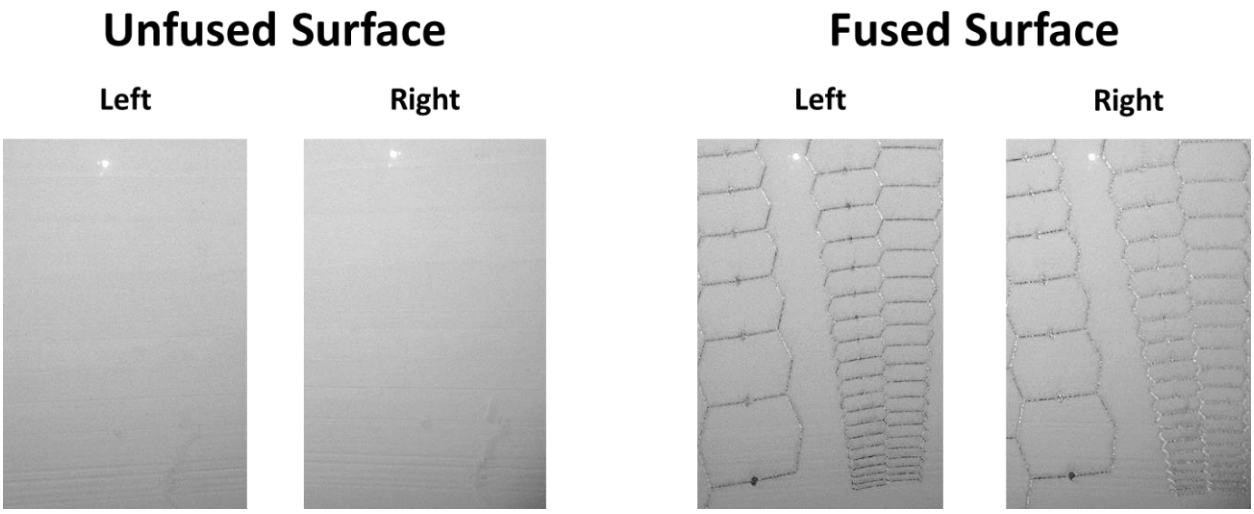

Figure 4.3: Example high-resolution images of metal powder surfaces within the sub-region of the build platform analyzed in this work (102 mm x 76 mm).

Stereoscopic 3D Surface Measurement using 3D Digital Image Correlation

3D Digital Image Correlation (DIC) is an established optical measurement technique most commonly employed in experimental mechanics applications to measure high-precision deformation and strain fields in specimens under loading [12]. The technique employs template matching algorithms to measure pointwise disparity values then uses stereo calibration information to reconstruct 3D surfaces. Consequently, one of the prerequisites for viable application of DIC is a locally unique surface pattern that supports the use of template matching for disparity measurement. In standard applications, a white light speckle pattern is applied to the surface of objects to attain sufficient distinguishability for reliable tracking from image-to-image (Figure 4.4). In this application, the optical similarity of metal powder to white light speckle provides a natural tracking mechanism that can be leveraged to measure disparity between stereoscopic images of the powder bed. The 316L stainless steel powder particles are sub-optimal compared to

ideal speckle for DIC (13), but the 48 µm/pixel camera resolution produced serviceable image texture for stereo correlation.

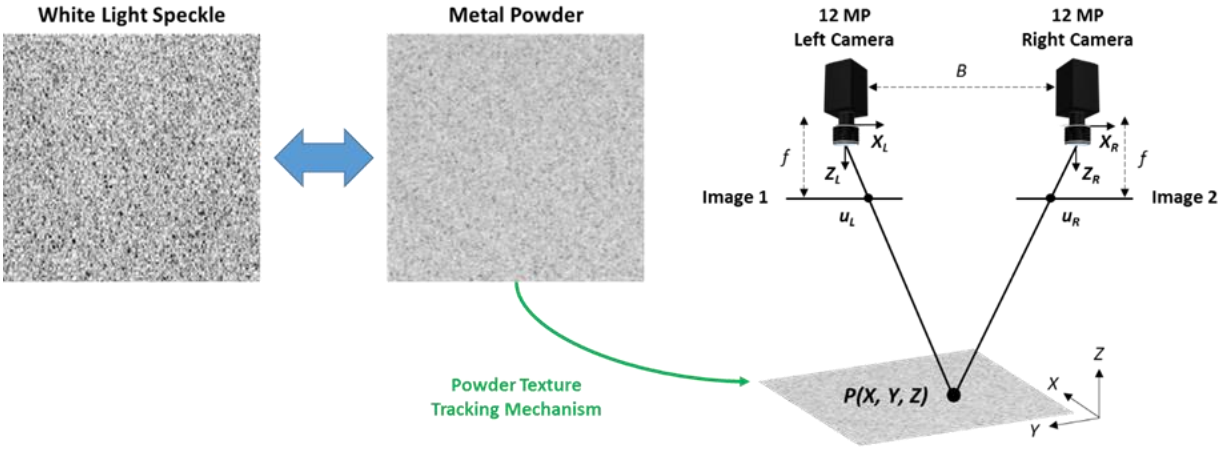

Figure 4.4: The optical similarity of illuminated metal powder to white light speckle is leveraged to extract 3D surface measurements from stereoscopic images of the powder bed using 3D DIC.

The commercial DIC measurement software Vic-3D (Correlated Solutions) was used for stereoscopic surface reconstruction. As mentioned before, stereo calibration is required to reconstruct 3D surfaces using DIC. Stereo camera parameters are estimated algorithmically by analyzing a sequence of calibration images. The images depict a planar calibration target containing a known regular grid pattern, positioned at different locations within the shared field of view (FoV) of the two-camera system. The system used in this work was calibrated with a standard Vic-3D dot grid target, containing 17 x 14 dots with 6 mm spacing. During calibration, 40 images were taken with the target at various positions, orientations, and tilts. Considerations were made to introduce extreme tilts, which improve out-of-plane calibration accuracy by providing maximum triangulation angles for solving the correspondence problem between 3D world coordinates and 2D image points [12].

The accuracy of surface reconstruction using DIC will ultimately depend on a variety of factors, including stereo calibration, camera resolution, FoV, lens distortion, system alignment, and surface pattern contrast [12]. Depending on setup, it is possible to achieve a wide-range of measurement accuracies using DIC. Systems with small stereo angles have been shown to achieve in-plane measurement accuracies of 1/340,000*FoV and out-of-plane accuracies of 1/19,000*FoV [14]. In general, a wide stereo angle can be used to optimize out-of-plane performance at the cost of in-plane measurement resolution [15]. The system employed in this study was decidedly wide-angle to benefit from maximum out-of-plane performance. It should also be noted that since only one-fourth of the camera FoV was utilized for this work, improved performance could have been attained by applying the entire sensor to monitor the area of interest.

In this study, 3D surfaces were reconstructed from stereo images taken both after the spread operation (unfused) and after the fusion operation (fused) for 100 layers. For each stereo pair, the Vic-3D analysis was performed with respect to the left-camera “reference image” at control points spaced every 5 pixels (240 µm) using 55-pixel subsets. The output of the Vic-3D analysis is 3D point cloud information of the form $[X, Y, Z]$ in world metric coordinates. However, since the measurements were made according to a regularly spaced pixel grid (control points), the planar sampling location in world coordinates will vary from layer-to-layer depending on relative surface height. To address this discrepancy, the z-height data associated with each surface was resampled onto a consistent spatial grid using cubic spline interpolation at a spacing of 240 µm (code found in Appendix B). Registering the data in this way creates sets of 4D data of the form:

$$Z(X,Y)_{N,unfused}$$

and

$$Z(X,Y)_{N,fused}$$

where N is the build layer number. Plotting this layer-wise surface variation data as a contour map produces the “z-height maps” shown in Figure 4.5. Z-height maps represent layer-by-layer build surface measurements needed to understand process variation, layer uniformity, and by extension the formation of defects and their location in metal AM [5-6, 9]. However, for the data to be properly utilized for the purposes of evaluating deviations in typical process behavior, stereoscopic surface measurements need to be shown in the context the entire build volume. The volume data will provide a tool for highlighting performance trends and exposing anomalous behavior regions that are indicative of defect formation in AM [11]. There is a fortuitous similarity between layer-wise z-height maps and slices of image data produced during XCT that can be leveraged to create these contextualized data sets. By treating z-height maps as analogous to slices of XCT data, we can produce a volumetric representation of in-situ measurement data with little additional effort. The first step in this effort is to convert individual z-height maps into equivalent grayscale images.

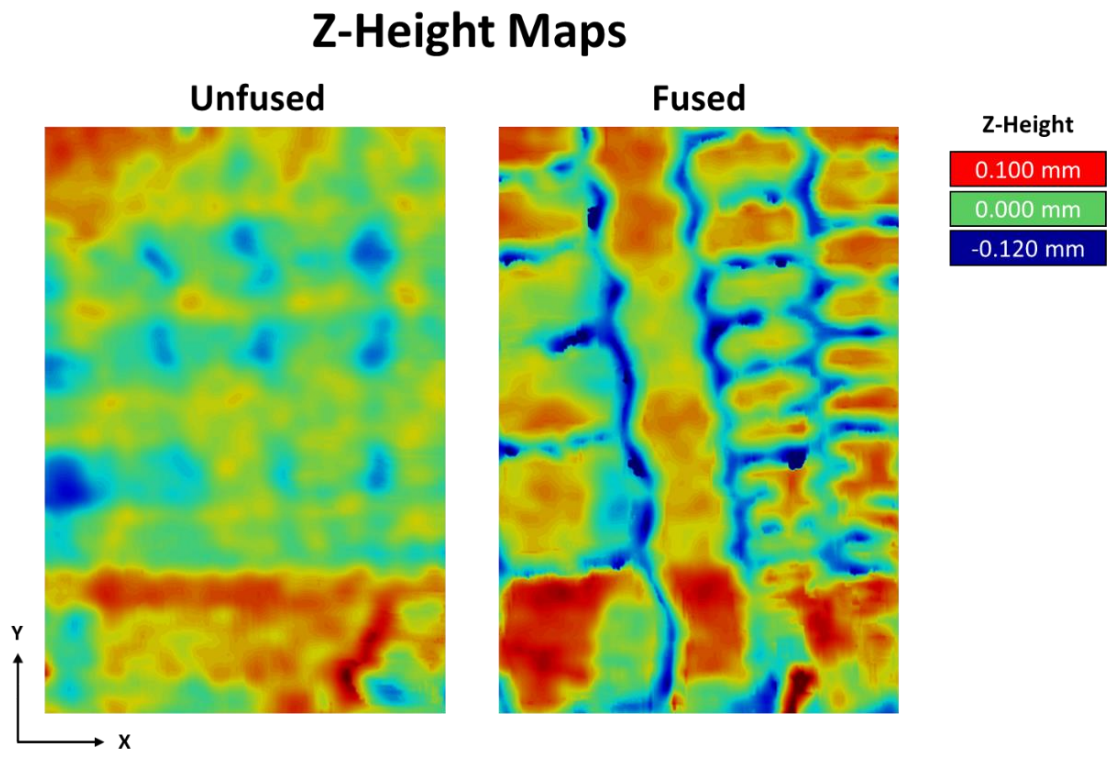

Figure 4.5: Example z-height maps showing SLM surface height over the 102 mm x 76 mm analysis region; unfused maps describe variation in post-spread surfaces and fused maps describe variation in post-fusion surfaces.

Converting Z-Height Maps to Grayscale Images

The primary difference between z-height maps and XCT image slices is their voxel content. Z-height maps contain floating point values, whereas XCT image slices are comprised of integer grayscale intensities. Converting z-height maps into grayscale images would be advantageous because they are convenient, require less memory, and enable the use of established and optimized tools for volume rendering. However, it is important for future evaluation that the conversion is performed in a way that preserves the quantitative nature of the measurement data. We also want to assure that all layer-wise z-height maps are converted consistently, such that grayscale values indicate the

same measurement value in each image. We can accomplish both by linearly mapping z-height values to grayscale intensities according to the following:

$$[Z_{min}\ Z_{max}] \rightarrow [0\ 255]$$

where Z_{min} and Z_{max} are chosen to include all measurement data. For this project, Z_{min} was selected to be -0.200 mm (black) and Z_{max} was set to 0.200 mm (white). Therefore, each grayscale intensity value represents roughly 1.6 µm of elevation change between black and white. Figure 4.6 shows converted "grayscale maps" plotted on a regular integer pixel grid (R, C), where the size of grayscale maps $G(R, C)$ remains equal to the size of z-height maps $Z(X, Y)$.

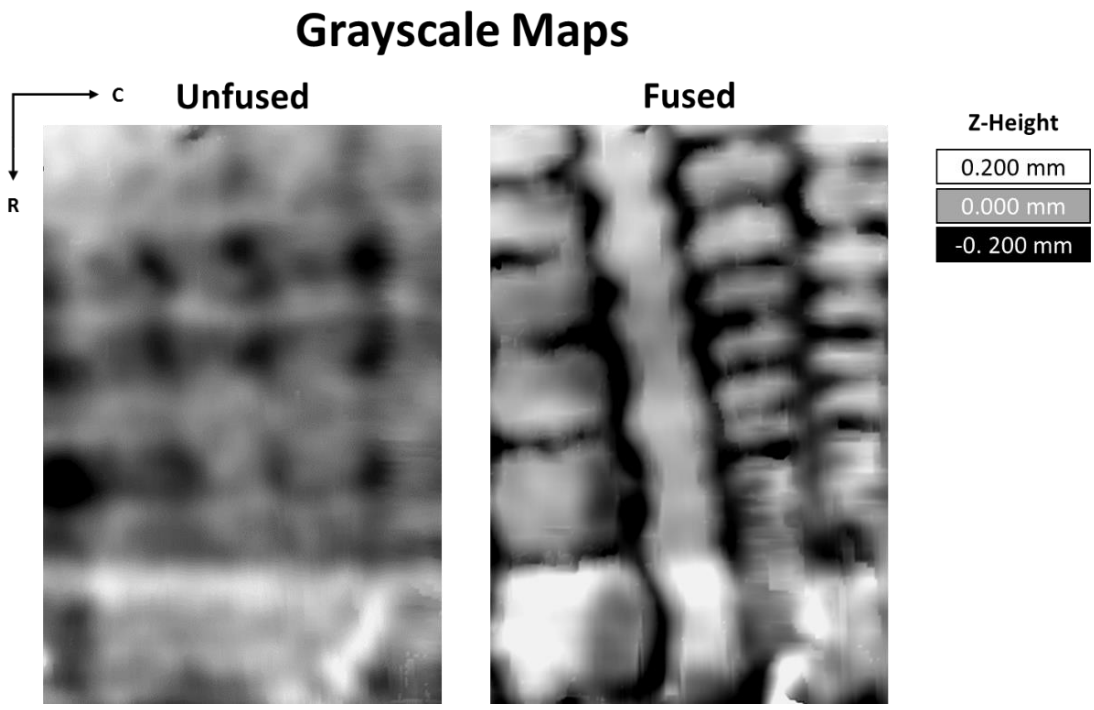

Figure 4.6: Example grayscale images representing in-situ surface measurement data in SLM. The size of grayscale maps is equal to the size of z-height maps.

Volumetric Rendering of Stereoscopic Build Surface Data

The procedure described in the previous section was used to convert 100 layers of unfused and fused surface z-height data into grayscale images. The resulting image stacks were imported into the open-source volume exploration and presentation tool Drishti (ANU Vizlab), where grayscale image volumes were generated and rendered for both unfused and fused surface data (Figure 4.7). Non-cubic voxels of 240 µm x 240 µm x 60 µm were used to accurately represent the spatial relationship between planar measurements and layer thickness.

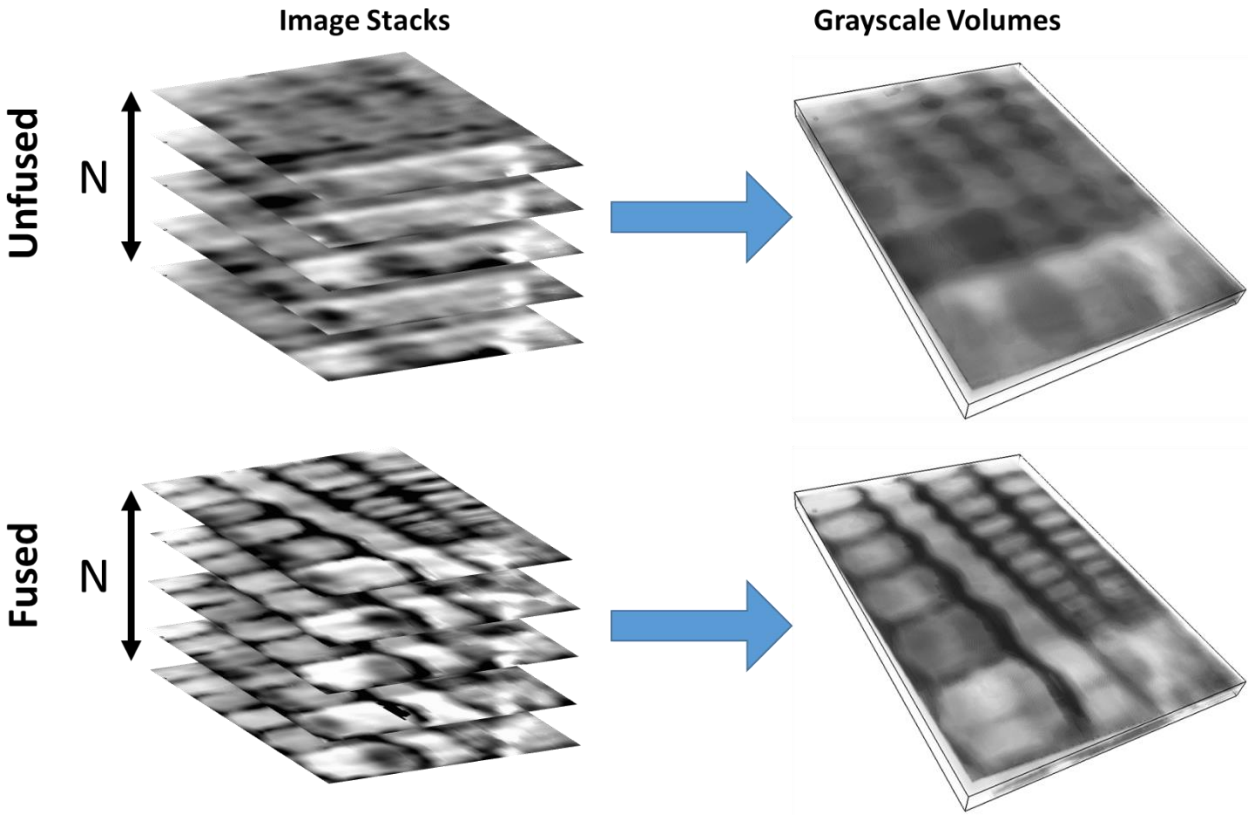

Figure 4.7: Image stacks representing measured surface variation are used to generate volumetric representations of stereoscopic data. The grayscale image volumes on the right comprise in-situ measurement data for 100 unfused and fused surfaces.

The first thing we notice about these initial renderings is that visualizing measured surface variation throughout the volume is nearly impossible. There is simply too much

poorly distinguished data to be useful. What we really want is a representation of the extreme occurrences of measured surface height. These regions are more likely to correspond to build surface issues [10, 16] associated with defect formation or at least behavior of interest. With this in mind, thresholding techniques were used to remove data that fell within the range of ±30 µm (one nominal layer thickness). The remaining data corresponding to extreme regions of measured surface height were then color-coded to improve distinguishability such that low values are displayed in blue and high values are displayed in red. These new "enhanced z-height volumes" deliver the contextual visualizations we were seeking (Figure 4.8).

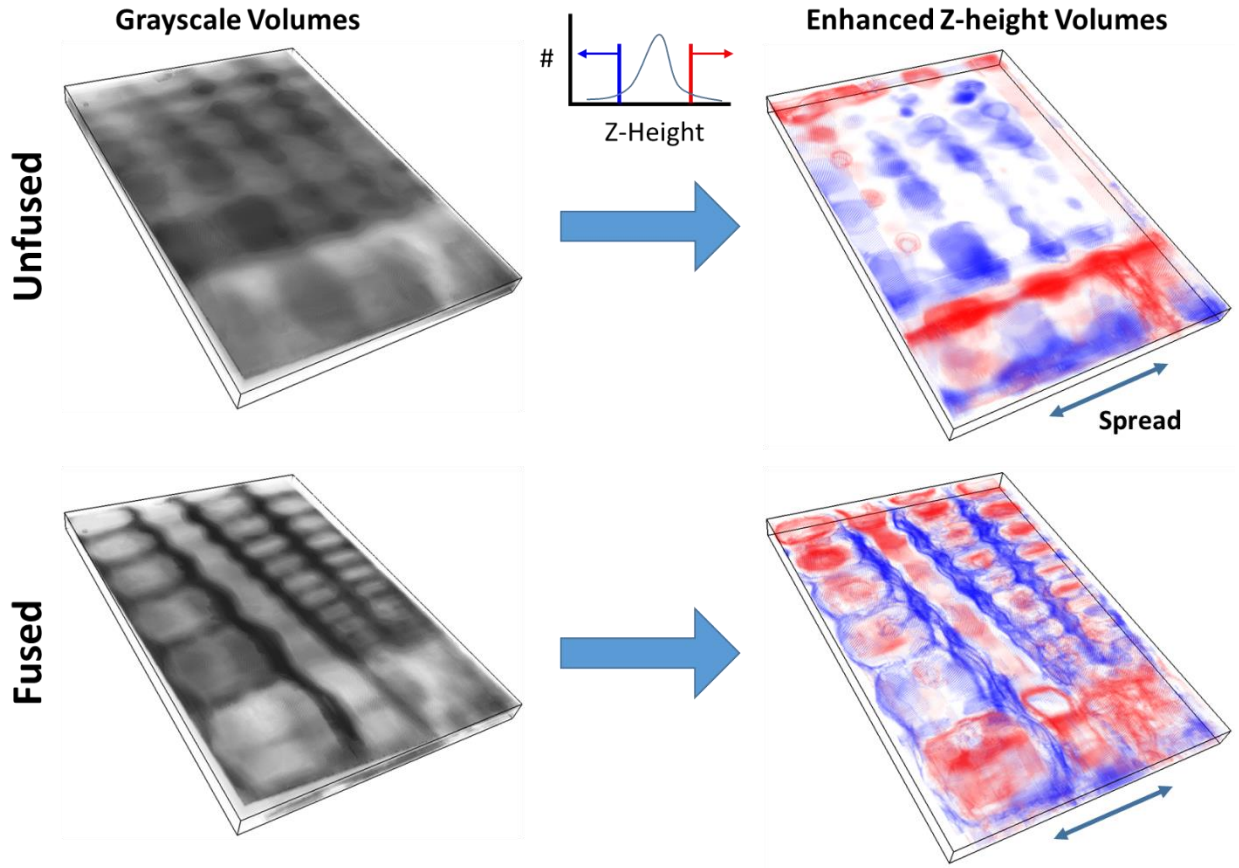

Figure 4.8: Z-height values falling within one nominal layer thickness are removed via thresholding. The remaining extreme regions are then color-coded to distinguish between high and low surface heights.

Both the unfused and fused surface volumes expose several noteworthy trends in a single glance. Parallel to spread direction, there is evidence of an elevated ridge that persists through the volume. In the unfused volume, we see low surface regions tending to systematically accumulate into four groupings perpendicular to the spread direction. These groupings also seem to coincide with locations of deeply depressed surfaces in the fused surface volume. Although these observations are interesting, it is difficult to draw conclusions regarding root cause or impact on part performance without seeing how surface variation manifests itself with respect to the constructed part geometry. We are therefore motivated to further contextualize these data sets with a visualization of as-built geometry.

Visualizing As-Built Geometry

The previous section ended with snapshot representations of unfused and fused surface variation over the course of 100 layers during the SLM test build. The volumetric views are useful independently for trend identification, but there is still ambiguity regarding how these variations relate to part geometry. Ideally, we would also have a way to reference part location within the build volume so that process behavior could be evaluated in the context of nominal build geometry, and vice versa. Fortunately, a byproduct of the stereoscopic measurement process is a set of grayscale images that depict a planar representation of each as-built cross-section. Casting the layer images into the same volumetric form as the surface variation images will yield a nominal depiction of the as-build part geometry that corresponds to the stereoscopic surface data being evaluated. However, for the geometry to be useful, we first need to register the raw camera images with the layer variation images generated earlier.

Due to conventions in DIC, it is standard for Vic-3D to output the pixel-wise control points (x, y) and their associated world metric coordinates $[X, Y]$ with respect to the left-camera images. Therefore, these images were used for the visualization. With the aforementioned information, the registration process was accomplished in three straightforward steps (code in Appendix D): (1) the images were scaled to the size of z-height maps by creating a mask that extracted grayscale intensity values at the control points (x, y), (2) the intensity values were mapped from control points to their respective world coordinate positions $[X, Y]$, and (3) the intensity values were resampled from $[X, Y]$ onto the same consistent spatial grid as the z-height data (240 µm spacing) using cubic spline interpolation. The registered images were then rendered in Drishti, where intensity thresholding was used to remove unfused powder regions, producing the reference geometry shown in Figure 4.9.

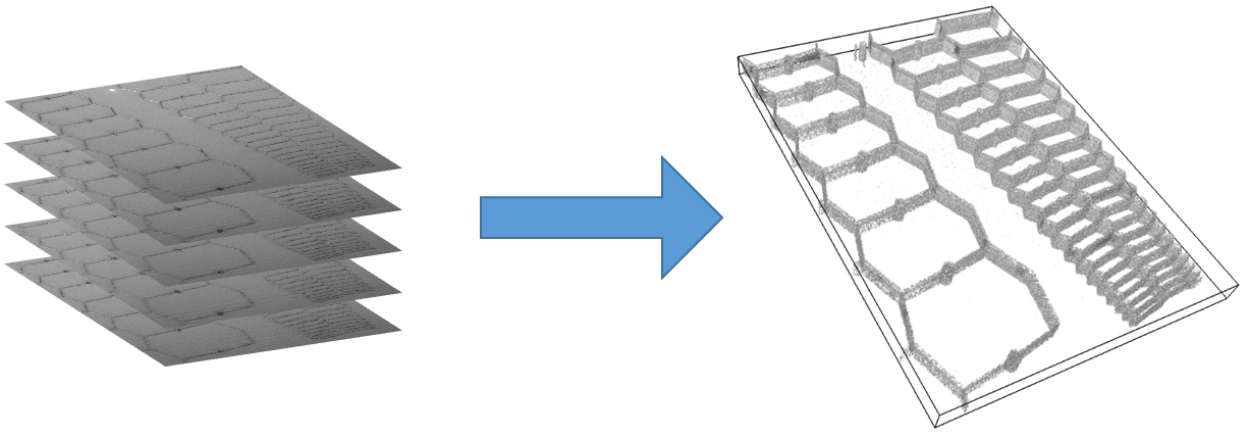

Figure 4.9: Left camera images were registered with grayscale metric images, then rendered in Drishti to produce a nominal representation of the as-built part geometry; unfused powder regions were removed via intensity thresholding.

Z-height volumes were superimposed onto the depiction of nominal part geometry (Figure 4.10) to create contextualized quasi-tomographic representations of SLM process variation measured using the in-situ stereo vision system. The addition of as-built

geometry allows us to identify where process deviations interact with the printed part. Pockets of extremely low z-height in the unfused surface volume accumulate near geometries that are perpendicular to the spread direction, indicating a potential systematic interaction between part and spreader. In the fused volume, low surface regions expectedly correspond with as-built part geometry. However, it is now also clear that an extreme source of process variation for the example build originates from the finer geometry constructed in the bottom right-corner of the build volume.

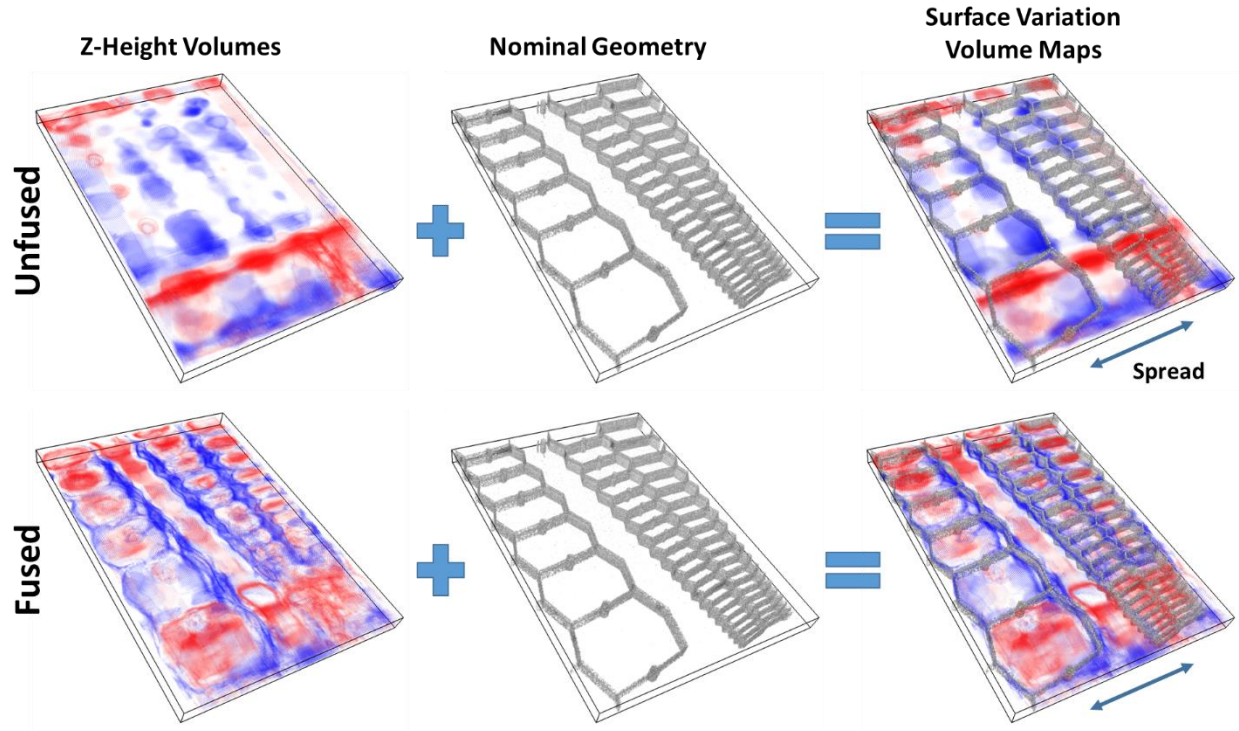

Figure 4.10: Superimposing z-height volumes on depiction of nominal build geometry creates contextualized quasi-tomographic representations of SLM process variation.

Results

Example Defect Detection using Volumetric Build Surface Stereo-CT Data

Although there are several instances of extreme process variation in the volume maps presented in Figure 4.10 that would ultimately need to be evaluated for part qualification, one particularly interesting area is the elevated ridge that appears and persists throughout the course of the build volume. In this region, we can see what appears to be characteristic part lifting associated with the formation of residual stresses in AM parts. This theory is corroborated by the presence of elevated surface areas in raw images of the unfused powder bed (Figure 4.11). Not only does this behavior indicate the probable formation of residual stresses [11] that contribute to mechanical deficiencies in final part properties, there is also a likelihood that the issue has a prevailing effect on layer uniformity and the manifestation of associated defects [5, 9-10] within the afflicted regions. For stereo-CT to provide sufficient understanding of AM part performance, volumetric layer uniformity trends will also need to be evaluated.

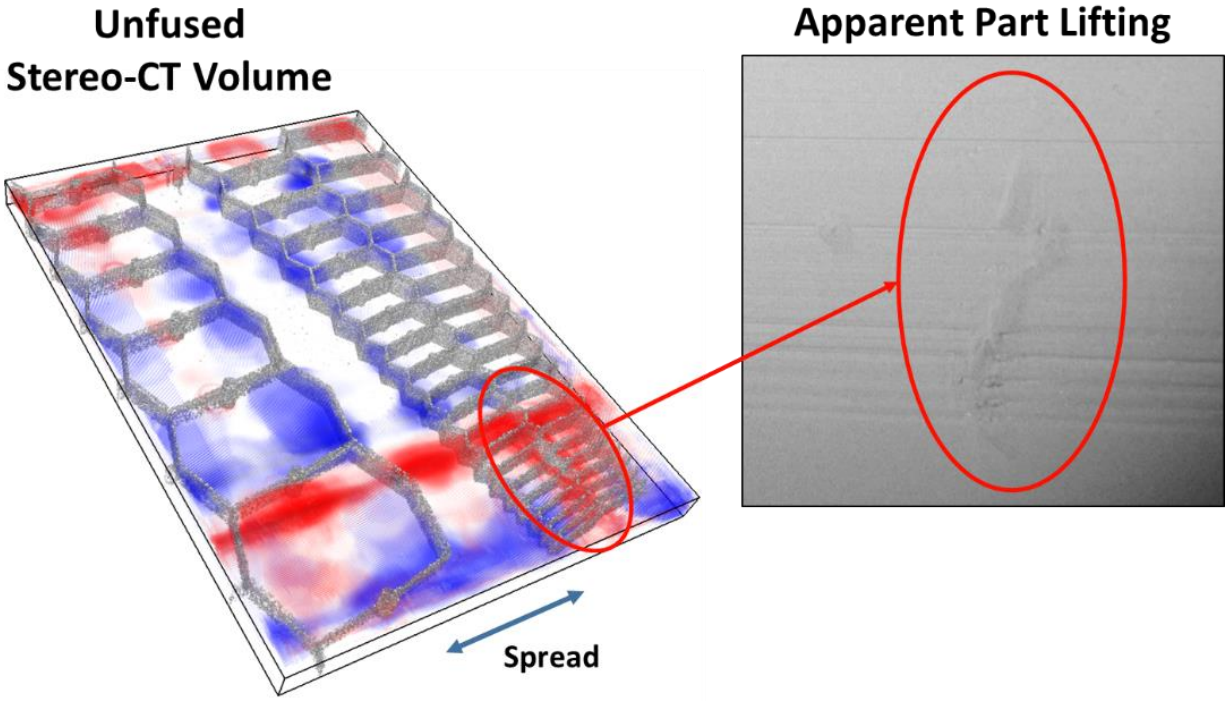

Figure 4.11: Unfused stereo-CT volume and raw image of apparent part lifting believed to be the source of persistent anomalous process behavior.

Volumetric Powder Layer Uniformity Evaluation using Stereo-CT Data

In addition to evaluating build surface variation independently at each stage of the process, the interactions between successive surfaces that describe layer uniformity need to be characterized. In this section, we investigate how measured surface variations (z-height maps) influence powder layer thickness. Deviations in powder layer thickness are closely linked to the formation of most typical defects in metal AM [5-6, 9]. Therefore, measuring and documenting the location of extreme occurrences of powder layer thickness throughout the build volume will enable local evaluation of mechanical properties with the appropriate deterministic models.

The thickness of applied powder at layer N can be calculated using z-height data acquired before and after the powder spreading operation. Mathematically, the definition for extracting powder layer thickness from z-height data is written as follows:

$$T(X,Y)_N = Z(X,Y)_{N,\,unfused} - Z(X,Y)_{N-1,fused} + \Delta Z_{platform}$$

where $T(X,Y)_N$ is the thickness of applied powder at layer N, $Z(X,Y)_{N,\,unfused}$ is the measured variation in the post-spread powder surface at layer N, $Z(X,Y)_{N-1,fused}$ is the z-height variation in the fused powder surface at layer $N-1$, and $\Delta Z_{platform}$ is the distance the platform drops before spreading occurs. The assumption for this study was that the build platform consistently dropped by the nominal 60 µm layer thickness.

Figure 4.12 shows a powder layer thickness volume map resulting from the data processing path shown in Figure 4.1. Powder thickness slice maps were calculated from z-height maps according to the equation above then converted to a volume map using the methods described in this manuscript. Thresholding techniques were used to remove thickness data that fell within the range of 60 ± 30 µm, then the remaining data was color-coded to enhance distinguishability. The accentuated map shows where extreme regions of powder layer thickness occur within the build volume as a result of the SLM layer construction operations. It also provides context for where these variations occur with respect to printed part geometry. Based on where layer uniformity deviations coincide with part geometry, there is likely to be a correlation between thick or thin powder regions and the occurrence of porosity [5, 9], surface roughness [10], residual stresses [7, 11], and ultimately final part properties [3, 5, 9]. By empirically determining thresholds for acceptable layer deviation as a function of resulting mechanical performance, it is

possible that stereo-CT can be used as a tool for rapidly identifying defective parts in metal powder bed AM processes.

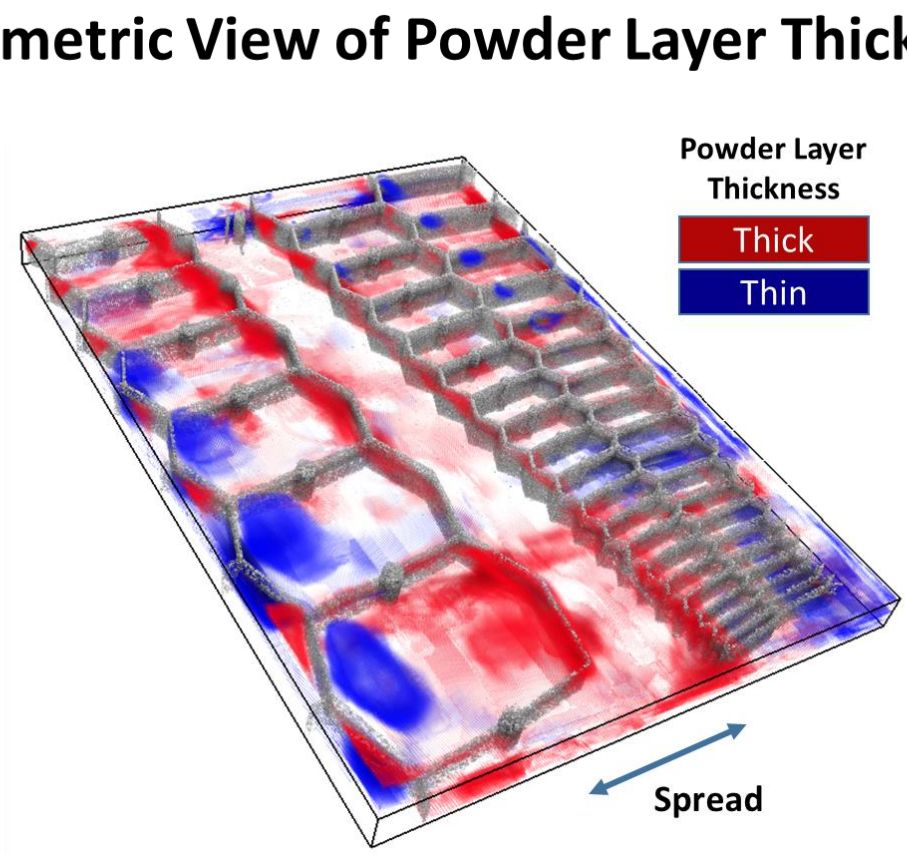

Figure 4.12: Powder layer thickness volume map produced by the stereo-CT method for metal SLM build.

Conclusions

This manuscript presented a methodology for producing quasi-tomographic representations of process variation in metal SLM using in-situ stereoscopic build surface data. Stereo-CT data was shown to be useful for identifying anomalous surface behavior likely associated with residual stress formation; corresponding damage afflicted on the silicone spreader bar by the lifted part was also distinguishable as an elevated surface

ridge that impacted both unfused and fused powder surfaces. Powder layer thickness volume maps were then created to show how individual surface variation accumulates to cause deviations in layer uniformity. Based on the process variations exposed by the stereo-CT data presented in this manuscript, it is likely that final part quality will depend on where it was printed within the build volume. Although the stereo-CT method is capable of providing the requisite volumetric build variance information needed to feed empirically-driven deterministic models for defect formation in metal PBF, the relationships between process variability and part quality are not yet fully formed. Future work should therefore be focused on developing suitable defect models and establishing databases of results that consistently link measurement observations with build outcomes. If reliable, quantifiable connections can be established between measured process variation and final part performance, then stereo-CT has the potential to be a valuable tool for streamlined part qualification in metal AM.

References

1. Tapia G, Elwany A (2014) A Review on Process Monitoring and Control in Metal-Based Additive Manufacturing. J. Manuf. Sci. Eng 136(6), 060801
2. King WE, Anderson AT, Ferencz RM, Hodge NE, Kamath C, Rubenchik AM (2015) Laser Power Bed Fusion Additive Manufacturing of Metals; Physics, Computational, and Materials Challenges. Applied Physics Review 2(4)
3. Spears TG and Gold SA (2016) In-process sensing in selective laser melting (SLM) additive manufacturing. Integrating Materials and Manufacturing Innovation (2016) 5(2)
4. Frazier WE (2014) Metal Additive Manufacturing: A Review. Journal of Materials Engineering and Performance 23(6)
5. Zhang M, Sun CN, Zhang X, Goh PC, Wei J, Li H, Hardacre D (2017) Competing Influence of Porosity and Microstructure on the Fatigue Property of Laser Powder

Bed Fusion Stainless Steel 316L. Proceedings of the 28th Annual International Solid Freeform Fabrication Symposium

6. Mower TM, Long MJ (2016) Mechanical Behavior of Additive Manufactured, Powder-Bed Laser-Fused Materials. Mat. Sci. and Eng. 651(2016):198-213

7. Van Belle L, Vansteenkiste G, and Boyer JC (2013) Investigation of Residual Stresses Induced During the Selective Laser Melting Process. Key Eng. Mater. 554-557(2013):1828-1834

8. Seifi M, Salem A, Beuth J, Harrysson O, Lewandowski JJ (2016) Overview of Materials Qualification Needs for Metal Additive Manufacturing. JOM 68(3):747:764

9. Sufiiarov VS, Popovich AA, Borisov EV, Polozov IA, Masaylo DV, Orlov AV (2017) The Effect of Layer Thickness at Selective Laser Melting. Procedia Engineering 174(2017):126-134

10. Craeghs T, Clijsters S, Yasa E, Bechmann F, Berumen S, Kruth JP (2011) Determination of geometrical factors in Layerwise Laser Melting using optical process monitoring. Optics and Lasers in Engineering 49(2011):1440-1446

11. Vlasea ML, Lane B, Lopez F, Mekhonstev S, Donmez A (2015) Development of Powder Bed Fusion Additive Manufacturing Test Bed for Enhanced Real-Time Process Control. Proceedings of the 26th Annual International Solid Freeform Fabrication Symposium

12. Sutton MA, Orteu JJ, and Schreier H (2009) Image Correlation for Shape, Motion and Deformation Measurements. Springer, NY, USA. doi: 10.1007/978-0-387-78747-3

13. Reu PL (2014) All about speckles: Speckle Size Measurement. Experimental Techniques 38(6):1-2

14. Wang YQ, Sutton MA, Ke XD, and Schreier H (2011) Error Assessment in Stereo-Based Deformation Measurements, Part II: Experimental Validation of Uncertainty and Bias Estimates. Exp. Mechanics 51(4):423-441

15. Wang YQ, Sutton MA, Ke XD, and Schreier H (2011) Error Assessment in Stereo-Based Deformation Measurements, Part I: Theoretical Developments for Quantitative Estimates. Exp. Mechanics 51(4):405-422

16. Craeghs T, Clijsters S, Yasa E, Kruth JP (2011) Online Quality Control of Selective Laser Melting. Proceedings of the 22nd Annual International Solid Freeform Fabrication Symposium

Chapter 5

General Conclusions:
A Foundation for Stereo Vision Metrology in Metal Additive Manufacturing

Daniel P. Mosher[1,2]

[1]Oregon State University, Corvallis, Oregon

[2]Department of Mechanical, Industrial, and Manufacturing Engineering

mosherd@oregonstate.edu

Conclusions

The manuscripts in this dissertation focused on the development of an in-situ stereovision-based metrology solution to address the gaps identified in Chapter 1 in state of the art metrology systems for metal Additive Manufacturing (AM). Many noteworthy contributions were made with regard to monitoring, characterizing, and presenting process variation in metal Powder Bed Fusion (PBF) AM technologies.

Chapter 2 described the implementation of a high-resolution stereo vision system to make accuracy-verified 3D build surface measurements in a production Selective Laser Melting (SLM) machine. The naturally occurring texture in metal powders and fused surfaces was demonstrated as a viable tracking mechanism for 3D surface reconstruction using Digital Image Correlation (DIC) [1]. At a spatial resolution of 48 µm/pixel, powder surface texture was used to achieve an out-of-plane measurement accuracy of ±6.0 µm. With this level of accuracy, stereo measurement data was shown to capture broad powder surface height variations, spreader bar wiper blade wear, interactions between powder spreading and part geometry, and powder irregularities linked to a focal build defect.

Chapter 3 extended in-situ stereoscopic build surface measurements into layer-wise measures of powder layer thickness, material densification, and incremental build height. These so-called Build Variance Metrics (BVMs) exposed significant process zone variability that undoubtedly contributes to the consistency issues associated with metal PBF. Tools for evaluating BVM uncertainty and specifying appropriate system components as a function of desired performance and constraints were presented along with suggestions for improving stereoscopic measurement performance. The spatial limitations of the stereo measurement technique were also described. Observations

included spread-direction and geometry-dependent variation in powder layer thickness, inconsistent material densification, and discrepancies between measured and assumed build height based on nominal layer thickness values. Based on these observations, a method was suggested for locally optimizing critical process parameters as a function of powder layer thickness maps with closed-loop feedback control from subsequent material densification measurements. The incremental build height metric was shown to provide information that enables high-level process control through adjustment of nominal layer thickness values to compensate for observed deviations from expected progress.

Chapter 4 presented a methodology for volumetrically rendering stereoscopic measurement data to produce quasi-tomographic representations of process variation for both unfused and fused surfaces in metal SLM. In a similar fashion, in-situ build surface data was used to produce a result that shows how powder layer thickness varies throughout the build volume. The volumetric stereo data was also superimposed onto a nominal depiction of the as-built geometry to provide context between build variations and the local properties of printed parts. This so-called stereo computed tomography (stereo-CT) approach was shown to be useful for identifying part lifting associated with residual stress formation [2-3] and layer uniformity deviations known to directly impact porosity [4-5], surface roughness [6], and the mechanical performance of PBF parts [4, 7-8]. If reliable, quantifiable connections can be established between measured process variation and final part performance, then stereo-CT has the potential to be a valuable tool for streamlined part qualification in metal AM.

Suggested Future Work

While the accomplishments above have provided a foundation of knowledge and novel learnings related to the application of stereo vision metrology to monitor, characterize, and present variability in metal powder bed AM processes, some priority areas of research remain before the potential of the technique can be fully realized. This section briefly describes these future work opportunities.

Feature-Informed Stereo Search Parameter Optimization for PBF Applications

The first area of research that will greatly benefit this technology is the development of optimized DIC algorithms for measuring 3D powder bed surface variation. Although metal powder and fused metal regions have been effectively used as a tracking mechanism for surface reconstruction using DIC, traditional methods for the selection of stereo search parameters are not ideal for the present application. In standard applications, where trackable surface texture is sufficiently homogenous, the use of a constant square subset size and consistent measurement spacing is adequate (Figure 5.1). However, for the case of powder bed surfaces, the quality of locally available texture will vary significantly depending on whether the surface is comprised of unfused powder, fused material, or a boundary between the two. As a result, the requirements for optimizing measurement accuracy and reliability will also change as a function of planar measurement location. The best results are achieved when these local requirements are met algorithmically. Strategies for locally adjusting subset size have been demonstrated for addressing variable density speckle patterns [9], but shape, orientation, and spacing adjustments remain largely unstudied due to a lack of need in common DIC applications. Therefore, investigation into methods for feature-informed adjustment of subset size,

shape, orientation, and spacing are a worthwhile endeavor for the application of stereo vision metrology to monitor powder beds. A critical advantage to consider for this effort is that CAD files offer knowledge of bed layout which can be used to effectively predetermine large portions of the stereo search strategy. This will alleviate some of the real-time computational requirements for localized parameter optimization.

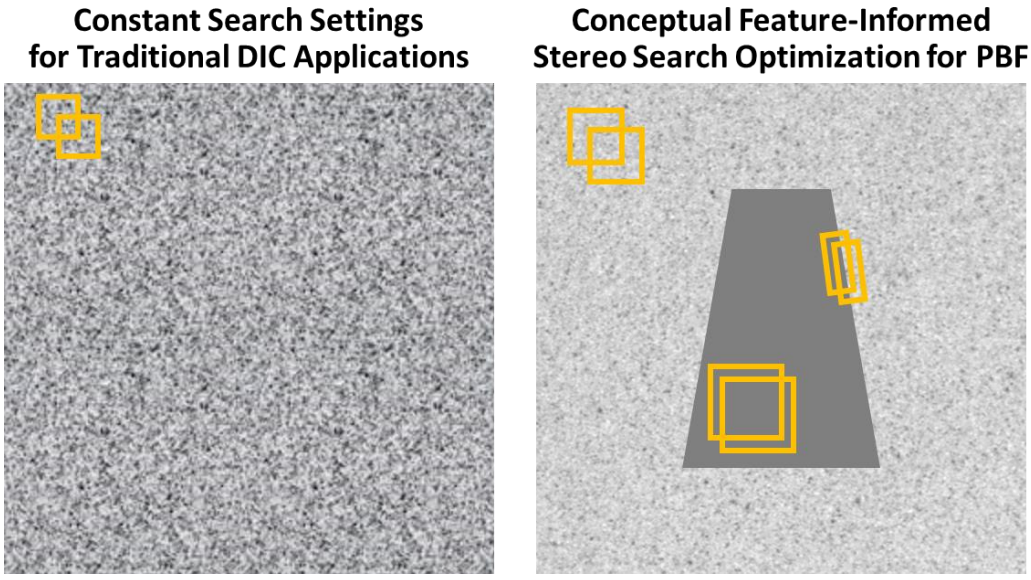

Figure 5.1: Constant square subset size and consistent spacing is sufficient for stereo correlation when using applied speckle patterns in traditional DIC, but powder bed surfaces require a more sophisticated approach to search parameter selection to optimize measurement performance.

Closed-Loop PBF Process Control System using BVMs

Another important area of research involves developing a closed-loop control system based on the BVMs presented in Chapter 3 to reduce the inherent process variability in metal PBF. In theory, layer-wise measures of powder layer thickness and material densification enable local optimization of laser power, scan speed, and scan pattern to reduce porosity [4-5], surface roughness [6], and the formation of residual stresses [2-3] in PBF parts. However, developing a successful closed-loop control strategy will likely be

a non-trivial task. Once a system is implemented, the process of drawing correlations between BVMs, parameter adjustments, and build outcomes can begin. At that point, the challenges associated with practical deployment of this solution will need to be reassessed which may also lead to further research opportunities.

Deterministic Models for Stereo-CT Defect Detection in PBF Parts

The stereo-CT method described in chapter 4 needs to be coupled with deterministic models for relating measured process variation to the formation of defects and the quality of final parts. While there are known correlations between build surface height, layer uniformity deviations, and the formation of typical defects [2-8] that contribute to mechanical performance issues in PBF parts, these connections are not well enough understood to be reliably applied for part qualification in an industry setting. Driving these documented relationships toward quantifiable, empirically-driven thresholds for acceptable process variation is a logical next step in this effort. End-to-end metrology experiments, where stereo-CT process monitoring is combined with typical AM post-production inspection, are recommended to validate defect causation and provide confidence in deterministic models. The development of a database infrastructure for housing, organizing, and comparing volumetric stereo-CT data should also be considered. Ultimately, due to the theoretically unlimited possibilities for AM part construction, a statistically-based, machine learning approach to part qualification would likely be an ideal solution to pursue for the stereo-CT method. A database of prior build outcomes organized according to build material, geometry, input parameters, and documented stereo-CT trends could be an extremely powerful tool for advancing current system knowledge and streamlining part qualification in metal AM.

References

1. Sutton MA, Orteu JJ, and Schreier H (2009) Image Correlation for Shape, Motion and Deformation Measurements. Springer, NY, USA. doi: 10.1007/978-0-387-78747-3

2. Vlasea ML, Lane B, Lopez F, Mekhonstev S, Donmez A (2015) Development of Powder Bed Fusion Additive Manufacturing Test Bed for Enhanced Real-Time Process Control. Proceedings of the 26th Annual International Solid Freeform Fabrication Symposium

3. Van Belle L, Vansteenkiste G, and Boyer JC (2013) Investigation of Residual Stresses Induced During the Selective Laser Melting Process. Key Eng. Mater. 554-557(2013):1828-1834

4. Zhang M, Sun CN, Zhang X, Goh PC, Wei J, Li H, Hardacre D (2017) Competing Influence of Porosity and Microstructure on the Fatigue Property of Laser Powder Bed Fusion Stainless Steel 316L. Proceedings of the 28th Annual International Solid Freeform Fabrication Symposium

5. Sufiiarov VS, Popovich AA, Borisov EV, Polozov IA, Masaylo DV, Orlov AV (2017) The Effect of Layer Thickness at Selective Laser Melting. Procedia Engineering 174(2017):126-134

6. Craeghs T, Clijsters S, Yasa E, Bechmann F, Berumen S, Kruth JP (2011) Determination of geometrical factors in Layerwise Laser Melting using optical process monitoring. Optics and Lasers in Engineering 49(2011):1440-1446

7. Spears TG and Gold SA (2016) In-process sensing in selective laser melting (SLM) additive manufacturing. Integrating Materials and Manufacturing Innovation (2016) 5(2)

8. Seifi M, Salem A, Beuth J, Harrysson O, Lewandowski JJ (2016) Overview of Materials Qualification Needs for Metal Additive Manufacturing. JOM 68(3):747:764

9. Pan B, Xie H, Wang Z, Qian K, Wang Z (2008) Study on Subset Size Selection in Digital image Correlation for Speckle Patterns. Optics Express 16(10):7037-7048

BIBLIOGRAPHY

Chapter [Reference]

1 [1] Tapia G, Elwany A (2014) A Review on Process Monitoring and Control in Metal-Based Additive Manufacturing. J. Manuf. Sci. Eng 136(6), 060801

1 [2] King WE, Anderson AT, Ferencz RM, Hodge NE, Kamath C, Rubenchik AM (2015) Laser Power Bed Fusion Additive Manufacturing of Metals; Physics, Computational, and Materials Challenges. Applied Physics Review 2(4)

1 [3] Spears TG and Gold SA (2016) In-process sensing in selective laser melting (SLM) additive manufacturing. Integrating Materials and Manufacturing Innovation (2016) 5(2)

1 [4] Fraizer WE (2014) Metal Additive Manufacturing: A Review. Journal of Materials Engineering and Performance 23(6):1917-28

1 [5] Everton SK, Hirsch M, Stravroulakis P, Leach RK, Clare AT (2016) Review of in-situ process monitoring and in-situ metrology for metal additive manufacturing. J. Materials & Design 95(2016)

1 [6] Craeghs T, Clijsters S, Yasa E, Kruth JP (2011) Online Quality Control of Selective Laser melting. Proceedings of the 22nd Annual International Solid Freeform Fabrication Symposium

1 [7] Dunsky C (2014) Process Monitoring in Laser Additive Manufacturing. Industrial Laser Solutions

1 [8] Wegner A, Witt G (2011) Process Monitoring in Laser Sintering using Thermal Imaging. Solid Freeform Fabrication: Proceedings, August 2011: University of Texas at Austin 2011

1 [9] Townsend A, Senin N, Blunt L, Leach RK, Taylor JS (2016) Surface Texture Metrology for Additive Manufacturing: A Review. Prec. Eng. 46(2016):34-47

1 [10] Bi G, Gasser A, Wissenbach K, Drenker A, Poprawe R (2006) Characterization of the Process Control for the Direct Laser Metallic Powder Deposition. Surface and Coatings Technology 201(6):2676-2683

1 [11] Bi G, Shürmann B, Gasser A, Wissenbach K, Poprawe R (2007) Development and Qualification of a Novel Laser-Cladding Head with Integrated Sensors. International Journal of machine Tools and manufacturing 47(3):555-561

1 [12] Lott P, Schleifenbaum H, Meiners W, Wissenbach K, Hinke C, Bultmann J (2011) Design of an Optical system for the In Situ Process Monitoring of Selective Laser Melting (SLM). Physics Procedia 12(2011):683-690

BIBLIOGRAPHY (Continued)

Chapter [Reference]

1 [13] Craeghs T, Bechmann F, Berumen S, Kruth JP (2010) Feedback control of Layerwise Laser Melting using Optical Sensors. Physics Procedia 5(2010):505-514

1 [14] Craeghs T, Clijsters S, Yasa E, Bechmann F, Berumen S, Kruth JP (2011) Determination of geometrical factors in Layerwise Laser Melting using optical process monitoring. Optics and Lasers in Engineering 49(2011):1440-1446

1 [15] Doubenskaia M, Pavlov M, Grigoriev S, Tikhonova E, Smurov I (2012) Comprehensive Optical Monitoring of Selective Laser Melting. Journal of Laser Micro/Nanoengineering 7(3):236-243

1 [16] Krauss H, Eschey C, Zaeh MF (2012) Thermography for Monitoring the Selective Laser Melting Process. Proceedings of the Solid Freeform Fabrication Symposium

1 [17] Seifi M, Salem A, Beuth J, Harrysson O, Lewandowski JJ (2016) Overview of Materials Qualification Needs for Metal Additive Manufacturing. JOM 68(3):747:764

1 [18] Cooke AL, Moylan SP (2011) Process Intermittent Measurement for Powder-Based Additive Manufacturing. Proceedings of the 22nd International SFF Symposium – An Additive Manufacturing Conference

1 [19] Kleszczynski S, Jacobsmühlen J zur, Sehrt JT, Witt G (2012) Error Detection in Laser Beam Melting Systems by High Resolution Imaging. Proceedings of the 23rd Annual International Solid Freeform Fabrication Symposium

2 [1] Tapia G, Elwany A (2014) A Review on Process Monitoring and Control in Metal-Based Additive Manufacturing. J. Manuf. Sci. Eng 136(6), 060801

2 [2] King WE, Anderson AT, Ferencz RM, Hodge NE, Kamath C, Rubenchik AM (2015) Laser Power Bed Fusion Additive Manufacturing of Metals; Physics, Computational, and Materials Challenges. Applied Physics Review 2(4)

2 [3] Spears TG and Gold SA (2016) In-process sensing in selective laser melting (SLM) additive manufacturing. Integrating Materials and Manufacturing Innovation (2016) 5(2)

2 [4] Purtonen T, Kalliosaari A, Salminen A (2014) Monitoring and Adaptive Control of Laser Processes. Physics Procedia 56(2014):1218-1231

BIBLIOGRAPHY (Continued)

Chapter [Reference]

2 [5] Bi G, Gasser A, Wissenbach K, Drenker A, Poprawe R (2006) Characterization of the Process Control for the Direct Laser Metallic Powder Deposition. Surface and Coatings Technology 201(6):2676-2683

2 [6] Bi G, Shürmann B, Gasser A, Wissenbach K, Poprawe R (2007) Development and Qualification of a Novel Laser-Cladding Head with Integrated Sensors. International Journal of machine Tools and manufacturing 47(3):555-561

2 [7] Lott P, Schleifenbaum H, Meiners W, Wissenbach K, Hinke C, Bultmann J (2011) Design of an Optical system for the In Situ Process Monitoring of Selective Laser Melting (SLM). Physics Procedia 12(2011):683-690

2 [8] Craeghs T, Bechmann F, Berumen S, Kruth JP (2010) Feedback control of Layerwise Laser Melting using Optical Sensors. Physics Procedia 5(2010):505-514

2 [9] Craeghs T, Clijsters S, Yasa E, Bechmann F, Berumen S, Kruth JP (2011) Determination of geometrical factors in Layerwise Laser Melting using optical process monitoring. Optics and Lasers in Engineering 49(2011):1440-1446

2 [10] Doubenskaia M, Pavlov M, Grigoriev S, Tikhonova E, Smurov I (2012) Comprehensive Optical Monitoring of Selective Laser Melting. Journal of Laser Micro/Nanoengineering 7(3):236-243

2 [11] Krauss H, Eschey C, Zaeh MF (2012) Thermography for Monitoring the Selective Laser Melting Process. Proceedings of the Solid Freeform Fabrication Symposium

2 [12] Craeghs T, Clijsters S, Yasa E, Kruth JP (2011) Online Quality Control of Selective Laser melting. Proceedings of the 22nd Annual International Solid Freeform Fabrication Symprosium

2 [13] Dunsky C (2014) Process Monitoring in Laser Additive Manufacturing. Industrial Laser Solutions

2 [14] Wegner A, Witt G (2011) Process Monitoring in Laser Sintering using Thermal Imaging. Solid Freeform Fabrication: Proceedings, August 2011: University of Texas at Austin 2011

2 [15] Cooke AL, Moylan SP (2011) Process Intermittent Measurement for Powder-Based Additive Manufacturing. Proceedings of the 22nd International SFF Symposium – An Additive Manufacturing Conference

BIBLIOGRAPHY (Continued)

Chapter [Reference]

2 [16] Kleszczynski S, Jacobsmühlen J zur, Sehrt JT, Witt G (2012) Error Detection in Laser Beam Melting Systems by High Resolution Imaging. Proceedings of the 23rd Annual International Solid Freeform Fabrication Symposium

2 [17] Colla et al. (2014) Monitoring Concepts for a 3D Printer Applied to Build a Human Outpost on the Moon. 16th International Conference on Computer Modelling and Simulation

2 [18] Townsend A, Senin N, Blunt L, Leach RK, Taylor JS (2016) Surface Texture Metrology for Additive Manufacturing: A Review. Prec. Eng. 46(2016):34-47

2 [19] Holzmond H, Li X (2017) In Situ Real Time Defect Detection of 3D Printed Parts. Journal of Additive Manufacturing 17(2017):135-142

2 [20] Sutton MA, Orteu JJ, and Schreier H (2009) Image Correlation for Shape, Motion and Deformation Measurements. Springer, NY, USA. doi: 10.1007/978-0-387-78747-3

2 [21] Wang YQ, Sutton MA, Ke XD, and Schreier H (2011) Error Assessment in Stereo-Based Deformation Measurements, Part I: Theoretical Developments for Quantitative Estimates. Exp. Mechanics 51(4):405-422

2 [22] Wang YQ, Sutton MA, Ke XD, and Schreier H (2011) Error Assessment in Stereo-Based Deformation Measurements, Part II: Experimental Validation of Uncertainty and Bias Estimates. Exp. Mechanics 51(4):423-441

2 [23] Hartley R and Zisserman A (2003) Multiple View Geometry in computer vision. Cambridge University Press. ISBN 0-521-54051-8.

3 [1] Frazier WE (2014) Metal Additive Manufacturing: A Review. Journal of Materials Engineering and Performance 23(6)

3 [2] Tapia G, Elwany A (2014) A Review on Process Monitoring and Control in Metal-Based Additive Manufacturing. J. Manuf. Sci. Eng 136(6), 060801

3 [3] King WE, Anderson AT, Ferencz RM, Hodge NE, Kamath C, Rubenchik AM (2015) Laser Power Bed Fusion Additive Manufacturing of Metals; Physics, Computational, and Materials Challenges. Applied Physics Review 2(4)

3 [4] Spears TG and Gold SA (2016) In-process sensing in selective laser melting (SLM) additive manufacturing. Integrating Materials and Manufacturing Innovation (2016) 5(2)

BIBLIOGRAPHY (Continued)

Chapter [Reference]

3 [5] Craeghs T, Clijsters S, Yasa E, Kruth JP (2011) Online Quality Control of Selective Laser Melting. Proceedings of the 22nd Annual International Solid Freeform Fabrication Symposium

3 [6] Kleszczynski S, Jacobsmühlen J zur, Sehrt JT, Witt G (2012) Error Detection in Laser Beam Melting Systems by High Resolution Imaging. Proceedings of the 23rd Annual International Solid Freeform Fabrication Symposium

3 [7] Everton SK, Hirsch M, Stravroulakis P, Leach RK, Clare AT (2016) Review of in-situ process monitoring and in-situ metrology for metal additive manufacturing. J. Materials & Design 95(2016)

3 [8] O'Regan P, Prickett P, Setchi R, Hankins Gareth, Jones N (2016) Metal Based Additive Layer Manufacturing: Variations, Correlations, and Process Control. Procedia Computer Science 96(2016):216-224

3 [9] Land WS, Zhang B, Ziegert J, Davies A (2015) In-Situ Metrology System for Laser Powder Bed Fusion Additive Process. Procedia Manufacturing 1(2015)

3 [10] Holzmond H, Li X (2017) In Situ Real Time Defect Detection of 3D Printed Parts. Journal of Additive Manufacturing 17(2017):135-142

3 [11] Wheeler AJ, Ganji AR (2009) Introduction to Engineering Experimentation 3rd Edition. Englewood Cliffs, NJ, USA. ISBN 0131742760

3 [12] Sutton MA, Orteu JJ, and Schreier H (2009) Image Correlation for Shape, Motion and Deformation Measurements. Springer, NY, USA. doi: 10.1007/978-0-387-78747-3

3 [13] Hartley R and Zisserman A (2003) Multiple View Geometry in computer vision. Cambridge University Press. ISBN 0-521-54051-8

3 [14] Sufiiarov VS, Popovich AA, Borisov EV, Polozov IA, Masaylo DV, Orlov AV (2017) The Effect of Layer Thickness at Selective Laser Melting. Procedia Engineering 174(2017):126-134

3 [15] Zhang M, Sun CN, Zhang X, Goh PC, Wei J, Li H, Hardacre D (2017) Competing Influence of Porosity and Microstructure on the Fatigue Property of Laser Powder Bed Fusion Stainless Steel 316L. Proceedings of the 28th Annual International Solid Freeform Fabrication Symposium

BIBLIOGRAPHY (Continued)

Chapter [Reference]

3 [16] Craeghs T, Clijsters S, Yasa E, Bechmann F, Berumen S, Kruth JP (2011) Determination of geometrical factors in Layerwise Laser Melting using optical process monitoring. Optics and Lasers in Engineering 49(2011):1440-1446

3 [17] Jacob G, Donmez A, Slotwinski J, Moylan S (2016) Measurement of Powder Bed Density in Powder Bed Fusion Additive Manufacturing Processes. Measurement Science and Technology 27(2016)

3 [18] Vlasea ML, Lane B, Lopez F, Mekhonstev S, Donmez A (2015) Development of Powder Bed Fusion Additive Manufacturing Test Bed for Enhanced Real-Time Process Control. Proceedings of the 26th Annual International Solid Freeform Fabrication Symposium

3 [19] Wang YQ, Sutton MA, Ke XD, and Schreier H (2011) Error Assessment in Stereo-Based Deformation Measurements, Part I: Theoretical Developments for Quantitative Estimates. Exp. Mechanics 51(4):405-422

3 [20] Wang YQ, Sutton MA, Ke XD, and Schreier H (2011) Error Assessment in Stereo-Based Deformation Measurements, Part II: Experimental Validation of Uncertainty and Bias Estimates. Exp. Mechanics 51(4):423-441

3 [21] Cyganek B, Siebert JP (2009) An Introduction to 3D Computer Vision Techniques and Algorithms. John Wiley & Sons, NJ, USA. ISBN 047001704X

4 [1] Tapia G, Elwany A (2014) A Review on Process Monitoring and Control in Metal-Based Additive Manufacturing. J. Manuf. Sci. Eng 136(6), 060801

4 [2] King WE, Anderson AT, Ferencz RM, Hodge NE, Kamath C, Rubenchik AM (2015) Laser Power Bed Fusion Additive Manufacturing of Metals; Physics, Computational, and Materials Challenges. Applied Physics Review 2(4)

4 [3] Spears TG and Gold SA (2016) In-process sensing in selective laser melting (SLM) additive manufacturing. Integrating Materials and Manufacturing Innovation (2016) 5(2)

4 [4] Frazier WE (2014) Metal Additive Manufacturing: A Review. Journal of Materials Engineering and Performance 23(6)

4 [5] Zhang M, Sun CN, Zhang X, Goh PC, Wei J, Li H, Hardacre D (2017) Competing Influence of Porosity and Microstructure on the Fatigue Property of Laser Powder Bed Fusion Stainless Steel 316L. Proceedings of the 28th Annual International Solid Freeform Fabrication Symposium

BIBLIOGRAPHY (Continued)

Chapter [Reference]

4 [6] Mower TM, Long MJ (2016) Mechanical Behavior of Additive Manufactured, Powder-Bed Laser-Fused Materials. Mat. Sci. and Eng. 651(2016):198-213

4 [7] Van Belle L, Vansteenkiste G, and Boyer JC (2013) Investigation of Residual Stresses Induced During the Selective Laser Melting Process. Key Eng. Mater. 554-557(2013):1828-1834

4 [8] Seifi M, Salem A, Beuth J, Harrysson O, Lewandowski JJ (2016) Overview of Materials Qualification Needs for Metal Additive Manufacturing. JOM 68(3):747:764

4 [9] Sufiiarov VS, Popovich AA, Borisov EV, Polozov IA, Masaylo DV, Orlov AV (2017) The Effect of Layer Thickness at Selective Laser Melting. Procedia Engineering 174(2017):126-134

4 [10] Craeghs T, Clijsters S, Yasa E, Bechmann F, Berumen S, Kruth JP (2011) Determination of geometrical factors in Layerwise Laser Melting using optical process monitoring. Optics and Lasers in Engineering 49(2011):1440-1446

4 [11] Vlasea ML, Lane B, Lopez F, Mekhonstev S, Donmez A (2015) Development of Powder Bed Fusion Additive Manufacturing Test Bed for Enhanced Real-Time Process Control. Proceedings of the 26th Annual International Solid Freeform Fabrication Symposium

4 [12] Sutton MA, Orteu JJ, and Schreier H (2009) Image Correlation for Shape, Motion and Deformation Measurements. Springer, NY, USA. doi: 10.1007/978-0-387-78747-3

4 [13] Reu PL (2014) All about speckles: Speckle Size Measurement. Experimental Techniques 38(6):1-2

4 [14] Wang YQ, Sutton MA, Ke XD, and Schreier H (2011) Error Assessment in Stereo-Based Deformation Measurements, Part II: Experimental Validation of Uncertainty and Bias Estimates. Exp. Mechanics 51(4):423-441

4 [15] Wang YQ, Sutton MA, Ke XD, and Schreier H (2011) Error Assessment in Stereo-Based Deformation Measurements, Part I: Theoretical Developments for Quantitative Estimates. Exp. Mechanics 51(4):405-422

4 [16] Craeghs T, Clijsters S, Yasa E, Kruth JP (2011) Online Quality Control of Selective Laser Melting. Proceedings of the 22nd Annual International Solid Freeform Fabrication Symposium

BIBLIOGRAPHY (Continued)

Chapter [Reference]

5 [1] Sutton MA, Orteu JJ, and Schreier H (2009) Image Correlation for Shape, Motion and Deformation Measurements. Springer, NY, USA. doi: 10.1007/978-0-387-78747-3

5 [2] Vlasea ML, Lane B, Lopez F, Mekhonstev S, Donmez A (2015) Development of Powder Bed Fusion Additive Manufacturing Test Bed for Enhanced Real-Time Process Control. Proceedings of the 26th Annual International Solid Freeform Fabrication Symposium

5 [3] Van Belle L, Vansteenkiste G, and Boyer JC (2013) Investigation of Residual Stresses Induced During the Selective Laser Melting Process. Key Eng. Mater. 554-557(2013):1828-1834

5 [4] Zhang M, Sun CN, Zhang X, Goh PC, Wei J, Li H, Hardacre D (2017) Competing Influence of Porosity and Microstructure on the Fatigue Property of Laser Powder Bed Fusion Stainless Steel 316L. Proceedings of the 28th Annual International Solid Freeform Fabrication Symposium

5 [5] Sufiiarov VS, Popovich AA, Borisov EV, Polozov IA, Masaylo DV, Orlov AV (2017) The Effect of Layer Thickness at Selective Laser Melting. Procedia Engineering 174(2017):126-134

5 [6] Craeghs T, Clijsters S, Yasa E, Bechmann F, Berumen S, Kruth JP (2011) Determination of geometrical factors in Layerwise Laser Melting using optical process monitoring. Optics and Lasers in Engineering 49(2011):1440-1446

5 [7] Spears TG and Gold SA (2016) In-process sensing in selective laser melting (SLM) additive manufacturing. Integrating Materials and Manufacturing Innovation (2016) 5(2)

5 [8] Seifi M, Salem A, Beuth J, Harrysson O, Lewandowski JJ (2016) Overview of Materials Qualification Needs for Metal Additive Manufacturing. JOM 68(3):747:764

5 [9] Pan B, Xie H, Wang Z, Qian K, Wang Z (2008) Study on Subset Size Selection in Digital image Correlation for Speckle Patterns. Optics Express 16(10):7037-7048

APPENDIX A: MATLAB Code – Plotting Platform Drop Data

```
clear all
close all

%% Theory
D = 0.063;    %pixel
e = 0.073;   %pixel
B = 687e3;   %microns
f = 51521;   %pixel from vic-3d
Z = 600e3;   %microns
ZerrorMean = 2*(D + e)*Z^2/(B*f)
deltaZ = [0 30 60];
Zerror = zeros(1,length(deltaZ));
for i = 1:length(deltaZ)
Zerror(i) = 2*(D + e)*(Z+deltaZ(i))^2/(B*f); %microns
end

%% Import and plot experimental data
filename = 'Platform Drop Experiment Data.xlsx';
xlRange = 'A2:A8893';
Datum = -1000*xlsread(filename,'Datum',xlRange);
Drop30 = -1000*xlsread(filename,'Drop 30',xlRange);
Drop60 = -1000*xlsread(filename,'Drop 60',xlRange);
Data = [Datum, Drop30, Drop60];
Labels = {'0 microns','30 microns','60 microns'};
maxTheory = deltaZ+Zerror;
minTheory = deltaZ-Zerror;
figure
h1 = plot(deltaZ,maxTheory,'r-','LineWidth',1.05)
hold on
h2 = plot(deltaZ,minTheory,'b-','LineWidth',1.05)
h3 = plot(deltaZ,deltaZ,'g--')
legend([h1 h2],{'Upper Theoretical Bound (+2Z_e)','Lower
Theoretical Bound (-2Z_e)'},'location','northwest')
boxplot(Data,'Labels',Labels,'positions',deltaZ,'Widths',2,'Symb
ol','y+')
title('Stereo Vision Measured Z-Height Results (Z_e = 1.4
microns)')
xlabel('Platform Drop \DeltaZ \pm 0.2%')
ylabel('Measured \DeltaZ (microns)')
xlim([-5 70])
ylim([-5 70])
hold off
grid on
```

APPENDIX B: MATLAB Code – Plotting Z-Height Maps

```
close all
clear all

spacing = 0.240;

%% Import floating point z-height data
dpost = csvread('089-postspread_0.csv');
x = dpost(:,1);
y = dpost(:,2);
z = dpost(:,3);
[X,Y] = meshgrid(min(x):spacing:max(x),min(y):spacing:max(y));
Zpost = griddata(x,y,z,X,Y,'cubic');

dpre = csvread('089-prespread_0.csv');
x = dpre(:,1);
y = dpre(:,2);
z = dpre(:,3);
Zpre = griddata(x,y,z,X,Y,'cubic');

figure(1)
subplot(1,2,1)
surf(Zpre)
subplot(1,2,2)
surf(Zpost)
shading interp
grid off
colormap(jet)
set(gca,'Ydir','Normal')
pbaspect([76/102 1 1])
title('Z-Height Maps')
az = 0;
el = 90;
view(az, el);
```

APPENDIX C: MATLAB Code – Spatial Convolution Simulation

```
close all
clear all

max = 2125;
A = 0.045;
x = [0:max];
z = A*rand(1,length(x)); % Simulated unfused powder surface
z = z - mean(z);

%% Adding step functions to simulate fused regions
for i = 252:302
z(i) = 0.00*rand(1) - 0.1;
end

for i = 802:827
z(i) = 0.00*rand(1) - 0.1;
end

for i = 1352:1362
z(i) = 0.00*rand(1) - 0.1;
end

for i = 1852:1857
z(i) = 0.00*rand(1) - 0.1;
end

%% Creating representative 1D gaussian window and spacing
subSize = 55;
spacing = 5;
subHW = floor(subSize/2);
subset = [-subHW:subHW];
gauss = normpdf(subset);

%% Convolving to create reconstructed surface
for i = subHW+1:spacing:length(x)-subHW-1
    xz(i) = i;
  Zs(i) = dot(z(i-subHW:i+subHW),gauss);
end

count = 1;
for i = 1:length(Zs)
    if abs(Zs(i))>0
        Zstep(count) = Zs(i);
```

```
        count = count + 1;
    end
end

spaceVec = [0:spacing:max];

%% Plotting simulated and reconstructed surfaces
figure(1)
plot(x,z)
title('Simulated 1-D Surface Height')
xlim([0 max])
ylim([-0.12 0.05])
grid on
hold off

xvec = [subHW:spacing:max-subHW];

figure(2)
Zstep = spline(xvec,Zstep,xvec);
plot(xvec,Zstep)
title('Reconstructed 1-D Surface Height')
xlim([0 max])
ylim([-0.12 0.05])
grid on
```

APPENDIX D: MATLAB Code – Geometry Image Registration

```
clear all
close all

path = 'C:\Stainless Steel Build\';
fileType = '.csv'; % original data file type
imageType = '.tif'; % grayscale image type

dirData = dir(strcat(path,'*.csv'));
fileNames = {dirData.name};
fileName = string(fileNames(1));
csvData = csvread(strcat(path,fileNames(1))); % read in .csv
files

x = csvData(:,1); % X data
y = csvData(:,2); % Y data
z = csvData(:,3); % Z data

spacing = 0.240;
[X,Y] = meshgrid(min(x):spacing:max(x),min(y):spacing:max(y));

for i = 1:length(fileNames)
    fileName = fileNames(i); % .csv file name
    csvData = csvread(strcat(path,string(fileName))); % read in
.csv file

    x = csvData(:,1); % X data(world coordinates X)
    y = csvData(:,2); % Y data (world coordinates Y)
    z = csvData(:,3); % Z data (world coordinates Z)
    c = csvData(:,4); % x data (control points C)
    r = csvData(:,5); % y data (control points R)

    % read in grayscale geometry image
    buildImage =
imread(strcat(path,strrep(string(fileName),fileType,imgType)));

    scaledImage = buildImage(r,c); % scale to z-height map size

    registeredImage = griddata(x,y,scaledImage,X,Y,'cubic'); %
interpolate intensities to same regular pixel grid as z-height
    geometryImageName =
char(strcat(path,'geometry\','geometry',fileNumber,imageType)) %
grayscale image name
    imwrite(I,geometryImageName) % save image
end
```